Experimental and theoretical studies in quantum metrology with optomechanical and multi-parameter-estimation applications

Magdalena Szczykulska
Brasenose College, Oxford

Submitted for the degree of Doctor of Philosophy

Trinity Term, 2018

Supervised by Dr. Michael Vanner,
Dr. Animesh Datta and Prof. Ian A. Walmsley

Clarendon Laboratory,
University of Oxford,
United Kingdom

Experimental and theoretical studies in quantum metrology with optomechanical and multi-parameter-estimation applications

Magdalena Szczykulska
Brasenose College, Oxford

Submitted for the degree of Doctor of Philosophy
Trinity Term, 2018

Abstract

This thesis explores the field of optomechanics and the theory of multi-parameter estimation for quantum metrology applications.

An optomechanical state inside a microresonator-taper system is studied experimentally, where the optical and mechanical modes interact by means of Brillouin anti-Stokes scattering. The scattering leads to sideband cooling of the mechanical (acoustic) mode and the underlying optomechanical coupling takes the form of a beam-splitter interaction Hamiltonian. The mechanical mode is further cooled by continuously monitoring the optical anti-Stokes mode by a heterodyne detector. The resulting time-domain data is input offline to a stochastic master equation model for Gaussian states to optimally estimate the mechanical phase space trajectories and subsequently reduce the observer's uncertainty associated with the phase space coordinates. It is shown that more information about the mechanical mode can be obtained by heterodyne monitoring than by the commonly used in optomechanics homodyne detection for the beam-splitter type interaction Hamiltonians.

The second part of this thesis theoretically considers the problem of simultaneous estimation of phase and phase diffusion using fixed-particle number states in the framework of quantum Cramér-Rao bound. Quantum Fisher information matrices are derived analytically in the limits of large and small diffusive noise to quantify the maximum amount of information available in the individual estimation of the parameters. The former is for a general fixed-particle number state and the latter for Holland-Burnett states for which quantum-enhanced estimation of phase as well as diffusion can be obtained. The precision limits given by quantum Fisher information may not be achievable in the joint estimation of the parameters due to the possible non-commutativity of the optimal measurements and this can be quantified in terms of a trade-off relation. This trade-off relation can reach the maximum of 2 in the large diffusion regime, whereas in the small diffusion regime a numerical evidence is shown that the optimal trade-off relation approaches 1 for Holland-Burnett states. These numerical results are valid in the small particle number regime. Finally, numerical results showing behaviour of the trade-off for a general value of phase diffusion when using Holland-Burnett states are provided.

To my Dad for all his support and encouragement to get me where I am now.

List of publications

1. M. Szczykulska, T. Baumgratz, and A. Datta. "Multi-parameter quantum metrology", Advanced in Physics: X 1, 621 (2016)

2. M. Szczykulska, T. Baumgratz, and A. Datta. " Reaching for the quantum limits in the simultaneous estimation of phase and phase diffusion ", Quantum Science and Technology 2, 044004 (2017)

3. G. Enzian, M. Szczykulska, J. Silver, L. Del Bino, S. Zhang, I. A. Walmsley, P. Del'Haye, and M. R. Vanner, "Observation of Brillouin optomechanical strong coupling with an 11 GHz mechanical mode", Optica 6, 7 (2019)

4. M. Szczykulska, G. Enzian, J. Zhang, J. Silver, L. Del Bino, S. Zhang, I. A. Walmsley, P. Del'Haye, K. Mølmer, and M. R. Vanner, " Heterodyne measurement enhanced cooling for optomechanics", manuscript in preparation

Acknowledgements

First of all I would like to thank Michael Vanner, Animesh Datta and Ian Walmsley for all their support and encouragement in completing my projects and beyond.

I would like to thank all my colleagues in the ultrafast quantum optics group at the University of Oxford with special thanks to Georg Enzian for all the many interesting discussions and for being a great support during my DPhil studies.

It has been a pleasure to work with Klaus Mølmer and Jinglei Zhang at the University of Aarhus, and I am very grateful to them for sharing their expertise and knowledge with me.

I would also like to thank Defence, Science and Technology Laboratory (DSTL) for providing the financial support during my DPhil years.

Last but not least, I would like thank my family and friends who have always been there for me in good and bad times. In particular, I would like to thank my Mum for her positivity, understanding and care.

Contents

Part I

Quantum metrology introduction

Chapter 1

From classical to quantum

1.1 A brief history of metrology

The story of metrology is the story of measurements. Its beginnings go as far as the beginnings of humankind. The ability to measure objects was crucial to hunt, build tools, shelters and eventually civilisations. Initially, people were using natural units found in the surroundings to compare their measurements such as length of body parts and weight of grain or seeds. However, these units were not always the same as different people as well as grain and seeds varied in size. Measurements could only be meaningful to everybody if people used the same standardised units of measure. Hence, there came the need to establish common standards that could be used by everybody to quantify the outcome of measurements. Adopting a common artefact as a unit of measure was a way of achieving this goal and the first recorded attempt of such a permanent standard was an Egyptian Cubit around 2,500 BC [1]. The Cubit was a wooden measuring rod derived from the length of the Egyptian Pharaoh's elbow down to the outstretched tip of his middle finger.

Development of standardised units went through many evolutions since, but its crucial moments took place more recently towards the end of the 18th century. The first such moment was the establishment of the decimal metric system in French law which happened in 1799 during the French Revolution. Here, the natural units of length and mass were replaced by the meter and the kilogram, and decimal multiples and fractions of these units. They were based on platinum prototypes with the overall aim of supporting the local trade. Another big step towards common standards took place in the late 18th to early 19th century during the Industrial Revolution. Mass production of goods during this time meant that accuracy of units of measure became increasingly important. In 1875, during a conference of an international commission to supervise the construction of the international metric system, a meter convention was signed by the participating nations. According to the convention, the participating countries would adopt the new international prototypes of the meter and kilogram followed by a 4-yearly General Conference on Weights and Measures (CGPM). The list of units was later extended to include other physical units, for instance the ampere. Finally, in 1960 during the 11th CGPM, the modern international system of units (SI units) was adopted. The ultimate goal in this direction since has been to redefine the SI units in terms of fundamental quantities. This would ensure the long term stability of the units which can not be guaranteed with the artefacts as the underlying basis of the definition. Moreover, fundamental quantities ought to carry less uncertainty resulting in more precise base units which is very important for precision metrology.

Improving measurement precision is another objective of metrology and it has had a very big impact on the world we live in today by enabling advances in areas such as navigation, telecommunication, transport and medicine [2]. Similarly to the standardized units, precision metrology started advancing during the Industrial Revolution when the mass production of items motivated the development of high level measuring machines. While initially the attainable precision was thought to be an engineering problem, the birth of quantum mechanics brought in the appreciation of fundamental limits in precision metrology arising due to quantum noise.

1.2 Thesis outline

This thesis is divided into three parts. Part I (chapters 1, 2 and 3) gives a pedagogical introduction to the quantum metrology concepts relevant for the works presented in parts II and III.

Part II (chapters 4, 5 and 6) describes an experimental study of a Brillouin optomechanical system, where the optical and mechanical modes are coupled by a beam-splitter interaction Hamiltonian leading to sideband cooling of the mechanical mode. Additionally, the optical mode is continuously monitored by means of balanced heterodyne detection. The collected time-domain data can then be input to an appropriate stochastic master equation model to allow an optimal state estimation of the system. The monitoring further enhances the already present sideband cooling of the mechanical motion by reducing the observer's uncertainty about where the mechanical state resides in phase space i.e. it reduces the variance associated with its phase space coordinates. One of the important messages here is that heterodyne detection beats homodyne detection in cooling of the mechanical mode for beam-splitter type optomechanical couplings.

Part III (chapters 7, 8, 9 and 10) is a theoretical consideration of the quantum estimation process in the quantum Cramér-Rao bound framework. Here, the main goal is to establish the quantum limits in the simultaneous estimation of phase and phase diffusion for fixed-particle number states.

The following is a list of chapters with a brief summary of their contents.

- Chapter 1 reviews the basics of quantum mechanics at the core of which is the probabilistic nature of a quantum measurement process arising due to quantum noise. It ends by introducing the three main stages of a quantum estimation process.

- Chapter 2 gives a quantum description of the probe states relevant for this thesis. It also briefs how a probe state interacts with the system of interest.

- Chapter 3 introduces the specific measurements relevant for parts II and III of this thesis. While part III considers a general positive operator-valued measure formalism, part II is based on balanced heterodyne detection.

- Chapter 4 introduces the field of optomechanics and explains the Physics of couplings between the mechanical and optical modes. It describes the radiation pressure coupling and the electrostrictive coupling. The latter is of crucial importance for the work presented in this thesis.

- Chapter 5 describes the physical features of the optomechanical platform which consists of a whispering gallery mode resonator evanescently coupled to a tapered fibre. The chapter discusses the underlying system Hamiltonian and the corresponding Langevin equations of motion that lead to the power spectral density of the heterodyned light. Further, it describes the parameter regime in which the system can operate. The system is capable of achieving strong coupling between the mechanical and optical modes [3], but it is important to note that this is not the desired parameter regime for cooling of the mechanical motion. The achieved system parameters for cooling of the mechanical mode are listed in table (5.1).

- Chapter 6 describes the continuous monitoring protocol applied to the time-domain data obtained by heterodyning the optical mode of the optomechanical state. The chapter presents the associated results showing the phase space trajectories of the mechanical mode and the amount of achieved cooling. It ends with an overall summary of part II.

- Chapter 7 gives an introduction to multi-parameter quantum metrology with the emphasis on the precision bounds in a parameter estimation process. It describes the quantum Cramér-Rao bound framework which is crucial for the work presented in part III. In particular, it introduces classical and quantum Fisher information quantities – distinguishability metrics, on the space of probability distributions and quantum states respectively, that quantify the amount of "information" about parameters. A review article on the topic of multi-parameter quantum metrology was published in [4].

- Chapter 8 motivates the importance of unitary and non-unitary parameter estimation. It introduces the main goal of part III which is to find the quantum limits in the simultaneous estimation of phase and phase diffusion parameters using fixed-particle number states. It emphasises the problem associated with simultaneous estimation of multiple parameters due to the non-commutativity of measurements in quantum mechanics. This work was published in [5].

- Chapter 9 gives the relevant background for the main work of part III. Although the quantum limits are attainable in the individual parameter estimation, this cannot be guaranteed when estimating the parameters simultaneously due to the possible non-commutativity of measurements. This leads to a trade-off in how much information can be gained about one parameter in the expense of the other parameter. Chapter 9 quantifies this trade-off relation for the considered multi-parameter estimation scheme via $\mathrm{Tr}\left[\mathbf{F}\mathbf{H}^{-1}\right]$, where

F and **H** are the classical and quantum Fisher information matrices respectively and Tr denotes the trace operation.

- Chapter 10 presents the results in three regimes of the diffusive noise: large, small and intermediate values of phase diffusion. The results report on the obtained quantum Fisher information and the trade-off relation quantity. While the large and small diffusion regime results are to a large extent analytical, the intermediate diffusion regime is studied numerically for the special case of Holland-Burnett states. The chapter ends with a summary of part III.

- Chapter 11 concludes all the parts of this thesis.

1.3 Classical measurement formalism

A classical system can be described by a set of system variables whose possible values define a configuration space and the state of such a system is represented by a probability distribution on that configuration space. Therefore, the system state describes observer's knowledge about the system variables. An ideal measurement on a classical system reveals with certainty the values of all the system variables. Therefore, the state of such a system can at least in principle be made deterministic i.e. all the system variables have assigned values with a probability of 1. In general, this is not the case with quantum systems where for any detection scheme the associated measurement outcomes have a corresponding probability distribution. As a consequence, a measurement can only reveal the system parameters with a probability less than unity.

1.4 Quantum measurement formalism

Throughout part I of this thesis, bold quantities will refer to vectors of numbers or more generally to matrices, whereas the circumflex diacritic will denote operators.

1.4.1 Quantum state

The state of a quantum system is represented by a vector in a complex vector space – Hilbert space – with an arbitrarily large dimension. Similarly to the classical case, the quantum state describes the observer's knowledge about the system. The basis states $|\phi_i\rangle$ of the Hilbert space are defined such that they are orthonormal and therefore their inner product is $\langle\phi_i|\phi_j\rangle = \delta_{ij}$. The state corresponding to the maximal knowledge is known as a pure state given by

$$|\psi\rangle = \sum_i \psi_i |\phi_i\rangle \tag{1.1}$$

and it is normalised such that the state's inner product with itself satisfies

$$\langle\psi|\psi\rangle = \sum_i |\psi_i|^2 = 1. \tag{1.2}$$

A matrix representation of the pure state defined in Eqn. (1.1) is $|\psi\rangle\langle\psi|$. More generally, a quantum state can be prepared as a classical mixture of pure states $|\psi_j\rangle\langle\psi_j|$ each with probability p_j. Such a state is called a mixed state and it is denoted by the density operator $\hat{\rho}$ which reads

$$\hat{\rho} = \sum_j p_j |\psi_j\rangle\langle\psi_j|. \tag{1.3}$$

The state is normalised so that $\mathrm{Tr}\left[\hat{\rho}\right] = 1$.

In order to access the physical properties of $\hat{\rho}$, we need to introduce objects called operators which can be defined as

$$\hat{A} = \sum_{ij} A_{ij} |\phi_i\rangle\langle\phi_j|, \tag{1.4}$$

where $A_{ij} \in \mathbb{C}$. One of the simplest connections that can be made with the state of the system is to find the expectation value of $\hat{A}$ with respect to $\hat{\rho}$ which is given by

$$\langle \hat{A} \rangle = \mathrm{Tr}\{\hat{A}\hat{\rho}\}. \tag{1.5}$$

An isolated quantum system undergoes a reversible evolution generated by a Hermitian operator also called the Hamiltonian or energy operator $\hat{H}$. In the Schrödinger picture, where the system changes but the operators are constant, the evolution is governed by

$$\frac{\mathrm{d}}{\mathrm{d}t}\hat{\rho}(t) = -\frac{\mathrm{i}}{\hbar}\left[\hat{H}, \hat{\rho}(t)\right]. \tag{1.6}$$

The unitary operator $\hat{U}$, satisfying $\hat{U}^\dagger \hat{U} = \hat{I}$ where $\hat{I}$ is the identity matrix, that can be applied to the state to give the evolution in Eqn. (1.6) is $\hat{U} = \mathrm{e}^{-\mathrm{i}\hat{H}t}$. For systems that are in contact with external baths and are being measured, the state evolution can be described by an appropriate stochastic master equation [6, 7]. Such a situation is considered in chapter 6 of this thesis.

1.4.2 Quantum measurements

Quantum measurements can be described by a collection of measurement operators $\{\hat{M}_m\}$ which act on the state space of the system being measured [8]. The subscript m denotes the possible measurement outcomes and the state of the quantum system immediately before the measurement is $\hat{\rho}$. The probability that the experimentalist obtains the m^{th} result is

$$p(m) = \mathrm{Tr}\left[\hat{M}_m^\dagger \hat{M}_m \hat{\rho}\right] \tag{1.7}$$

and the normalised state of the system after the measurement is

$$\hat{\rho}' = \frac{\hat{M}_m \hat{\rho} \hat{M}_m^\dagger}{\mathrm{Tr}\left[\hat{M}_m^\dagger \hat{M}_m \hat{\rho}\right]}. \tag{1.8}$$

The measurement operators satisfy the completeness relation given by

$$\sum_m \hat{M}_m^\dagger \hat{M}_m = \hat{I} \tag{1.9}$$

which is equivalent to the statement that the probabilities of the measurement outcomes add up to 1 i.e. $\sum_m p_m = \sum_m \mathrm{Tr}\left[\hat{M}_m^\dagger \hat{M}_m \hat{\rho}\right] = \mathrm{Tr}\left[\hat{\rho} \sum_m \hat{M}_m^\dagger \hat{M}_m\right] = \mathrm{Tr}\left[\hat{\rho}\right] = 1$.

The set of measurements $\{\hat{M}_m\}$ gives an observer access to the physical properties – called observables – of the studied system. In the quantum measurement formalism, the observables are denoted by Hermitian operators.

In the special case of projective measurements, the measurement can be described by a set of projectors $\{\hat{M}_m\} = \{\hat{P}_m\} = \{|m\rangle\langle m|\}$ which satisfies $\hat{P}_m \hat{P}_{m'} = \delta_{mm'} \hat{P}_m$. These measurement operators can be represented by an observable $\hat{M} = \sum_m m|m\rangle\langle m|$. The projectors $\{\hat{P}_m\}$ project the state of the system onto the eigenstates of $\hat{M}$ which gives an experimentalist full information about the observable.

More generally, $\hat{M}_m$ can be a weighted sum of projectors $\hat{M}_m = \sum_n q_{n,m}|n\rangle\langle n|$ with the underlying observable $\hat{N} = \sum_n n|n\rangle\langle n|$ that the observer tries to obtain information about. A measurement outcome m prepares the state of the system in a combination of the eigenstates of observable $\hat{N}$ and as a result, the measurement provides only partial information about $\hat{N}$. This more general quantum measurement treatment is encapsulated in the positive operator-valued measure (POVM) formalism. Here, a measurement is described by a set of operators $\{\hat{E}_m\}$, where $\hat{E}_m = \hat{M}_m^\dagger \hat{M}_m$, and the only condition that they have to satisfy is the completeness relation given by $\sum_m \hat{E}_m = \hat{I}$.

At the end of any quantum measurement process, the statistics of the measurement outcomes determines the properties of the studied quantum system.

1.4.3 Heisenberg uncertainty principle

Observables associated with position and momentum of a particle have continuous spectra and can be expressed as

$$\hat{X} = \int x|x\rangle\langle x|\mathrm{d}x \tag{1.10}$$

and

$$\hat{P} = \int p|p\rangle\langle p|\mathrm{d}p \tag{1.11}$$

respectively. The corresponding eigenstates of $\hat{X}$ and $\hat{P}$, $|x\rangle$ and $|p\rangle$, are normalised such that $\int |x\rangle\langle x|\mathrm{d}x = \hat{I}$ and $\int |p\rangle\langle p|\mathrm{d}p = \hat{I}$.

Operators $\hat{X}$ and $\hat{P}$ can also be expressed in terms of creation $\hat{c}^\dagger$ and annihilation $\hat{c}$ operators. These operators represent the mode of a field and satisfy the commutation relation given by

$$\left[\hat{c}, \hat{c}^\dagger\right] = \hat{c}\hat{c}^\dagger - \hat{c}^\dagger\hat{c} = 1. \tag{1.12}$$

With this, the position and momentum operators can be defined as

$$\hat{X} = x_{\mathrm{zpf}}\left(\hat{c}^{\dagger} + \hat{c}\right) \tag{1.13}$$

and

$$\hat{P} = \mathrm{i}\,p_{\mathrm{zpf}}\left(\hat{c}^{\dagger} - \hat{c}\right) \tag{1.14}$$

where $x_{\mathrm{zpf}} = \sqrt{\hbar/\left(2m_{\mathrm{eff}}\omega\right)}$ and $p_{\mathrm{zpf}} = \sqrt{\hbar m_{\mathrm{eff}}\omega/2}$ are, respectively, the standard deviations of the zero-point motion and zero-point momentum of the oscillator. The oscillator has an effective mass m_{eff} and angular frequency ω. Throughout the rest of the thesis, $\hat{X}$ and $\hat{P}$ are normalised so that $x_{\mathrm{zpf}} = p_{\mathrm{zpf}} = 1\sqrt{2}$. The non-commutativity of operators is one of the central aspects of quantum mechanics. In particular, the non-commutativity of $\hat{X}$ and $\hat{P}$, given by $\left[\hat{X}, \hat{P}\right] = \mathrm{i}$, leads to the Heisenberg uncertainty principle

$$\mathrm{Var}\left(\hat{X}\right)\mathrm{Var}\left(\hat{P}\right) \geq \frac{1}{4}. \tag{1.15}$$

It states that upon preparing a large number of quantum systems in identical states, $\hat{\rho}$, measurements of $\hat{X}$ on some of these systems and measurements of $\hat{P}$ in others give rise to variances in the obtained measurement outcomes that satisfy Eqn. (1.15). Gaussian pure states saturate the inequality given by the Heisenberg uncertainty principle. More details about Gaussian states will be covered in the next chapter.

1.5 Quantum metrology structure

A measurement process can be divided into three stages: state preparation, interaction with the system and measurement of the modified probe. Appropriate choice of the input states ensures that the optimal amount of information is extracted about the studied system and suitable measurements ensure that all this information is read out. The following chapters expand the relevant aspects of these stages for the works presented in parts II and III of this thesis.

Chapter 2

State preparation and interaction with the studied system

States relevant for this thesis are the definite-particle number states, with emphasis on Holland-Burnett (HB) states [9], and Gaussian states, with emphasis on thermal states. The Gaussian state evolution is considered in part II, where the aim is to experimentally demonstrate cooling of the mechanical motion of an optomechanical system. Definite particle number states are considered in part III which presents theoretical studies of quantum limits in the simultaneous estimation of phase and phase diffusion.

2.1 Definite particle number states

Number states $|n\rangle$ are the eigenstates of the number operator $\hat{n} = \hat{c}^\dagger \hat{c}$, where $\hat{c}^\dagger$ and $\hat{c}$ are the creation and annihilation operators introduced in section 1.4.3. They are states with a definite-particle number n. The action of $\hat{n}$ on $|n\rangle$ gives

$$\hat{n}|n\rangle = n|n\rangle. \tag{2.1}$$

Acting with $\hat{c}^\dagger$ and $\hat{c}$ on $|n\rangle$ results in

$$\hat{c}^\dagger|n\rangle = \sqrt{n+1}|n+1\rangle \tag{2.2}$$

and

$$\hat{c}|n\rangle = \sqrt{n}|n-1\rangle \tag{2.3}$$

respectively. Therefore, $\hat{c}^\dagger$ adds a particle to the state whereas $\hat{c}$ subtracts a particle from the state. A number state can be expressed in terms of the creation operator $\hat{c}^\dagger$ acting on a vacuum state $|0\rangle$ as follows

$$|n\rangle = \frac{\left(\hat{c}^\dagger\right)^n}{\sqrt{n!}}|0\rangle. \tag{2.4}$$

States with a definite-particle number are important for metrology from the conceptual point of view. For a fixed amount of resources, defined as the total number of particles in the state $(2K)$, they allow improving the precision in parameter estimation protocols when compared to the classical schemes [10]. More precisely, they allow achieving the so-called Heisenberg scaling of $1/(2K)$ in the estimation precision while the best classical possible scaling is $1/\sqrt{2K}$ [4]. An iconic example of definite-particle number probe states that reach the Heisenberg scaling in phase estimation protocols are N00N states [10].

2.1.1 N00N states

A two-mode N00N state is a superposition state with all particles ($2K$) in one mode and zero particles in the other mode, and vice-versa for the remaining superposition element. Mathematically, it is expressed as

$$|\psi\rangle_{\mathrm{N00N}} = \frac{1}{\sqrt{2}}\left(|2K,0\rangle + |0,2K\rangle\right). \tag{2.5}$$

While these states can achieve the desired Heisenberg scaling in phase estimation precision, their advantage quickly disappears in the presence of loss [10, 11]. They are also challenging to prepare and post-selection methods are often employed.

2.1.2 Holland-Burnett states

Holland-Burnett states also allow reaching the Heisenberg scaling in phase estimation protocols [9]. They can be defined as

$$|\psi_{HB}\rangle = \sum_{n=0}^{K} b_n |2n, 2K-2n\rangle, \tag{2.6}$$

where $b_n = \sqrt{(2n)!\,(2K-2n)!}/\left(2^K n!\,(K-n)!\right)$. Preparation of HB states involves interfering two equal number states on a 50/50 beam splitter. While this is still a challenging task, it is more feasible when compared to N00N states. HB states are also more resilient to loss since loss of a particle in one of the superposition elements still leaves the other superposition elements to carry the phase information.

Although definite-particle number states for sensing applications have many practical challenges, they form a backbone for quantum metrology and are important to study from the fundamental science point of view.

2.2 Gaussian states

Gaussian states can be defined as states whose Wigner function is Gaussian. The Wigner function is a quasiprobability distribution that gives a representation of a quantum state in phase space. For a general N-mode state, $\hat{\rho}$, it takes the form [12]

$$W_{\rho}\left(\boldsymbol{x},\boldsymbol{p}\right)=\frac{1}{(\pi)^{N}}\int\left\langle\boldsymbol{x}+\boldsymbol{x}'|\hat{\rho}|\boldsymbol{x}-\boldsymbol{x}'\right\rangle\mathrm{e}^{2\mathrm{i}\boldsymbol{x}'\cdot\boldsymbol{p}}\mathrm{d}^{N}\boldsymbol{x}',\tag{2.7}$$

where $\boldsymbol{x}=(x_1,x_2,...,x_N)^{\mathrm{T}}$ and $\boldsymbol{p}=\left(p_1,p_2,...,p_N\right)^{\mathrm{T}}$ denote vectors of length N containing the possible position and momentum values for each mode in $\hat{\rho}$, and $|\boldsymbol{x}\rangle=|x_1,x_2,...,x_N\rangle$ are the corresponding position eigenstates. Some of the important properties of the Wigner function include the following. Its marginal distributions are true probability distributions

$$\begin{aligned}\int W_{\rho}\left(x,p\right)\mathrm{d}x&=\langle p|\hat{\rho}|p\rangle\\ \int W_{\rho}\left(x,p\right)\mathrm{d}p&=\langle x|\hat{\rho}|x\rangle\end{aligned}\tag{2.8}$$

and the overlap between two states, $\hat{\rho}_1$ and $\hat{\rho}_2$, is determined by the product of their correspoonding Wigner functions integrated over all phase space

$$\mathrm{Tr}\left[\hat{\rho}_1\hat{\rho}_2\right]=\pi\int_x\int_p W_{\rho_1}\left(x,p\right)W_{\rho_2}\left(x,p\right)\mathrm{d}x\mathrm{d}p.\tag{2.9}$$

A Gaussian N-mode state, $\hat{\rho}_{\mathrm{G}}$, can be fully described by its first and second moments. The first moments read $\langle\hat{\boldsymbol{r}}\rangle=\left(\left\langle\hat{X}_1,\hat{P}_1,\hat{X}_2,\hat{P}_2,...,\hat{X}_N,\hat{P}_N\right\rangle\right)^{\mathrm{T}}$, whereas the covariance matrix **Cov** has elements defined as $2\sigma_{jk}^2=\left\langle\hat{r}_j\hat{r}_k+\hat{r}_k\hat{r}_j\right\rangle-2\left\langle\hat{r}_j\right\rangle\langle\hat{r}_k\rangle$. The Wigner function representation of the Gaussian state, $\hat{\rho}_{\mathrm{G}}$, as a function of coordinate $r\in\mathbb{R}^{2N}$ reads [13]

$$W_{\rho_{\mathrm{G}}}(\boldsymbol{r})=\frac{1}{(\pi)^{N}}\frac{1}{\sqrt{\det\left(\mathbf{Cov}\right)}}\mathrm{e}^{-(\boldsymbol{r}-\langle\hat{\boldsymbol{r}}\rangle)^{\mathrm{T}}\mathbf{Cov}^{-1}(\boldsymbol{r}-\langle\hat{\boldsymbol{r}}\rangle)},\tag{2.10}$$

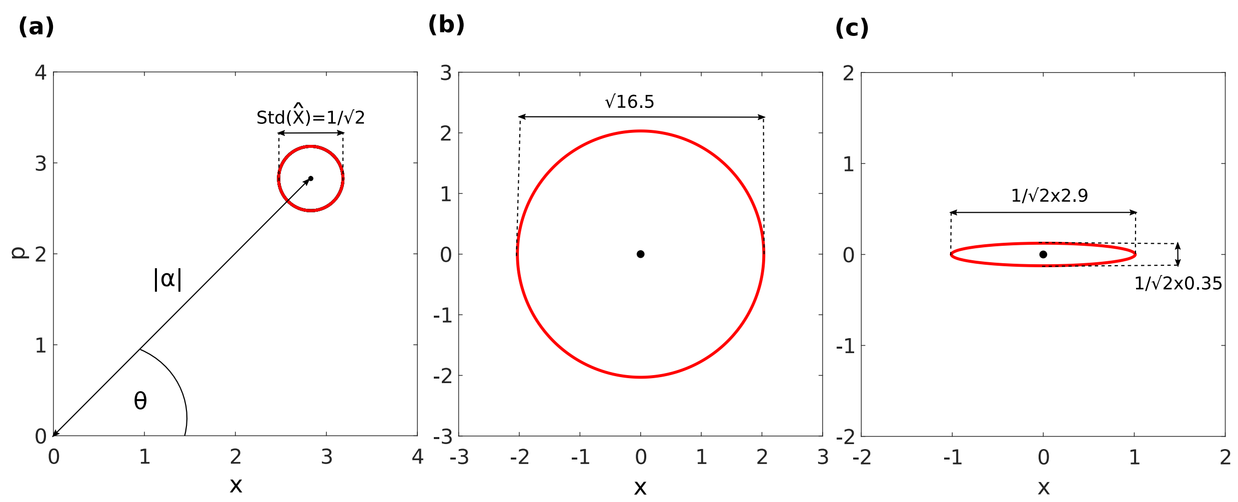

Figure 2.1: Phase space plots of **(a)** coherent state **(b)** thermal state and **(c)** vacuum squeezed state. All the plots assume an average occupation number of $\langle \hat{n} \rangle = 16$. The red lines are contours at one standard deviation (std) of the quadratures associated with the corresponding states.

where $\boldsymbol{r} = (r_1, r_2, ..., r_{2N})^{\mathrm{T}} = \left(x_1, p_1, x_2, p_2, ..., x_N, p_N\right)^{\mathrm{T}}$. State, $\hat{\rho}_{\mathrm{G}}$, will preserve its Gaussian nature under unitary transformations whose exponents are at most quadratic operators [13]. This is an important property for the work presented in part II of this thesis.

A common example of pure Gaussian states is the coherent state which forms the basis of many quantum optics studies.

2.2.1 Coherent states

Coherent states, denoted by $|\alpha\rangle$, are the eigenstates of the annihilation operator $\hat{c}$ and therefore satisfy

$$\hat{c}|\alpha\rangle = \alpha|\alpha\rangle, \tag{2.11}$$

where $\alpha \in \mathbb{C}$ and can be expressed as $\alpha = |\alpha|\mathrm{e}^{\mathrm{i}\theta}$. These states saturate the Heisenberg uncertainty principle in Eqn. (1.15) with $\mathrm{Var}\left(\hat{X}\right) = \mathrm{Var}\left(\hat{P}\right) = 1/2$. In a phase space representation, they can be imagined as a displaced vacuum state by letting a displacement operator $\hat{D} = \mathrm{e}^{\alpha\hat{a}^\dagger - \alpha^*\hat{a}}$

act on the vacuum state $|0\rangle$. This is shown in Fig. (2.1a). In the number state basis, they can be expressed as

$$|\alpha\rangle = \mathrm{e}^{-|\alpha|^2/2} \sum_{n=0}^{\infty} \frac{\alpha^n}{(n!)^{1/2}} |n\rangle \tag{2.12}$$

with the average photon number of $\langle \hat{n} \rangle = \langle \alpha | \hat{n} | \alpha \rangle = |\alpha|^2$.

2.2.2 Thermal states

While the quantum noise in thermal states is typically hidden behind the thermal noise, these states are usually the starting point for most of the optomechanical platforms which includes the work presented in part II. Thermal states are an example of mixed states. Their corresponding density matrix, $\hat{\rho}_{\mathrm{th}}$, in the number state basis reads

$$\hat{\rho}_{\mathrm{th}} = \sum_{n=0} \frac{\bar{n}_{\mathrm{b}}^n}{(1+\bar{n}_{\mathrm{b}})^{n+1}} |n\rangle\langle n| \tag{2.13}$$

with $\bar{n}_{\mathrm{b}} = \langle \hat{n} \rangle = \left(e^{\hbar\omega/k_{\mathrm{b}}T} - 1\right)^{-1}$, where ω is the angular frequency, k_{b} is the Boltzmann constant and T is the temperature. In the coherent state basis, $\hat{\rho}_{\mathrm{th}}$ is given by

$$\hat{\rho}_{\mathrm{th}} = \frac{1}{\pi \bar{n}_{\mathrm{b}}} \int \mathrm{e}^{-|\alpha|^2/\bar{n}_{\mathrm{b}}} |\alpha\rangle\langle\alpha| \mathrm{d}^2\alpha, \tag{2.14}$$

where $\mathrm{d}^2\alpha = \mathrm{d}\,\mathrm{Re}\,(\alpha)\,\mathrm{d}\,\mathrm{Im}\,(\alpha)$. The variance of operators $\hat{X}$ and $\hat{P}$ for thermal states is $\mathrm{Var}\left(\hat{X}\right) = \mathrm{Var}\left(\hat{P}\right) = \bar{n}_{\mathrm{b}} + 1/2$. A phase space plot of a thermal state is shown in Fig. (2.1b).

2.2.3 Squeezed states

In general, squeezed states can relate to any state (pure or mixed) in which the uncertainty of one of the quadratures is below that of vacuum. However, squeezed vacuum states are of particular interest in quantum metrology. Similarly to coherent states, described in section 2.2.1, they saturate the Heisenberg uncertainty principle in Eqn. (1.15). The uncertainty in one of the quadratures is reduced below that of vacuum at the expense of increased uncertainty in the other quadrature. This is illustrated pictorially in Fig. (2.1c). More formally, a single mode squeezed vacuum state $|r\rangle$ can be defined through a squeezing operator $\hat{S}(r) = \mathrm{e}^{1/2\left(r^* \hat{c}^2 - r\hat{c}^{\dagger 2}\right)}$ acting on a vacuum state $|0\rangle$ [10]

$$|r\rangle = \hat{S}(r)\,|0\rangle, \tag{2.15}$$

where $r = |r|\mathrm{e}^{\mathrm{i}\zeta}$. The state has minimum and maximum quadrature variances of $\mathrm{Var}_{\mathrm{min}} = 1/2\mathrm{e}^{-r}$ and $\mathrm{Var}_{\mathrm{max}} = 1/2\mathrm{e}^{r}$ respectively. The mean particle number in $|r\rangle$ is $\langle \hat{n} \rangle = 1/4\left(\mathrm{e}^{2r} - \mathrm{e}^{-2r}\right)$.

Vacuum squeezed states are used to improve the sensitivity of gravitational wave detectors which rely on optical interferometry [10]. One input of the interferometer is fed with coherent light whereas the other input is typically left empty. Injecting vacuum squeezed light into the empty input of the interferometer improves its phase sensitivity if the phase of the coherent state is appropriately matched with the phase of the low noise quadrature of the squeezed light.

2.3 System interaction

The system that the input probe state interacts with can be parameterised and identification of the parameters yields knowledge about the studied system. A typical parameter of interest in quantum metrology settings is the interferometric phase [10] induced by a unitary operation $\hat{U}_\phi = \mathrm{e}^{\mathrm{i}\phi\hat{n}}$. Physical phenomena, such as gravitational waves [14, 15, 16], changes in refractive index [17], measurements of displacements, magnetic and electric fields [18] can be associated with a unitary evolution. Noise parameters, such as diffusion and loss, can also be of interest and they are associated with the non-unitary evolution. The aspect of unitary and non-unitary parameters in the estimation process is discussed in part III, and the non-unitary system evolution due to the interaction with the thermal environment is the topic of part II.

Chapter 3

Measurements

Measurement of the evolved probe state allows reading out the information about the system acquired by the probe. Parts II and III of this thesis explore the measurement aspect in different contexts. Part II considers continuous heterodyne measurement of the optical mode in an optomechanical platform to learn about the phase space trajectories of the relevant mechanical mode. This subsequently cools the oscillator's mechanical motion by means of reducing the uncertainty associated with the mechanical quadratures. Part III, on the other hand, studies quantum limits in a multi-parameter estimation process, where the probabilities associated with the measurement outcomes determine the precision with which the relevant parameters can be estimated. Here, a general POVM formalism is adopted with the example of the canonical phase measurement and a primary focus on the class of projective measurements.

3.1 Canonical phase measurement

The canonical phase measurement measures the phase ϕ of a field. It constitutes an important role in the problem of finding the quantum phase observable [7, 19, 20]. The POVM set of such measurement satisfies the completeness relation $\int_0^{2\pi} \hat{E}_\phi \mathrm{d}\phi = 1$ with $\hat{E}_\phi = 1/(2\pi)\,|\phi\rangle\langle\phi|$, where $|\phi\rangle = \sum_{n=0}^{\infty} \mathrm{e}^{-\mathrm{i}\phi\hat{n}}|n\rangle$ is the so-called Susskind-Glogower phase state [19]. For a two-mode field with phase ϕ in between, phase states can also be defined and in the case of a two-mode HB state, they take the form $|\phi\rangle = \sum_{n=0}^{K} \mathrm{e}^{\mathrm{i}n\phi}|n, 2K-n\rangle$. The phase states $|\phi\rangle$ are not eigenstates of any Hermitian operator and therefore are not directly realisable from the experimental point of view. They are however important for the fundamental measurement science.

More experimentally feasible measurements include homodyne and heterodyne detection which are the topics of the next sections.

3.2 Homodyne and heterodyne detection

3.2.1 Homodyne detection

A balanced optical homodyne detector measures a quadrature of an optical field mode ($\hat{c}_1$) by interfering the signal of interest with the on-resonance reference light field ($\hat{c}_2$) in a strong coherent state on a 50/50 beam splitter. The resulting signal is measured by two photodetectors and the photocurrents subtracted to yield a quadrature value. The measured quadrature can be expressed as $\hat{X}_\theta(t) = 1/\sqrt{2}\left(\hat{c}_1^\dagger(t)\,\mathrm{e}^{\mathrm{i}\theta} + \hat{c}(t)\,\mathrm{e}^{-\mathrm{i}\theta}\right)$ and its phase angle θ is determined by the phase of the reference field which is also referred to as the local oscillator. The homodyne detection scheme is shown in Fig. (3.1). After the beam splitter transformation, annihilation operators $\hat{c}_1$

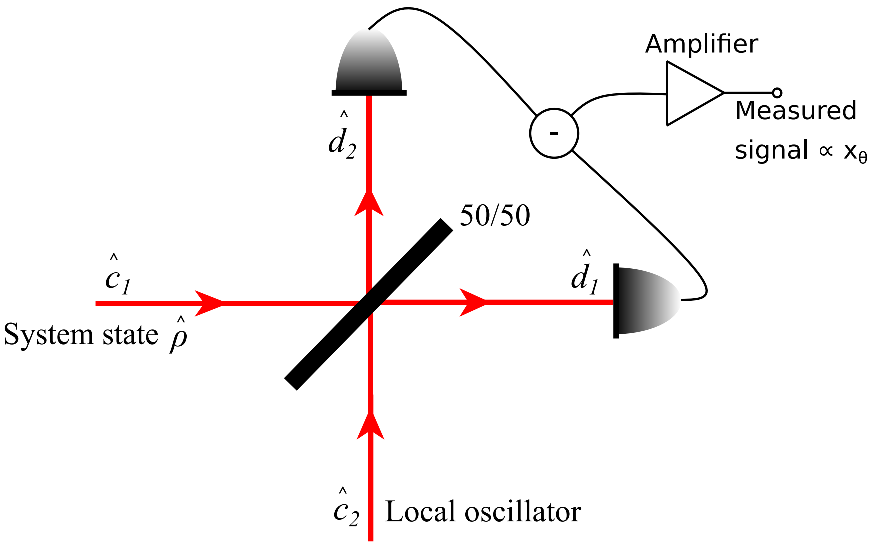

Figure 3.1: Schematic of balanced homodyne detection scheme. Signal field mode $\hat{c}_1$, in state $\hat{\rho}$, interferes with the local oscillator in mode $\hat{c}_2$ on a 50/50 beam splitter. The resulting signals in modes $\hat{d}_1$ and $\hat{d}_2$ are measured by two photodetectors and the photocurrents are subtracted and the difference amplified to yield the final signal proportional to the samples of the quadrature $\hat{X}_\theta$ of state $\hat{\rho}$. The phase θ of the measured quadrature is determined by the phase of the local oscillator.

and $\hat{c}_2$ transform to

$$\begin{aligned} \hat{d}_1 &= \frac{1}{\sqrt{2}}\left(\hat{c}_1 + \mathrm{i}\hat{c}_2\right), \\ \hat{d}_2 &= \frac{1}{\sqrt{2}}\left(\hat{c}_2 + \mathrm{i}\hat{c}_1\right) \end{aligned} \tag{3.1}$$

respectively. The intensity measured by the two photodetectors is proportional to the number of photons present in modes 1 and 2. It can therefore be represented by the following number operators

$$\begin{aligned} \hat{N}_1 &= \hat{d}_1^\dagger \hat{d}_1 = \frac{1}{2}\left(\hat{c}_1^\dagger \hat{c}_1 + \mathrm{i}\hat{c}_1^\dagger \hat{c}_2 - \mathrm{i}\hat{c}_2^\dagger \hat{c}_1 + \hat{c}_2^\dagger \hat{c}_2\right), \\ \hat{N}_2 &= \hat{d}_2^\dagger \hat{d}_2 = \frac{1}{2}\left(\hat{c}_2^\dagger \hat{c}_2 + \mathrm{i}\hat{c}_2^\dagger \hat{c}_1 - \mathrm{i}\hat{c}_1^\dagger \hat{c}_2 + \hat{c}_1^\dagger \hat{c}_1\right) \end{aligned} \tag{3.2}$$

for modes 1 and 2 respectively. Subtracting $\hat{N}_1$ and $\hat{N}_2$ gives

$$\Delta\hat{N}_{\text{hom}} = \hat{N}_2 - \hat{N}_1 = \mathrm{i}\left(\hat{c}_2^\dagger \hat{c}_1 - \hat{c}_1^\dagger \hat{c}_2\right). \tag{3.3}$$

Since mode $\hat{c}_2$ corresponds to the reference field which is in a strong coherent state, it can be represented as a classical field of amplitude $\alpha_{\text{LO}} = |\alpha_{\text{LO}}|\mathrm{e}^{\mathrm{i}\theta}$. This leads to a photocurrent difference of $\Delta\hat{N}_{\text{hom}} = |\alpha_{\text{LO}}|\left(\hat{c}_1^\dagger \mathrm{e}^{\mathrm{i}(\theta-\pi/2)} + \hat{c}_1 \mathrm{e}^{-\mathrm{i}(\theta-\pi/2)}\right)$. The $\pi/2$ term present in the exponent can be absorbed into θ which gives

$$\Delta\hat{N}_{\text{hom}} = |\alpha_{\text{LO}}|\left(\hat{c}_1^\dagger \mathrm{e}^{\mathrm{i}\theta} + \hat{c}_1 \mathrm{e}^{-\mathrm{i}\theta}\right) = \sqrt{2}|\alpha_{\text{LO}}|\hat{X}_\theta. \tag{3.4}$$

Homodyne detection therefore indeed corresponds to a measurement of a single quadrature of the probed field.

3.2.2 Heterodyne detection

In heterodyne detection, the local oscillator is detuned from the system frequency by $\omega_{\text{HET}}/(2\pi)$. The effect of the detuning is to replace $\hat{c}_1$ with $\hat{c}_1 \mathrm{e}^{-\mathrm{i}\omega_{\text{HET}} t}$ which results in the photocurrent difference of

$$\Delta\hat{N}_{\text{het}} = |\alpha_{\text{LO}}|\left(\hat{c}_1^\dagger \mathrm{e}^{\mathrm{i}(\theta+\omega_{\text{HET}} t)} + \hat{c}_1 \mathrm{e}^{-\mathrm{i}(\theta+\omega_{\text{HET}} t)}\right) = \sqrt{2}|\alpha_{\text{LO}}|\hat{X}_{(\theta+\omega_{\text{HET}} t)}. \tag{3.5}$$

As a result, the measured quadrature rotates at the frequency $\omega_{\text{HET}}/(2\pi)$. If the system evolution time is appreciably longer than $2\pi/\omega_{\text{HET}}$ then information about two orthogonal quadratures can be obtained.

Part II

Optomechanical state estimation and preparation by measurement

Chapter 4

Introduction to optomechanics

4.1 Background and motivation

The field of optomechanics explores the interactions between electromagnetic radiation and mechanical systems to allow control of the mechanical motion. Some of the first examples of optomechanical systems employed cantilevers inside microwave cavities coupled by the radiation pressure force [21, 22, 23, 24]. This research direction was strongly motivated by the development of gravitational wave detectors whose desired sensitivity encouraged studies of such platforms and their fundamental limits. The quantum limits associated with the sensitivity of optomechanical systems were first investigated by Braginskiǐ and colleagues in the 1960s, see for instance Ref. [25]. Braginskiǐ pointed out the importance of radiation pressure quantum fluctuations in cooling the mechanical motion. Appropriate control of the experimental parameters can reduce the temperature of the mechanical mode and also allow efficient swap operations between the optics and mechanics if strong interactions are invoked. This finds applications not only in fundamental science, but also in fields such as metrology and information processing [26, 27, 28, 29]. Mechanical oscillators can be used as a precise sensor to detect different kinds of forces [27, 30, 31]. Moreover, the field has explored different cooling approaches such as sideband cooling [32, 33, 34, 35, 36, 37, 38, 39, 40], conditional state preparation [41] and feedback cooling [42, 43, 44, 45, 46].

While microwave cavities were convenient to use with the technology available in the 1970s, reaching the regime of low thermal microwave occupation requires demanding cryogenic techniques. This is because at such low wavelengths the microwave thermal occupation is still above the ground state even at low environmental temperatures. For instance, a 10 GHz microwave signal has a thermal occupation number of 2 at the environmental temperature of 1 K. Working in the optical regime has the advantage of having the optical thermal occupation very close to vacuum even at room temperatures and thus making it more feasible to achieve mechanical ground states without cryogenic systems. Therefore, the experimental efforts expanded towards exploring interactions between optical and mechanical modes [47].

Further technological advances allowed miniaturization of mechanical elements and fabrication of high finesse and high quality factor optical cavities essential for the exploration of the quantum regime. Nowadays, many optomechanical systems have been investigated including: membranes and nano-rods inside Fabry-Perot resonators, whispering gallery resonators, photonic crystals and evanescently coupled nanobeams [26]. They allow to access different experimental parameter regimes and explore different underlying physical principles. Although the field started with the radiation pressure as the mediator of the optomechanical coupling, platforms investigating different interaction types, such as electrostriction, are now possible. In particular, such systems allow for exploring the field of Brillouin optomechanics [48] which is one of the bases for the experiment presented in this part of my thesis.

4.2 Cavity properties

A simple cavity can be constructed by positioning two highly reflective mirrors at some distance L. The cavity will support modes whose half wavelengths fit the cavity an integer number of times. Such modes are the cavity's eigenmodes and the amplitude of light injected into these eigenmodes is reinforced on each reflection from the mirrors building up the power of the optical field. The optical field also experiences some unwanted material losses and the unavoidable losses associated with coupling to external light. As a result, photons inside the cavity have a certain lifetime denoted by τ. A different type of cavity is a microresonator, for instance microsphere and microrod resonators [49, 50], where light circulates inside a material medium by means of total internal reflection. Here, the optical power build up is mainly limited by material absorption and surface scattering. Microrod resonators are of particular interest for the work presented in part II of this thesis and more details about them can be found in section 5.3 of chapter 5.

The separation between the longitudinal resonances of a cavity can be quantified by its free spectral range (FSR) which is defined as the inverse of the round trip time experienced by the photons inside the cavity. For a microrod resonator of diameter d and refractive index n, the FSR in the angular frequency units can be expressed as,

$$\Delta\omega_{\mathrm{FSR}} = \frac{2c}{dn}, \tag{4.1}$$

where c is the speed of light in free space. The transverse mode structure of microrod resonators allows for the existence of optical resonances within the free spectral range. This allows selecting discrete optical modes separated by an appropriate frequency distance which is very important for the experiment presented in this part of the thesis. A frequency separation $\Delta\omega$

can be converted into the equivalent wavelength separation $\Delta\lambda$ using

$$\Delta\lambda = \frac{\lambda\Delta\omega}{\frac{2\pi c}{\lambda} + \Delta\omega}, \tag{4.2}$$

where λ is the wavelength of light. The property of a cavity that measures its ability to store energy is the quality (Q) factor defined as

$$Q = \frac{\omega_{\text{cav}}}{2\kappa}, \tag{4.3}$$

where $\omega_{\text{cav}}/2\pi$ is the cavity resonance frequency and $\kappa = \pi/\tau$ is the cavity amplitude decay rate in the units of angular frequency. The ability to store light can also be quantified by the number of round trips that a photon takes before it leaks out of the cavity. This is encapsulated in a quantity called finesse given by,

$$F = \frac{\Delta\omega_{\text{FSR}}}{2\kappa}. \tag{4.4}$$

The amplitude decay rate κ constitutes the earlier mentioned two types of losses, the external coupling losses κ_{e} and any other internal losses κ_{i} such that

$$\kappa = \kappa_{\text{e}} + \kappa_{\text{i}}. \tag{4.5}$$

The power at the input of the cavity P_{in} is enhanced resulting in the intracavity power

$$P_{\text{cav}} = \frac{2P_{\text{in}}F\kappa\kappa_{\text{e}}}{\pi\left(\kappa^2 + \Delta_{\text{L}}^2\right)} = \frac{P_{\text{in}}F\left(1 - T_\nu\right)}{\pi\left(1 \pm \sqrt{T_{\text{o}}}\right)}, \tag{4.6}$$

where T_{o} is the cavity transmission on resonance, T_ν is the actual cavity transmission and Δ_{L} is the laser detuning with respect to the optical mode. In the denominator, $\pm$ applies to under-and over-coupled conditions respectively.

4.3 Radiation-pressure-based optomechanics

Radiation pressure relates to the transfer of momentum from light to an object that it interacts with. This force was first theorized by Kepler in the 17th century who noted that tails of comets point away from the Sun during their transits. Although radiation pressure has a big impact on the dynamics of objects in outer space, we do not perceive much of its influence on the Earth. It does however dictates the dynamics of many optomechanical systems. In 1966, Braginskiĭ and Manukin formulated a classical description of this effect for mirrors inside the Fabry-Perot resonator [21]. In their work, radiation pressure introduces positive or negative rigidity in the mechanical oscillator depending on the sign of the optical cavity detuning. Positive detuning amplifies whereas negative detuning damps the mechanical motion. This dynamical effect of radiation pressure on the mechanical motion is termed as dynamical backaction [51].

Throughout part II, the optical and mechanical modes are denoted by $\hat{a}$ and $\hat{b}$ respectively. The optical and mechanical amplitude decay rates in angular frequency units are represented by κ and γ_{m} respectively. The quadrature operators are normalised such that the variance of vacuum is 1/2 unless stated otherwise. The resulting position and momentum quadrature operators for an arbitrary mode operator $\hat{c}$ are defined by

$$\hat{X} = \left(\hat{c}^{\dagger} + \hat{c}\right)/\sqrt{2} \tag{4.7}$$

and

$$\hat{P} = \mathrm{i}\left(\hat{c}^{\dagger} - \hat{c}\right)/\sqrt{2} \tag{4.8}$$

respectively.

The following calculation considers a mode description of the optical and mechanical oscillators to derive the cooling and heating Hamiltonians for a cantilever coupled via radiation pressure to a Fabry-Perot cavity of length L. The optical cavity resonance frequency is $\omega_{\mathrm{cav}}/2\pi$ and the mechanical frequency is $\omega_{\mathrm{m}}/2\pi$. The oscillator has an effective mass of m_{eff}.

The uncoupled optical and mechanical Hamiltonian $\hat{H}_0$ can be represented by two harmonic oscillators,

$$\hat{H}_0 = \hbar\omega_{\mathrm{cav}}\hat{a}^\dagger\hat{a} + \hbar\omega_{\mathrm{m}}\hat{b}^\dagger\hat{b}. \tag{4.9}$$

The above Hamiltonian does not include the dissipation and cavity driving terms, but their effect on the interaction Hamiltonian is considered qualitatively at the end of this section. The displacement Δx of the cantilever from the original position $x = 0$ changes the cavity length and therefore its resonance frequency. For small displacements, we can Taylor expand ω_{cav} with respect to x about $x = 0$ and keep terms up to the linear order only,

$$\omega_{\mathrm{cav}}(x) \approx \omega_{\mathrm{cav},x=0} + x\partial\omega_{\mathrm{cav}}/\partial x. \tag{4.10}$$

The term $-\partial\omega_{\mathrm{cav}}/\partial x$ describes the cavity frequency shift per displacement and is denoted by D which for this example is ω_{cav}/L. The Hamiltonian $\hat{H}_0$ can therefore be written as

$$\hat{H}_0 = \hbar\left(\omega_{\mathrm{cav},x=0} - D\hat{X}_{\mathrm{m}}\right)\hat{a}^\dagger\hat{a} + \hbar\omega_{\mathrm{m}}\hat{b}^\dagger\hat{b}, \tag{4.11}$$

where $\hat{X}_{\mathrm{m}}$ is the mechanical position quadrature operator defined in Eqn. (4.7) for mode $\hat{b}$. The interaction part $\hat{H}_{\text{int}}$ of this Hamiltonian is therefore

$$\hat{H}_{\text{int}} = -\hbar g_0 \hat{a}^\dagger \hat{a} \left(\hat{b}^\dagger + \hat{b}\right), \tag{4.12}$$

where $g_0 = D/\sqrt{2}$ represents the coupling between the optical number operator and the mechanical position quadrature in the units of angular frequency per $\left(1/\sqrt{2}\right)\sqrt{\text{Var}\left(\hat{X}_{\text{m},0}\right)}$. Here, $\hat{X}_{\text{m},0}$ is the mechanical position quadrature ground state with variance given by $\text{Var}\left(\hat{X}_{\text{m},0}\right) = \hbar/\left(2m_{\text{eff}}\omega_{\text{m}}\right)$. Using the linearized approximate description of cavity optomechanics [26], the optical field can be considered as quantum fluctuations $\delta\hat{a}$ around an average coherent amplitude α,

$$\hat{a} = \alpha + \delta\hat{a}. \tag{4.13}$$

The interaction Hamiltonian then becomes,

$$\hat{H}_{\text{int}} = -\hbar g_0 \left(\alpha^\star + \delta\hat{a}^\dagger\right)\left(\alpha + \delta\hat{a}\right)\left(\hat{b}^\dagger + \hat{b}\right). \tag{4.14}$$

The term containing $|\alpha|^2$ implies an average radiation pressure force which only shifts the spatial origin of the mechanical oscillator and therefore can be omitted. The term containing $\delta\hat{a}^\dagger\delta\hat{a}$ can also be ignored as it is $|\alpha|$ times smaller compared with the remaining terms. This results in,

$$\hat{H}_{\text{int}} = -\hbar g_0 \left(\alpha^\star\delta\hat{a} + \alpha\delta\hat{a}^\dagger\right)\left(\hat{b}^\dagger + \hat{b}\right). \tag{4.15}$$

Writing $\alpha = |\alpha| \mathrm{e}^{\mathrm{i}\phi}$ and taking $\phi = 0$, we get

$$\hat{H}_{\text{int}} = -\hbar g_0 |\alpha| \left(\delta\hat{a} + \delta\hat{a}^\dagger\right)\left(\hat{b}^\dagger + \hat{b}\right) \tag{4.16}$$

and expanding the brackets,

$$\hat{H}_{\rm int} = -\hbar g_0 \mid \alpha \mid \left(\delta\hat{a}\hat{b}^\dagger + \delta\hat{a}^\dagger\hat{b} + \delta\hat{a}\hat{b} + \delta\hat{a}^\dagger\hat{b}^\dagger\right). \tag{4.17}$$

The radiation pressure force is provided by pumping the optical cavity mode with a laser light. The detuning of the pump laser $\Delta_{\rm L}$ with respect to the optical cavity determines the dynamics of the system. In the resolved sideband regime ($\kappa \ll \omega_{\rm m}$), two interesting scenarios can be distinguished.

1. $\Delta_{\rm L} = -\omega_{\rm m}$ – here laser light is red-detuned with respect to the cavity resonance. This strongly suppresses the last two terms of $\hat{H}_{\rm int}$ in Eqn. (4.17) as they are not resonant. Therefore, the first two terms are only relevant and form the beam-splitter (BS) interaction, $\hat{H}_{\rm BS} = -\hbar g_0 \mid \alpha \mid \left(\delta\hat{a}\hat{b}^\dagger + \delta\hat{a}^\dagger\hat{b}\right)$, which leads to cooling of a mechanical motion.

2. $\Delta_{\rm L} = \omega_{\rm m}$ – here laser light is blue-detuned with respect to the cavity resonance and the last two terms are dominant. Therefore, the interaction Hamiltonian represents a two-mode squeezing, $\hat{H}_{\rm TMS} = -\hbar g_0 \mid \alpha \mid \left(\delta\hat{a}\hat{b} + \delta\hat{a}^\dagger\hat{b}^\dagger\right)$, which leads to growth of energy in both modes if no dissipation is present.

The red-detuned scenario forms the backbone for sideband cooling [36]. It is important to note that the mechanical motion cannot be indefinitely cooled due to the quantum backaction limit [40]. It arises due to the asymmetry between the rates at which phonons are absorbed and emitted from the mechanical mode due to the presence of the radiation pressure force [26, 52]. The absorption and emission processes are proportional to $(\bar{n}+1)$ and $\bar{n}$ accordingly, where $\bar{n}$ is the average phonon number in the mechanical mode. This leads to a non-zero minimum phonon occupation even when there is no coupling to the mechanical thermal bath ($\gamma_{\rm m} = 0$).

In the resolved sideband regime ($\omega_m >> \kappa$), this gives a minimum phonon number of $\bar{n}_{min} = (\kappa/2\omega_m)^2$.

4.4 Brillouin optomechanics: electrostriction and photoelasticity

In general, light scattering results from fluctuations of optical properties in a material medium that the light passes. There are different light scattering processes, such as Raman, Rayleigh and Brillouin scattering, leading to different physical phenomena. The scattered light is shifted to higher and lower frequency components known as Stokes and anti-Stokes components respectively. The work outlined in this part is based on Brillouin scattering which is the scattering of light (or photons) from acoustic waves (or phonons). It was first studied by Leon Brillouin in 1922 [53] and is a type of inelastic scattering. During this interaction, photons in the pump mode are scattered to the Stokes and anti-Stokes modes by creating and annihilating phonons from the acoustic (mechanical) mode respectively. Energy and momentum of the photon-phonon system are conserved which implies,

$$\begin{aligned} \omega_p &= \omega_S + \omega_m \\ \omega_p + \omega_m &= \omega_{aS} \end{aligned} \tag{4.18}$$

and

$$\begin{aligned} \vec{k}_p &= \vec{k}_S + \vec{k}_m \\ \vec{k}_p + \vec{k}_m &= \vec{k}_{aS}. \end{aligned} \tag{4.19}$$

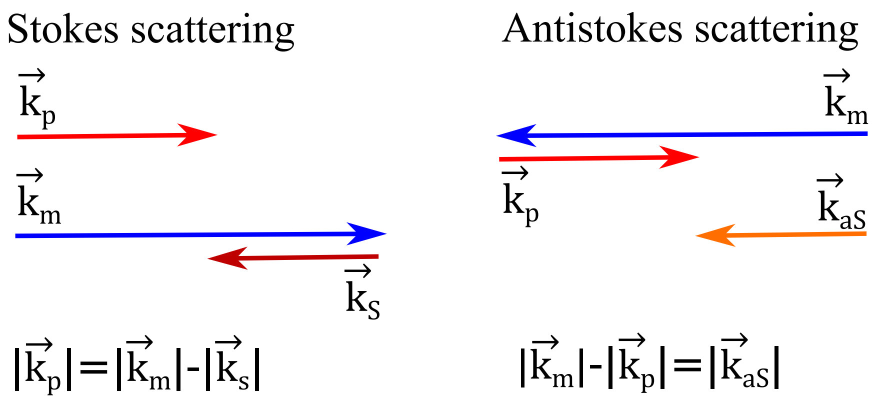

Figure 4.1: Conservation of wave vector $\vec{k}$ for the Stokes (left) and anti-Stokes (right) scattering processes. Subscripts S, aS, m and p refer to Stokes, anti-Stokes, mechanical and pump modes respectively. When $|\vec{k}_\mathrm{m}|>|\vec{k}_\mathrm{p}|$, the scattered light is enhanced in the backwards direction relative to the incident pump light.

Throughout the rest of part II, ω and $\vec{k}$ indicate angular frequency and wavevector respectively. Subscripts S, aS, m and p refer to Stokes, anti-Stokes, mechanical and pump modes respectively. The mechanical and optical wavevectors have magnitudes, $|\vec{k}_\mathrm{m}|=\omega_\mathrm{m}/v$, $|\vec{k}_\mathrm{p}|=\omega_\mathrm{p}n/c$, $|\vec{k}_\mathrm{aS}|=\omega_\mathrm{aS}n/c$ and $|\vec{k}_\mathrm{S}|=\omega_\mathrm{S}n/c$, where n is the refractive index of the material medium, c is the speed of light in free space and v is the speed of sound in the material medium. When $|\vec{k}_\mathrm{m}|>|\vec{k}_\mathrm{p}|$ such that Eqn. (4.18) and Eqn. (4.19) are satisfied, the scattered light is enhanced in the backwards direction relative to the incident pump light. This is shown pictorially in Fig. (4.1). The phonons travel in the direction of the pump photons in the case of Stokes and in the opposite direction in the case of anti-Stokes scattering. The condition on the magnitude of momenta for the Stokes scattering process, shown in Fig. (4.1), gives

$$\frac{\omega_\mathrm{p}n}{c}=\frac{\omega_\mathrm{m}}{v}-\frac{\omega_\mathrm{S}n}{c}. \tag{4.20}$$

Using the energy conservation condition in Eqn. (4.18) and the fact that $v \ll c/n$, the above equation can be expressed as

$$\omega_{\mathrm{m}} = \frac{2\omega_{\mathrm{p}} n}{c\left(\frac{n}{c} + \frac{1}{v}\right)} \approx \frac{2\omega_{\mathrm{p}} n v}{c}. \tag{4.21}$$

Therefore, the mechanical frequency depends on the ratio of the speeds of sound and light in a given material medium.

The Stokes and anti-Stokes back scattering is the relevant scenario for the experiment presented in part II, where the studied optical fields are at telecommunication wavelengths ($\lambda_{\mathrm{p}} \approx$ 1550 nm, or equivalently $\omega_{\mathrm{p}}/2\pi \approx 194$ THz) and the considered medium is fused silica with $v = 5.97 \times 10^3$ m/sec [54] and $n = 1.47$. Using Eqn. (4.21), the resulting $|\vec{k}_{\mathrm{m}}| \approx 1.9 \times 10^6\ \mathrm{m}^{-1} > |\vec{k}_{\mathrm{p}}| \approx 0.9 \times 10^6\ \mathrm{m}^{-1}$ and $\omega_{\mathrm{m}}/2\pi \approx 11$ GHz.

The physical mechanisms responsible for the coupling of the mechanical and optical modes are electrostriction and photoelasticity. Electrostriction is the property of a material to compress under the applied electric field whereas photoelasticity describes the change of optical properties of the material under the applied mechanical stress. The incident pump field exerts an electrostrictive pressure to the material which leads to creating or annihilating phonons in the acoustic field. The acoustic field, on the other hand, photoelastically causes variations in the refractive index of the material medium leading to scattering of the incident photons into the Stokes and anti-Stokes fields.

The refractive index fluctuations can be induced by thermal phonons or by the presence of optical field. The former case leads to thermal whereas the latter case to stimulated scattering. When the incident pump light is strong, the thermal scattering process can be very efficient leading to a lot of light in the Stokes and anti-Stokes modes. Beating of the incident pump light and the Stokes light reinforces the acoustic wave. At the same time, beating of the pump

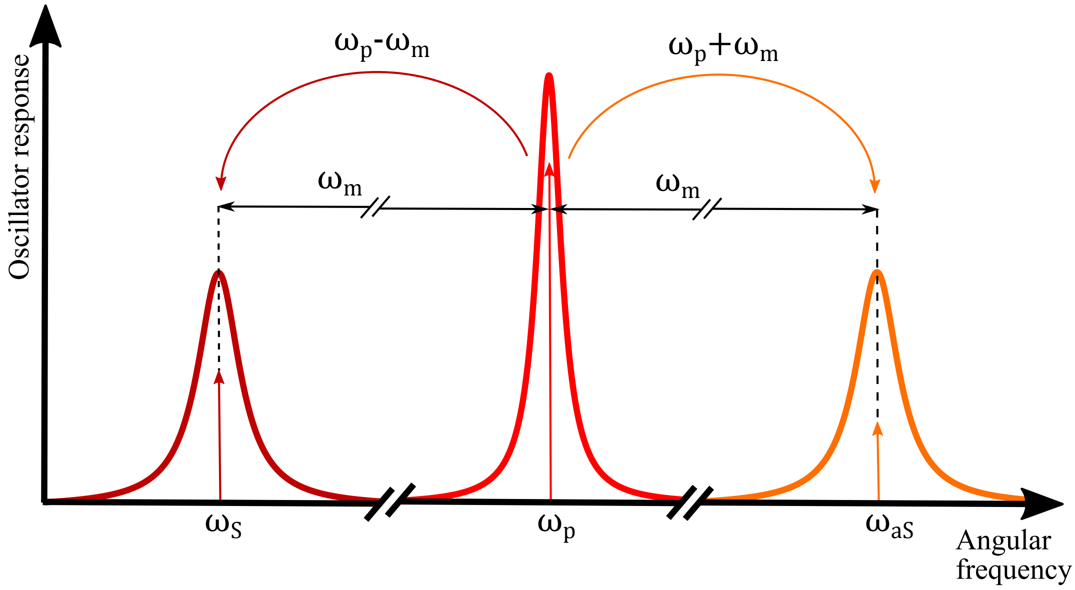

Figure 4.2: Scattering of a pump photon (red) into the Stokes (brown) and anti-Stokes (orange) modes by adding and subtracting a phonon from the mechanical mode, respectively.

light and the acoustic wave reinforces the Stokes light. This positive feedback can lead to the exponential growth of the Stokes occupation and is referred to as stimulated Brillouin scattering (SBS). This amplification process can only happen with the Stokes light as the anti-Stokes light dampens the acoustic mode and thus weakens the acoustic wave. Therefore, anti-Stokes scattering is a thermal process only.

Brillouin scattering is the interaction of four fields, pump $\hat{a}_{\mathrm{p}}$, Stokes $\hat{a}_{\mathrm{S}}$, anti-Stokes $\hat{a}_{\mathrm{aS}}$ and the mechanical field $\hat{b}$. The full interaction Hamiltonian can be written as

$$\hat{H}_{\mathrm{int}} = \hbar g_0 \left(\hat{a}_{\mathrm{p}} \hat{a}^{\dagger}_{\mathrm{aS}} \hat{b} + \hat{a}_{\mathrm{p}} \hat{a}^{\dagger}_{\mathrm{S}} \hat{b}^{\dagger} \right) + \mathrm{h.c.} \tag{4.22}$$

and the interaction is pictorially shown in Fig. (4.2). The anti-Stokes part of the Hamiltonian forms a BS interaction which can be used for cooling of the mechanical motion if the Stokes terms are suppressed.

4.5 Applications: optomechanical sensing

Optomechanics has found many applications since its beginnings in 1960s and at the time was sparked largely due to the growing interest in gravitational wave detection. Some of the many uses include,

1. Fundamental science – optomechanics allows experimental realisation of non-classical states of macroscopic objects [55, 26].
2. Information processing – strong coupling between light and mechanics permits efficient swap operations between these two modes which is very relevant for devices such as optomechanical transducers. Optical storage protocols can also be applied to optomechanical systems to store light in the mechanical excitations [56, 57]. Another example of information processing application is a tunable optical filter, where two microcavities with a certain gap in between are evanescently coupled to an optical field. Tuning of the optical resonances is possible by changing the width of the gap or applying capacitive tuning between the two resonators [58, 59].
3. Metrology – mechanical oscillators with optical readout can provide exquisite sensors. This will be the focus of the remainder of this section.

While ground state cooling has already been achieved in some optomechanical platforms [37, 38, 40, 46], it is still an active area of research. Although cryogenic systems can aid this task, they are not very practical for commercial mass production applications due to their bulk, complexity and cost. Another way of cooling the mechanical degree of freedom is to use the sideband cooling technique introduced in Sec. 4.3. However, to date, this technique also requires precooling to achieve ground states and therefore, is still at the research stage. A technique that has been applied to real-world sensing applications is the displacement measurement [27]. Optomechanical systems are very well suited for displacement sensing due to the large coupling that can be achieved between the optical and mechanical modes. Such measurement is limited by two factors, measurement shot noise and radiation pressure shot noise (RPSN), which set the maximum input drive power for which the sum of these effects is minimal. The precision limit is called the standard quantum limit (SQL) and is typically masked by the thermal noise [60].

High bandwidth accelerometry is one of the areas that could benefit from the high precision displacement measurements that can be performed by optomechanical platforms. A typical accelerometer is based on an accurate displacement measurement of a moving mass under the applied acceleration. This displacement is usually measured using the capacitance between the moving mass and a nearby electrode. Such measurement is limited by the electro-thermal noise from the readout circuitry and can be reduced by employing optical interferometric methods which eliminate the electronic noise and introduce the fundamental thermal-mechanical noise only. This noise leads to a trade-off between the achievable sensitivity and bandwidth. Using displacement measurements in optomechanical systems this noise limit can be achieved.

Another interesting sensing application is magnetometry which has a wide range of uses in biology, medicine, security, defence, condensed matter physics etc. Here, optomechanical systems allow avoiding cryogenic systems while still achieving high magnetic field sensitivity. For this purpose, a magnetostrictive material (Terfenol-D) is placed on a whispering-gallery-mode (WGM) resonator which then contracts and expands under the applied magnetic field. As a result, the resonance frequency of the resonator shifts allowing to infer the magnetic field strength [61].

Atomic force microscopy is also a type of displacement measurement on an optomechanical system. It relies on a nanometer radius tip placed at the end of a cantilever which scans the surface of interest. Contact forces between the tip and the surface deflect the cantilever. This displacement can be measured with high precision using optomechanical readout methods [62].

Finally, the GEO 600 gravitational wave detector measures displacements of mirrors in a Michelson interferometer caused by gravitational waves. These displacements are transduced onto the incident light field at one of the inputs of the Michelson interferometer. Squeezed light has been injected into the empty port present at the other input of the interferometer to further increase the sensitivity of this optomechanical system beyond the SQL [63].

Chapter 5

Experimental setup and equations of motion

5.1 Overview of the experiment

The aim of the experimental work presented in part II of this thesis is to cool a mechanical mode of a microresonator by continuously monitoring the light evanescently coupled to it and evanescently leaving the resonator after the interaction. This conditional state preparation is performed from room temperature using a heterodyne detection scheme. The details of how the measurement is used to learn about the mechanical mode are given in the next chapter. This chapter focuses on the experimental setup, its operational parameter regime and the equations of motion that lead to the power spectral density seen in the heterodyne measurement.

The studied system consists of one acoustic mode and two optical whispering-gallery-modes (WGMs). WGMs take their name after the phenomenon observed under the dome of St. Paul's Cathedral. It was noted that when two people stood at the opposite ends of the dome and faced

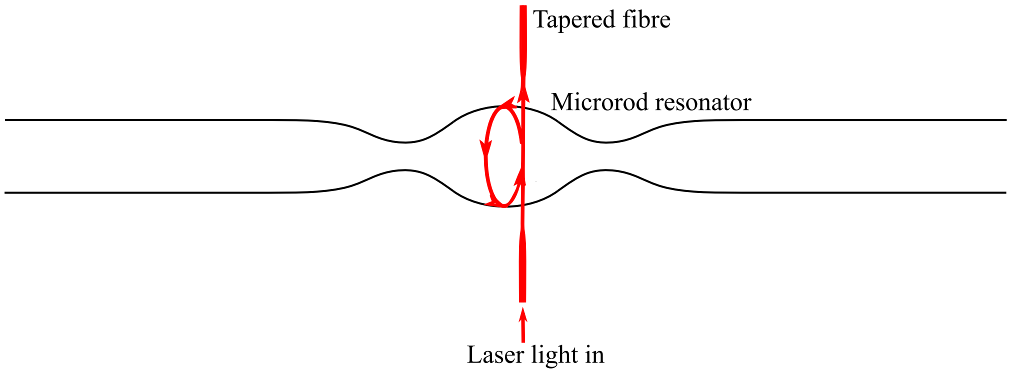

Figure 5.1: Schematic illustration of how laser light (red arrow) is evanescently coupled via a tapered fibre (red) to a whispering-gallery-mode inside a microrod resonator (black). The light is trapped in the bulge region formed on a silica rod using the CO_2-laser lathe machining technique. More information about microrod resonators is given in section 5.3.1.

the dome, they could hear each other's whispers. They could no longer hear the whispers when they faced each other. This phenomenon was first explained by Lord Rayleigh in 1878 [64]. Sound waves bounce off the dome surface with little loss leading to constructive and destructive interference of the waves at different locations of the dome. Later, in the 20th century, this phenomenon was realized for electromagnetic waves inside dielectric spheres and other geometrical structures [49] that light can circulate by means of total internal reflection.

In this experiment, the acoustic wave and the optical WGMs are contained inside a silica microrod resonator [50]. Fig. (5.1) shows the schematic of how laser light evanescently couples to a WGM in such a resonator. The circulating light can then scatter off the mechanical mode by means of Brillouin scattering explained in section 4.4. The two optical WGMs participating in the Brillouin scattering process are separated by approximately the mechanical frequency of $\omega_{\mathrm{m}}/2\pi = 11$ GHz. These are transverse optical modes of the resonator. The lower frequency mode is the pump mode, where the laser light is injected, whereas the higher frequency mode is the anti-Stokes mode, where the scattered pump light scatters into. During

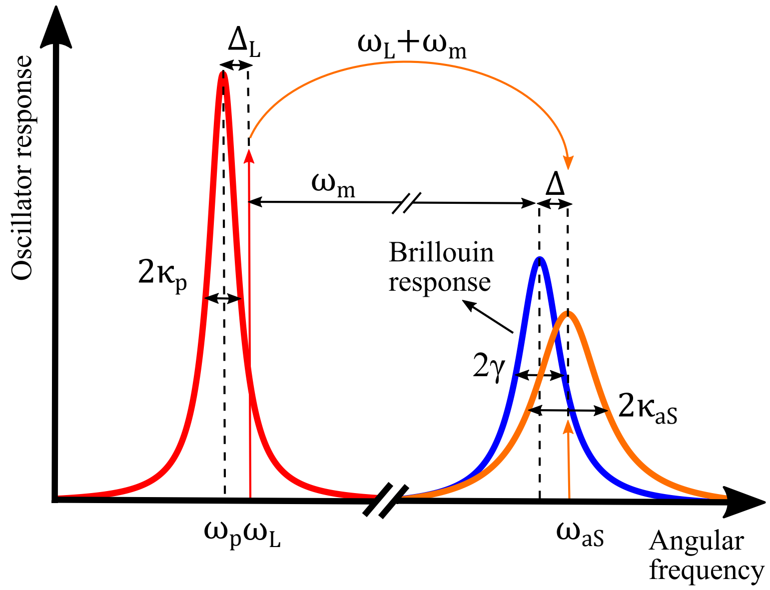

Figure 5.2: BS interaction between the anti-Stokes (orange) and mechanical modes leading to the transfer of phonons from the mechanical to the anti-Stokes mode with the help of an auxiliary pump (red) field. This exchange of quanta is such that the energy and momentum in Eqn. (4.18) and Eqn. (4.19) are conserved within the linewidths of the participating modes.

this scattering process, the pump photons and the acoustic phonons are used to create light of higher frequency in the anti-Stokes mode. This creates a BS interaction between the mechanical and anti-Stokes modes. As a result, the mechanical motion is sideband cooled because the thermal occupation of the mechanical oscillator at room temperature is higher than that of the anti-Stokes mode which is initially in vacuum. The externally driven pump mode acts as an auxiliary mode enhancing the strength of the interaction. Fig. (5.2) shows a pictorial representation of this interaction. It is important to emphasise that Brillouin Stokes scattering is suppressed by the cavity mode structure and therefore the resulting heating effect does not take place. This is because the transverse optical modes of the resonator are irregularly spaced in frequency making it possible to select a mode pair with the desired modal neighbourhood. In the experiment, the laser light, denoted by subscript L, is slightly off-resonance with respect to the pump field. This means that for the same laser power the interaction strength is weakened compared to the on-resonance case. Additionally, there is some frequency mismatch $\Delta/2\pi = \omega_{\mathrm{aS}}/2\pi - \omega_{\mathrm{L}}/2\pi - \omega_{\mathrm{m}}/2\pi$ between the anti-Stokes mode and the Brillouin response spectrum [65]. However, as long as there is an appreciable overlap between them, the Brillouin scattering process will take place.

The BS interaction already leads to cooling of the mechanical motion by means of converting phonons and pump photons into anti-Stokes photons. Monitoring of the anti-Stokes light further enhances our knowledge about the mechanical mode since the two modes are coupled by the BS interaction. This has the effect of reducing the phase space variance of the mechanical state and therefore increases its purity. The experiment has optical non-linearities as well as optomechanical interactions. The non-linearities are discussed in the next section.

5.2 Third-order nonlinear optical materials

All materials, to some extent, have an optical power-dependent refractive index n. A linear dependence of n with power is a third-order nonlinear process and is referred to as the optical Kerr effect. The microrod resonator's medium (fused silica), used for this experiment, is a third-order nonlinear material and therefore exhibits the optical Kerr effect. This results in optical intracavity power dependent frequency shift of the resonances and effectively intracavity power dependent detuning Δ.

The process can be understood by considering the electric polarization field vector $\mathbf{P}$ of a third-order nonlinear material as a function of the electric field vector $\mathbf{E}$,

$$\mathbf{P} = \epsilon_0 \chi^{(1)} \mathbf{E}(\omega) + 3\epsilon_0 \chi^{(3)} \mid \mathbf{E}(\omega) \mid^2 \mathbf{E}(\omega) = \epsilon_0 \chi_{\mathrm{eff}} \mathbf{E}(\omega)\,, \tag{5.1}$$

where ϵ_0 is the vacuum permittivity, $\chi^{(1)}$ and $\chi^{(3)}$ are the first- and third-order susceptibilities respectively [54] and $\chi_{\text{eff}} = \chi^{(1)} + 3\chi^{(3)} \mid \mathbf{E}(\omega) \mid^2$. For simplicity, an isotropic medium is assumed (which applies to fused silica) to suppress the tensor indices associated with $\chi^{(1)}$ and $\chi^{(3)}$. Refractive index n of the material can be defined as

$$n = \sqrt{1 + \chi_{\text{eff}}} = n_0 \sqrt{1 + \frac{3\chi^{(3)}}{n_0^2} \mid \mathbf{E}(\omega) \mid^2}, \tag{5.2}$$

where $n_0 = \sqrt{1 + \chi^{(1)}}$ is the weak field refractive index. Assuming that the nonlinear term in Eqn. (5.1) is much smaller than the linear term and using $\left(1 + x^2\right)^{1/2} \sim (1 + x/2)$ for $x \ll 1$, Eqn. (5.2) can be approximated as

$$n \approx n_0 \left(1 + \frac{3\chi^{(3)}}{2n_0^2} \mid \mathbf{E}(\omega) \mid^2\right). \tag{5.3}$$

In terms of time averaged optical intensity $I = 2n_0\epsilon_0 c \mid \mathbf{E}(\omega) \mid^2$, the above equation reads

$$n = n_0 + \frac{3\chi^{(3)}}{4n_0^2\epsilon_0 c} I = n_0 + n_2 I, \tag{5.4}$$

where $n_2 = 3\chi^{(3)} / \left(4n_0^2\epsilon_0 c\right)$ is the nonlinear refractive index. In general, the change in the refractive index Δn, such that the final refractive index is $n = n_0 + \Delta n$, leads to a frequency shift of

$$\Delta\omega = -\omega \frac{\Delta n}{n}, \tag{5.5}$$

where ω is the original frequency. The above treatment considers refractive index change experienced by the beam of light that caused it. This is the so-called self-Kerr (SK) effect and leads to a frequency shift of a cavity mode by

$$\Delta\omega_{\mathrm{SK}} = -\omega\frac{n_2 I}{n}. \tag{5.6}$$

If two modes, one containing weak intensity and the other one high intensity light, are present in the medium then the frequency of the mode associated with the weak intensity light will also shift due to the presence of the high intensity light mode. This is referred to as the cross-Kerr (XK) effect. In the case of a perfect intensity overlap between the two modes, $\Delta n_{\mathrm{XK}} = 3\chi^{(3)} I / \left(2n_0^2\epsilon_0 c\right) = 2n_2$. The resulting angular frequency shift of the low intensity light mode is

$$\Delta\omega_{\mathrm{XK}} = -\omega\frac{2n_2 I}{n}. \tag{5.7}$$

Lower intensity overlaps between the two modes reduce the factor in front of n_2.

In this experiment (see Fig. (5.2)), the pump mode experiences a self-Kerr effect whereas the anti-Stokes mode, which is initially in vacuum, experiences a cross-Kerr effect due to the high intensity of light in the pump mode. Assuming a perfect overlap between the pump and anti-Stokes modes, the resulting angular frequency separation between the two modes due to the Kerr effect reads

$$\Delta - \Delta_0 = \Delta\omega_{\mathrm{aS}} - \Delta\omega_{\mathrm{p}} = -\frac{\left(2\omega_{\mathrm{aS}} - \omega_{\mathrm{p}}\right) n_2}{n} I_{\mathrm{p}} = -\frac{\left(2\omega_{\mathrm{aS}} - \omega_{\mathrm{p}}\right) n_2}{n A_{\mathrm{eff}}} P_{\mathrm{cav}}. \tag{5.8}$$

Here, Δ_0 is the original separation between the modes, I_{p} is the light intensity in the pump mode, A_{eff} is the effective mode area of the pump mode (which is assumed to be equal to the effective mode area of the anti-Stokes mode) and P_{cav} is the intracavity pump power defined in Eqn. (4.6). Although the intensity overlap between the two modes is not 100% in the experiment, Eqn. (5.8) still shows a linear dependence between Δ and P_{cav}. The slope of this relationship depends on the intensity overlap between the modes.

5.3 Experimental setup

The experiment is performed in polarisation maintaining (PM) fibres and a schematic of the setup is shown in Fig. (5.3). The pump laser of sub-kilohertz linewidth is set to ~ 1550 nm and is evanescently coupled to a silica microrod resonator via a tapered fibre. After identifying a suitable mode pair separated by approximately the mechanical frequency $\omega_{\text{m}}/2\pi$ = 11 GHz, the cavity pump mode is thermally locked to the frequency of the pump laser. The laser light is backscattered off the resonator's acoustic mode into the anti-Stokes mode as explained in Fig. (4.1). The anti-Stokes light is then directed to a heterodyne detector via a circulator and the resulting signal is stored as a time trace. The data can then be analysed to recover the relevant system parameters and to improve our knowledge about the mechanical state.

5.3.1 Microrod resonator

The microrod resonator is a bulge formed on a silica rod using the CO_2–laser lathe machining technique [50]. An example of such resonator is shown in Fig.(5.4a). In this process, a fused-silica rod, machined to a desired diameter, is put on a fast rotating spindle while the CO_2–laser cuts two rings into the rod. The region in between the rings confines the WGMs. The resonator is fabricated in collaboration with Dr. Pascal Del'Haye's group at the National Physical Laboratory in Teddington. The low material and surface losses can give rise to high optical Q-factors exceeding 10^8. See section 4.2 of chapter 4 for definitions of cavity properties. The diameter of

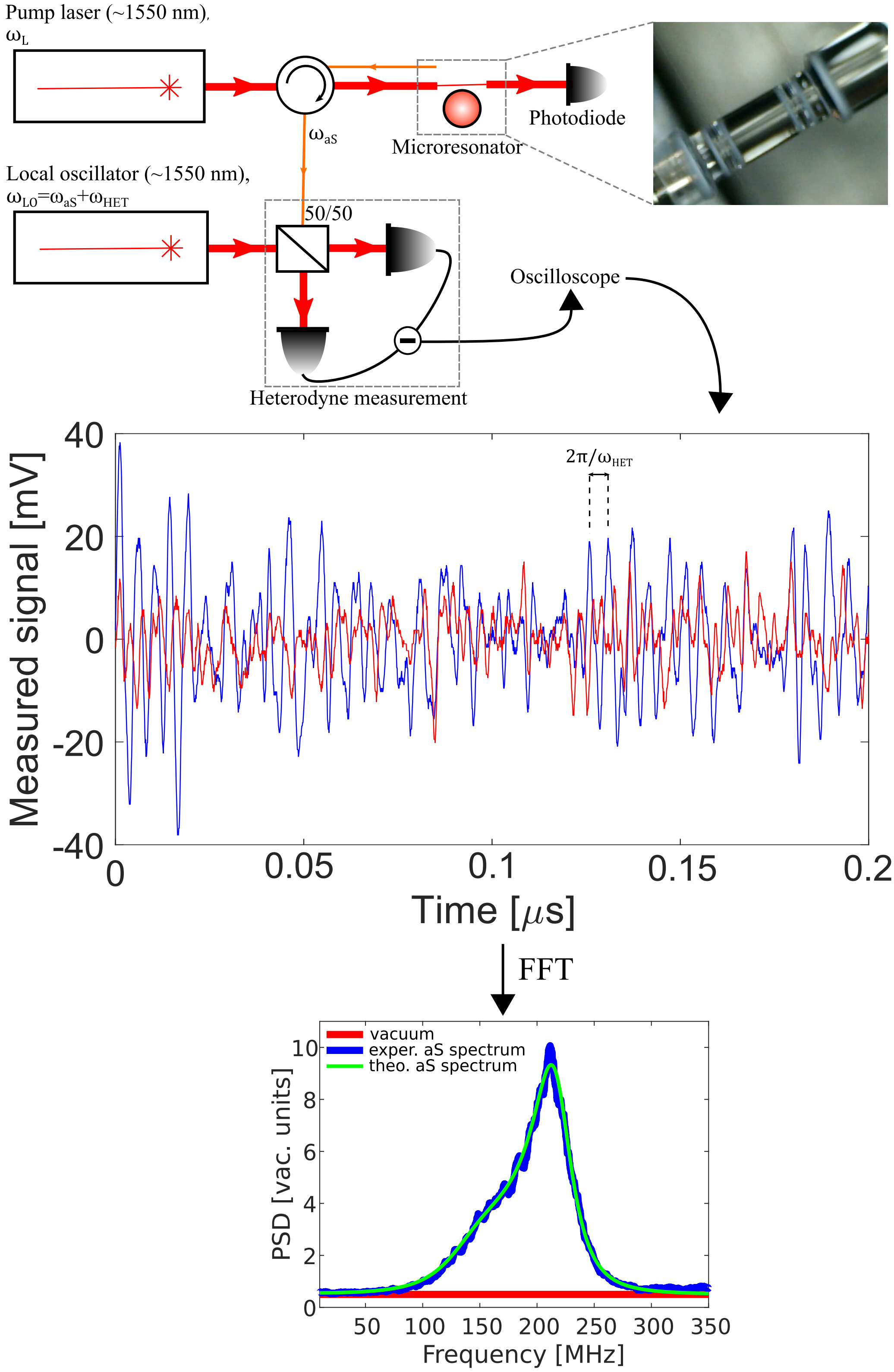

Figure 5.3: Experimental setup: pump light (red) is evanescently coupled into the microrod resonator and backscatters off the resonator's acoustic mode. The resulting anti-Stokes light (orange) is heterodyned and further analysed to reveal information about the mechanical state. The red curve in the time trace represents vacuum signal while the blue curve anti-Stokes signal. Note that PSD refers to power spectral density and FFT to fast Fourier transform.

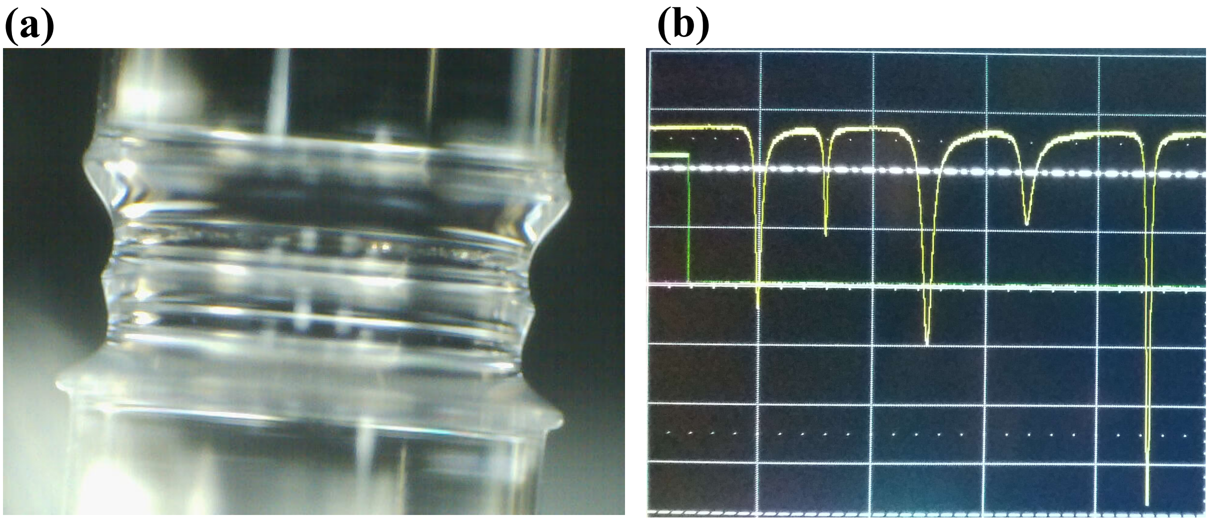

Figure 5.4: **(a)** Microrod resonator of diameter $d = 700\ \mu$m. **(b)** Microrod resonator's optical modes seen as absorption lines on an oscilloscope's time trace. The horizontal time range corresponds to ~ 10 pm wavelength scanning range or equivalently ~ 1.25 GHz frequency scanning range.

the rod used for this experiment is $d = 700\ \mu$m which combined with the refractive index of silica at telecommunication wavelengths, $n = 1.47$, gives the free spectral range (FSR) of $\Delta\omega_{\mathrm{FSR}}/2\pi = 95$ GHz. In wavelength notation, this corresponds to $\Delta\lambda_{\mathrm{FSR}} = 0.76$ nm. Although the pump laser thermal tuning range is 1 nm only, the transverse structure of the resonator allows for many solutions to Maxwell's equations within this range. As explained in section 5.2, the detuning Δ between the pump and anti-Stokes modes varies linearly with the intracavity power due to the self- and cross-Kerr effects inside the silica material.

5.3.2 Searching for resonances

To search for resonances, light resulting from the interference of the pump light that does not couple into the resonator and the pump light that couples out of the resonator is measured in a photodiode as shown in Fig. (5.3). The different resonances can be studied by piezo scanning the laser which relies on applying a ramp voltage followed by an amplifier to the piezo plug. This in turn applies tensile strain to the fibre laser which allows fast wavelength tuning. The resonances can then be observed as transmission dips on an oscilloscope's time trace. See Fig.(5.4b). To pump on the desired mode a thermal lock is applied. The evanescently coupled pump light heats the resonator up which results in red-shifting of the cavity resonance regardless of whether the mode is pumped on the red or blue side with respect to the resonance [66]. A self-stable situation can be reached when approaching the resonance from the blue side. The presence of the optical field heats the cavity and therefore shifts the cavity resonance towards higher wavelengths. This decreases the absorbed power and after some time an equilibrium is reached with the surrounding environment. The pump wavelength can be further increased to tune deeper into the resonance until maximum absorption is reached at which point the resonance is lost. This is the principle of a thermal lock. A self-stable situation can only be established in the blue-detuned case which reduces the available power due to the detuning.

5.3.3 Identifying a suitable mode pair

An appropriate mode pair is identified by looking for the SBS condition explained in section 4.4 of chapter 4. Here, the roles of the pump and the scattering mode are reversed. The higher frequency mode acts as a pump and the lower frequency mode acts as a Stokes mode. If the pump and Stokes modes are separated by the mechanical frequency and the single photon coupling strength g_0 is appreciable then a strong backscattered light can be detected at a frequency $\omega_{\mathrm{m}}/2\pi$ away from the pump light. This can be measured directly on an optical spectrum analyser. A low power threshold SBS is a good indicator for a high g_0 between the modes participating in the Brillouin interaction resulting in a strong anti-Stokes signal.

5.3.4 Heterodyne detection

The heterodyne detector which measures the backscattered anti-Stokes light consists of a strong local oscillator (LO) mixed with the anti-Stokes signal on a 50/50 beam splitter. The LO is derived from an independent laser source to the pump light. It is at a frequency $\omega_{\mathrm{LO}}/2\pi = \omega_{\mathrm{aS}}/2\pi + \omega_{\mathrm{HET}}/2\pi$, where $\omega_{\mathrm{HET}}/2\pi$ is the heterodyne frequency of $\sim$ 150 MHz. The outgoing light from the BS is directed to a balanced detector which measures the photocurrent difference and amplifies it. The balanced detector used for this experiment is the BPD-1 model from Insight Photonic Solutions which has a 3 dB cut-off frequency of 400 MHz and $\sim$ 20 dB clearance between shot noise and electronic noise at the LO power of 5 mW. This is the LO power used for the optomechanics experiments discussed in this part of the thesis. Fig. (5.5a) shows the vacuum and electronic noise frequency spectra for this detector. The vacuum noise has a flat gain spectrum profile within its specified bandwidth which is important for the analysis presented in the next chapter. Fig. (5.5b) shows detector noise variance as a function of LO power. A linear relationship is an indicator of a shot noise limited performance of the detector. At high LO powers, the detector's amplifier saturates which starts happening at $\sim$ 6 mW. The balanced detector has a specified quantum efficiency of $\eta_{\mathrm{BD}} \sim 0.8$ at telecommunication wavelengths limited by the quantum efficiency of its InGaAs photodiodes.

The signal from the balanced detector contains information about the two orthogonal quadratures of the anti-Stokes mode and also of the mechanical mode due to the optomechanical coupling. In an ideal heterodyne detection $\omega_{\mathrm{HET}}/2\pi \to \infty$, however, as long as it is appreciably greater than the mechanical intensity decay rate, which in this case is $2\gamma_{\mathrm{m}}/2\pi \sim 42$ MHz, it is still a very good approximation. The full measured time trace has a length of 100 μs and is sampled at 10 Gsamples/s. A small fraction of such a time trace is shown in Fig. (5.3). The red trace

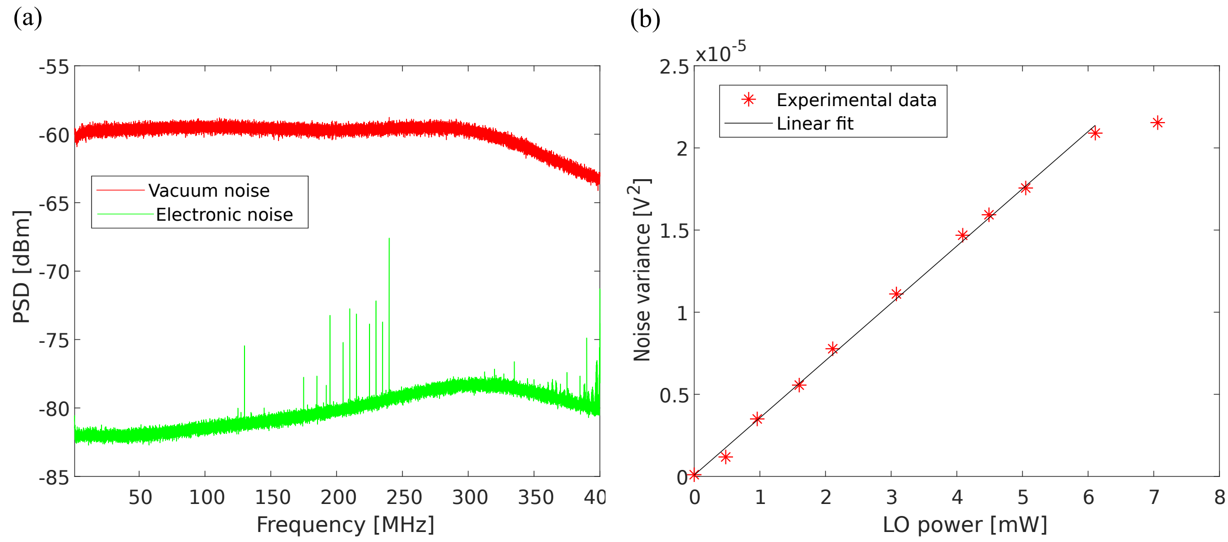

Figure 5.5: **(a)** Frequency spectrum of BPD-1 balanced detector electronic noise (green) and shot noise (red) at 5mW LO power. **(b)** BPD-1 balanced detector noise variance versus LO power.

shows the vacuum signal whereas the blue trace shows the heterodyned anti-Stokes signal. The anti-Stokes signal is visibly modulated by the heterodyne frequency, as indicated on the time trace, and also by the mechanical linewidth.

Fig. (5.6) shows the main parts of the experimental setup.

5.4 System Hamiltonian

The Hamiltonian of the interaction between the pump, anti-Stokes and mechanical modes reads

$$\frac{\hat{H}}{\hbar} = g_0\left(\hat{a}_{\mathrm{p}}\hat{a}_{\mathrm{aS}}^{\dagger}\hat{b} + \hat{a}_{\mathrm{p}}^{\dagger}\hat{a}_{\mathrm{aS}}\hat{b}^{\dagger}\right) + \omega_{\mathrm{p}}\hat{a}_{\mathrm{p}}^{\dagger}\hat{a}_{\mathrm{p}} + \omega_{\mathrm{aS}}\hat{a}_{\mathrm{aS}}^{\dagger}\hat{a}_{\mathrm{aS}} + \omega_{\mathrm{m}}\hat{b}^{\dagger}\hat{b} + \hat{H}_{\mathrm{drive}}, \tag{5.9}$$

where $\hat{H}_{\mathrm{drive}}$ is the input laser drive and is given by $\hat{H}_{\mathrm{drive}} = \Omega^{*}\mathrm{e}^{\mathrm{i}\omega_{\mathrm{L}}t}\hat{a}_{\mathrm{p}} + \Omega\mathrm{e}^{-\mathrm{i}\omega_{\mathrm{L}}t}\hat{a}_{\mathrm{p}}^{\dagger}$ with $\Omega = \sqrt{2\kappa_{\mathrm{p,e}}P_{\mathrm{in}}/\left(\hbar\omega_{\mathrm{p}}\right)}\mathrm{e}^{\mathrm{i}\phi}$. $\kappa_{\mathrm{p,e}}$ denotes the pump mode's external amplitude decay rate, P_{in} is the optical input power to the cavity and ϕ is the initial phase of the input laser. Hamiltonian terms associated with the self- and cross-Kerr effects are ignored since they can be treated as intra-

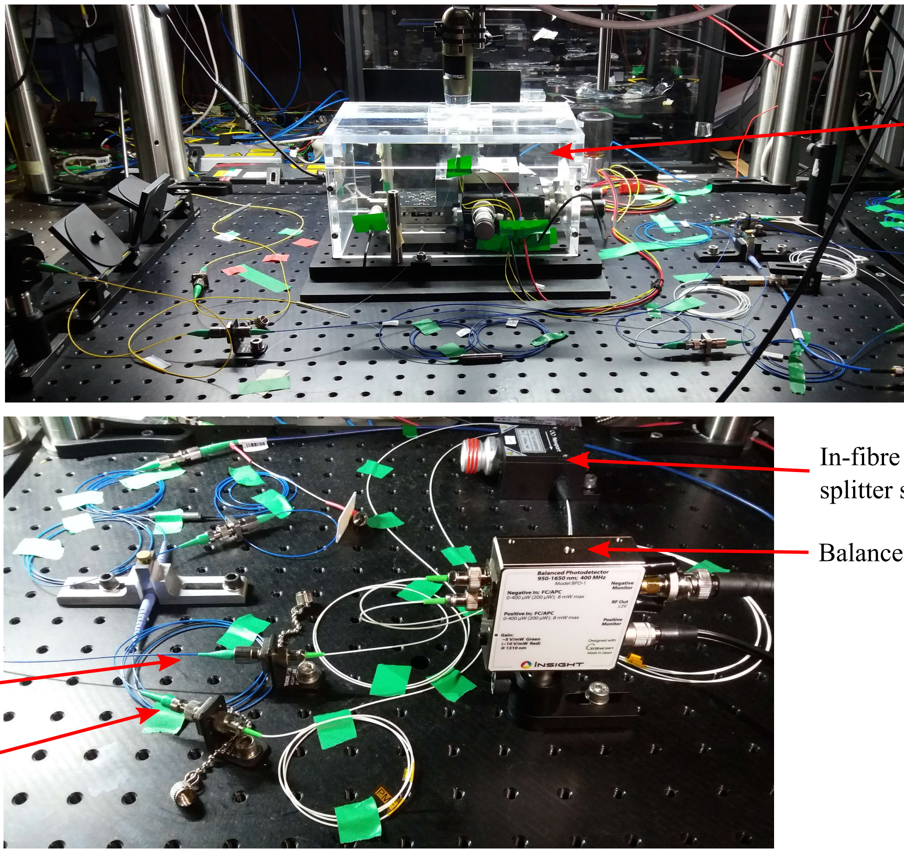

Figure 5.6: Photographs of the main components of the experimental setup.

cavity power dependent detuning Δ, see section 5.2 for details.

The Hamiltonian can be further simplified by working in a suitable rotating frame. Rotating a Hamiltonian in the frame of a general mode operator $\hat{c}$ about frequency ω corresponds to a unitary transformation $\hat{U} = \mathrm{e}^{\mathrm{i}\omega\hat{c}^\dagger\hat{c}t}$. In general, $\hat{U}$ transforms the Hamiltonian in the following way,

$$\hat{H} \rightarrow \hat{U}\hat{H}\hat{U}^\dagger - \mathrm{i}\hat{U}\frac{\partial}{\partial t}\left(\hat{U}^\dagger\right) \tag{5.10}$$

and it is useful to note that $\hat{U}\hat{c}\hat{U}^\dagger = \hat{c}\mathrm{e}^{-\mathrm{i}\omega t}$ and $\hat{U}\frac{\partial}{\partial t}\left(\hat{U}^\dagger\right) = -\mathrm{i}\omega\hat{c}^\dagger\hat{c}$. Therefore rotating the Hamiltonian in Eqn. (5.9) in the frame of the pump mode $\hat{a}_\mathrm{p}$ about the laser frequency ω_L gives

$$\frac{\hat{H}}{\hbar} = g_0\left(\mathrm{e}^{-\mathrm{i}\omega_\mathrm{L}t}\hat{a}_\mathrm{p}\hat{a}_\mathrm{aS}^\dagger\hat{b} + \mathrm{e}^{\mathrm{i}\omega_\mathrm{L}t}\hat{a}_\mathrm{p}^\dagger\hat{a}_\mathrm{aS}\hat{b}^\dagger\right) - \Delta_\mathrm{L}\hat{a}_\mathrm{p}^\dagger\hat{a}_\mathrm{p} + \omega_\mathrm{aS}\hat{a}_\mathrm{aS}^\dagger\hat{a}_\mathrm{aS} + \omega_\mathrm{m}\hat{b}^\dagger\hat{b} + \Omega^*\hat{a}_\mathrm{p} + \Omega\hat{a}_\mathrm{p}^\dagger, \tag{5.11}$$

where $\Delta_{\mathrm{L}} = \omega_{\mathrm{L}} - \omega_{\mathrm{p}}$ is the laser detuning with respect to the pump mode. Further rotating the Hamiltonian in the frame of $\hat{a}_{\mathrm{aS}}$ about ω_{aS} and then in the frame of $\hat{b}$ about $\omega_{\mathrm{aS}} - \omega_{\mathrm{L}}$ gives

$$\frac{\hat{H}}{\hbar} = g_0 \left(\hat{a}_{\mathrm{p}} \hat{a}_{\mathrm{aS}}^{\dagger} \hat{b} + \hat{a}_{\mathrm{p}}^{\dagger} \hat{a}_{\mathrm{aS}} \hat{b}^{\dagger} \right) - \Delta \hat{b}^{\dagger} \hat{b} - \Delta_{\mathrm{L}} \hat{a}_{\mathrm{p}}^{\dagger} \hat{a}_{\mathrm{p}} + \Omega^{*} \hat{a}_{\mathrm{p}} + \Omega \hat{a}_{\mathrm{p}}^{\dagger}, \tag{5.12}$$

where $\Delta = \omega_{\mathrm{aS}} - \omega_{\mathrm{L}} - \omega_{\mathrm{m}}$. Since the pump mode is driven by a strong laser field, it can be treated as a classical field with negligible quantum fluctuations such that

$$\hat{a}_{\mathrm{p}} \to \alpha = |\alpha| \mathrm{e}^{\mathrm{i}\phi}. \tag{5.13}$$

Picking $\phi = 0$ and neglecting the constant terms, the Hamiltonian simplifies to

$$\frac{\hat{H}}{\hbar} = G \left(\hat{a}_{\mathrm{aS}}^{\dagger} \hat{b} + \hat{a}_{\mathrm{aS}} \hat{b}^{\dagger} \right) - \Delta \hat{b}^{\dagger} \hat{b}, \tag{5.14}$$

where $G = |\alpha| g_0$ is the enhanced optomechanical coupling strength.

5.5 Quantum Langevin equations and power spectral density

5.5.1 Fourier transform definitions

The time derivative of a general operator $\hat{C}$ is denoted by $\dot{\hat{C}}$. Operators in the time domain are denoted by $\hat{C}$ whereas operators in the frequency domain by $\tilde{C}$. Fourier transforms for operators and their time derivatives are defined as

$$\hat{C}(t) = \frac{1}{\sqrt{2\pi}} \int_{-\infty}^{+\infty} \tilde{C}(\omega)\, \mathrm{e}^{-\mathrm{i}\omega t} \mathrm{d}\omega \tag{5.15}$$

$$\dot{\hat{C}}(t) = \frac{1}{\sqrt{2\pi}} \int_{-\infty}^{+\infty} -\mathrm{i}\omega\tilde{C}(\omega)\,\mathrm{e}^{-\mathrm{i}\omega t}\mathrm{d}\omega = \frac{-\mathrm{i}}{\sqrt{2\pi}} \int_{-\infty}^{+\infty} \tilde{Z}(\omega)\,\mathrm{e}^{-\mathrm{i}\omega t}\mathrm{d}\omega = -\mathrm{i}\hat{Z}(t)\,, \tag{5.16}$$

where $\tilde{Z}(\omega) = \omega\tilde{C}(\omega)$. In the frequency domain, the operators are

$$\tilde{C}(\omega) = \frac{1}{\sqrt{2\pi}} \int_{-\infty}^{+\infty} \hat{C}(t)\,\mathrm{e}^{\mathrm{i}\omega t}\mathrm{d}t \tag{5.17}$$

$$\dot{\tilde{C}}(\omega) = \frac{1}{\sqrt{2\pi}} \int_{-\infty}^{+\infty} \dot{\hat{C}}(t)\,\mathrm{e}^{\mathrm{i}\omega t}\mathrm{d}t = -\mathrm{i}\tilde{Z}(\omega) = -\mathrm{i}\omega\tilde{C}(\omega)\,. \tag{5.18}$$

Operator $\tilde{C}^{\dagger}(\omega)$ satisfies

$$\tilde{C}^{\dagger}(\omega) = \frac{1}{\sqrt{2\pi}} \int_{-\infty}^{+\infty} \hat{C}^{\dagger}(t)\,\mathrm{e}^{\mathrm{i}\omega t}\mathrm{d}t = \left(\tilde{C}(-\omega)\right)^{\dagger}. \tag{5.19}$$

5.5.2 Quantum Langevin equations of motion

The quantum Langevin equations enable the stochastic evolution of system operators in the Heisenberg picture to be computed [67]. They can be obtained by differentiating an appropriately time-evolved system operator containing the system and environment dynamics under the rules of quantum stochastic calculus. They yield the following time evolution of the anti-Stokes and mechanical modes of the optomechanical system considered in this work,

$$\dot{\hat{a}}_{\mathrm{aS}}(t) = -i\left[\hat{a}_{\mathrm{aS}}(t), \hat{H}\right] - \kappa_{\mathrm{aS}}\hat{a}_{\mathrm{aS}}(t) + \sqrt{2\kappa_{\mathrm{aS,i}}}\hat{a}_{\mathrm{in}}^{(i)}(t) + \sqrt{2\kappa_{\mathrm{sS,e}}}\hat{a}_{\mathrm{in}}^{(\mathrm{e})}(t) \tag{5.20}$$

$$\dot{\hat{b}}(t) = -i\left[\hat{b}(t), \hat{H}\right] - \gamma_{\mathrm{m}}\hat{b}(t) + \sqrt{2\gamma_{\mathrm{m}}}\hat{b}_{\mathrm{in}}(t)\,, \tag{5.21}$$

where $\hat{H}$ is defined in Eqn. (5.14), κ_{aS} is the amplitude decay rate of the anti-Stokes mode and is composed of internal losses $\kappa_{\mathrm{aS,i}}$ and external coupling losses $\kappa_{\mathrm{aS,e}}$ as defined in Eqn. (4.5), and γ_{m} is the mechanical amplitude decay rate. The quantum noise operators $\hat{a}_{\mathrm{in}}^{(\mathrm{i})}$ and $\hat{a}_{\mathrm{in}}^{(\mathrm{e})}$ are associated with the intrinsic and external optical loss channels, and $\hat{b}_{\mathrm{in}}$ noise operator arises from coupling of the mechanical state to the surrounding thermal bath. Substituting for $\hat{H}$ in Eqn. (5.14) gives

$$\dot{\hat{a}}_{\mathrm{aS}}(t) = -\mathrm{i}G\hat{b}(t) - \kappa_{\mathrm{aS}}\hat{a}_{\mathrm{aS}}(t) + \sqrt{2\kappa_{\mathrm{aS,i}}}\hat{a}_{\mathrm{in}}^{(\mathrm{i})}(t) + \sqrt{2\kappa_{\mathrm{aS,e}}}\hat{a}_{\mathrm{in}}^{(\mathrm{e})}(t) \tag{5.22}$$

$$\dot{\hat{b}}(t) = -\mathrm{i}G\hat{a}_{\mathrm{aS}}(t) - \gamma_{\mathrm{m}}\hat{b}(t) + \sqrt{2\gamma_{\mathrm{m}}}\hat{b}_{\mathrm{in}}(t) + \mathrm{i}\Delta\hat{b}(t)\,. \tag{5.23}$$

Fourier transforming Eqn. (5.22) and Eqn. (5.23) according to Eqn. (5.17) and Eqn. (5.18) gives

$$-\mathrm{i}\omega\tilde{a}_{\mathrm{aS}} = -\mathrm{i}G\tilde{b} - \kappa_{\mathrm{aS}}\tilde{a}_{\mathrm{aS}} + \sqrt{2\kappa_{\mathrm{aS,i}}}\tilde{a}_{\mathrm{in}}^{(\mathrm{i})} + \sqrt{2\kappa_{\mathrm{aS,e}}}\tilde{a}_{\mathrm{in}}^{(\mathrm{e})} \tag{5.24}$$

$$-\mathrm{i}\omega\tilde{b} = -\mathrm{i}\left(G\tilde{a}_{\mathrm{aS}} - \Delta\tilde{b}\right) - \gamma_{\mathrm{m}}\tilde{b} + \sqrt{2\gamma_{\mathrm{m}}}\tilde{b}_{\mathrm{in}}. \tag{5.25}$$

Writing this set of simultaneous equations in a matrix form

$$\begin{pmatrix} -\mathrm{i}\omega + \kappa_{\mathrm{aS}} & \mathrm{i}G \\ \mathrm{i}G & -\mathrm{i}(\omega+\Delta) + \gamma_{\mathrm{m}} \end{pmatrix} \begin{pmatrix} \tilde{a}_{\mathrm{aS}} \\ \tilde{b} \end{pmatrix} = \begin{pmatrix} \sqrt{2\kappa_{\mathrm{aS,i}}}\tilde{a}_{\mathrm{in}}^{(\mathrm{i})} + \sqrt{2\kappa_{\mathrm{aS,e}}}\tilde{a}_{\mathrm{in}}^{(\mathrm{e})} \\ \sqrt{2\gamma_{\mathrm{m}}}\tilde{b}_{\mathrm{in}} \end{pmatrix} \tag{5.26}$$

and solving for $\tilde{a}_{\mathrm{aS}}$ and $\tilde{b}$ yields

$$\begin{pmatrix} \tilde{a}_{\mathrm{aS}} \\ \tilde{b} \end{pmatrix} = D \begin{pmatrix} -\mathrm{i}(\omega+\Delta) + \gamma_{\mathrm{m}} & -\mathrm{i}G \\ -\mathrm{i}G & -\mathrm{i}\omega + \kappa_{\mathrm{aS}} \end{pmatrix} \begin{pmatrix} \sqrt{2\kappa_{\mathrm{aS,i}}}\tilde{a}_{\mathrm{in}}^{(\mathrm{i})} + \sqrt{2\kappa_{\mathrm{aS,e}}}\tilde{a}_{\mathrm{in}}^{(\mathrm{e})} \\ \sqrt{2\gamma_{\mathrm{m}}}\tilde{b}_{\mathrm{in}} \end{pmatrix}, \tag{5.27}$$

where

$$D(\omega) = \frac{1}{(-\mathrm{i}\omega + \kappa_{\mathrm{aS}})\left(-\mathrm{i}(\omega+\Delta) + \gamma_{\mathrm{m}}\right) + G^2}. \tag{5.28}$$

Eqn. (5.27) describes the anti-Stokes and mechanical fields in the frequency domain inside the cavity. The optical field that comes out of the cavity $\tilde{a}_{\mathrm{out}}$ can be described using the cavity input-output theory [67],

$$\tilde{a}_{\mathrm{out}} = \tilde{a}_{\mathrm{in}}^{(\mathrm{e})} - \sqrt{2\kappa_{\mathrm{aS,e}}}\tilde{a}_{\mathrm{aS}}. \tag{5.29}$$

The light field that comes out of the cavity also experiences detection losses. These losses can be encapsulated in the detection efficiency parameter denoted by η_{det} and defined by the ratio of intensity of light after enduring the losses and intensity of light before encountering the loss channel. This extra loss channel can be modelled as a beam splitter of transmissivity $\sqrt{\eta_{\mathrm{det}}}$ and reflectivity $\sqrt{1-\eta_{\mathrm{det}}}$ with $\tilde{a}_{\mathrm{out}}$ and vacuum field $\tilde{a}_{\mathrm{in}}^{(\mathrm{bs})}$ at the inputs of the beam splitter. Therefore, the detected optical field operator in frequency domain is

$$\tilde{a} = \sqrt{\eta_{\mathrm{det}}}\left(\tilde{a}_{\mathrm{in}}^{(\mathrm{e})} - \sqrt{2\kappa_{\mathrm{aS,e}}}\tilde{a}_{\mathrm{aS}}\right) + \sqrt{1-\eta_{\mathrm{det}}}\tilde{a}_{\mathrm{in}}^{(\mathrm{bs})}. \tag{5.30}$$

Substituting for $\tilde{a}_{\mathrm{aS}}$ from Eqn. (5.27) into Eqn. (5.30) and defining coupling efficiency as $\eta_{\mathrm{cpl}} = \kappa_{\mathrm{aS,e}}/\kappa_{\mathrm{aS}}$ gives

$$\begin{aligned}
\tilde{a} =& 2\mathrm{i}G\sqrt{\eta_{\mathrm{det}}\eta_{\mathrm{cpl}}}\sqrt{\kappa_{\mathrm{aS}}\gamma_{\mathrm{m}}}D\tilde{b}_{\mathrm{in}} \\
&- 2\sqrt{\eta_{\mathrm{det}}\eta_{\mathrm{cpl}}}\sqrt{\kappa_{\mathrm{aS}}\kappa_{\mathrm{aS,i}}}D\left(-\mathrm{i}\left(\omega+\Delta\right)+\gamma_{\mathrm{m}}\right)\tilde{a}_{\mathrm{in}}^{(\mathrm{i})} \\
&+ \sqrt{\eta_{\mathrm{det}}}\left(1-2\eta_{\mathrm{cpl}}\kappa_{\mathrm{aS}}D\left(-\mathrm{i}\left(\omega+\Delta\right)+\gamma_{\mathrm{m}}\right)\right)\tilde{a}_{\mathrm{in}}^{(\mathrm{e})} \\
&+ \sqrt{1-\eta_{\mathrm{det}}}\tilde{a}_{\mathrm{in}}^{(\mathrm{bs})} \\
=& A_1(\omega)\,\tilde{b}_{\mathrm{in}} + A_2(\omega)\,\tilde{a}_{\mathrm{in}}^{(\mathrm{i})} + A_3(\omega)\,\tilde{a}_{\mathrm{in}}^{(\mathrm{e})} + A_4(\omega)\,\tilde{a}_{\mathrm{in}}^{(\mathrm{bs})},
\end{aligned} \tag{5.31}$$

where in the last row the coefficients in front of the noise operators are abbreviated into the $A(\omega)$ terms.

5.5.3 Power spectrum of detected light

The out-coupled anti-Stokes light is directed to a heterodyne detector which measures two orthogonal quadratures of light. More precisely, it measures quadratures rotating at the heterodyne frequency $\omega_{\mathrm{HET}}/2\pi$ given by

$$\hat{X}_{\mathrm{HET}}(t) = \frac{1}{\sqrt{2}}\left(\hat{a}^{\dagger}(t)\,\mathrm{e}^{\mathrm{i}\omega_{\mathrm{HET}}t} + \hat{a}(t)\,\mathrm{e}^{-\mathrm{i}\omega_{\mathrm{HET}}t}\right). \tag{5.32}$$

The power spectral density (PSD) of an operator is defined as the Fourier transform of its autocorrelation function [68]. For the operator $\hat{X}_{\mathrm{HET}}$, this gives a PSD $S_{X_{\mathrm{HET}}X_{\mathrm{HET}}}$ of

$$S_{X_{\mathrm{HET}}X_{\mathrm{HET}}}(\omega) = \int_{-\infty}^{+\infty} \mathrm{e}^{\mathrm{i}\omega\tau}\left\langle \hat{X}^{\dagger}_{\mathrm{HET}}(t+\tau)\,\hat{X}_{\mathrm{HET}}(t)\right\rangle \mathrm{d}\tau. \tag{5.33}$$

Equivalently, it can be written as

$$S_{X_{\mathrm{HET}}X_{\mathrm{HET}}}(\omega) = \int_{-\infty}^{+\infty} \left\langle \tilde{X}^{\dagger}_{\mathrm{HET}}(\omega)\,\tilde{X}_{\mathrm{HET}}\left(\omega'\right)\right\rangle \mathrm{d}\omega', \tag{5.34}$$

where $\tilde{X}_{\mathrm{HET}}(\omega) = \tilde{X}^{\dagger}_{\mathrm{HET}}(\omega)$ is the Fourier transform of $\hat{X}_{\mathrm{HET}}(t)$ defined in Eqn. (5.17) given by

$$\tilde{X}_{\mathrm{HET}}(\omega) = \frac{1}{\sqrt{2}}\left(\tilde{a}^{\dagger}(\omega_{+}) + \tilde{a}(\omega_{-})\right). \tag{5.35}$$

Here, $\omega_{+} = \omega + \omega_{\mathrm{HET}}$ and $\omega_{-} = \omega - \omega_{\mathrm{HET}}$. The PSD for the rotating quadrature can therefore be written as

$$S_{X_{\mathrm{HET}}X_{\mathrm{HET}}}(\omega) = \frac{1}{2}\int_{-\infty}^{+\infty} \left\langle \tilde{a}^{\dagger}(\omega_{+})\,\tilde{a}\left(\omega'_{-}\right)\right\rangle + \left\langle \tilde{a}(\omega_{-})\,\tilde{a}^{\dagger}\left(\omega'_{+}\right)\right\rangle \mathrm{d}\omega', \tag{5.36}$$

where terms $\langle \tilde{a}\tilde{a} \rangle$ and $\langle \tilde{a}^{\dagger}\tilde{a}^{\dagger} \rangle$ do not contribute towards the PSD. Correlation functions of the input noise satisfy [68]

$$\begin{aligned}\left\langle \tilde{b}_{\text{in}}^{\dagger}(\omega)\,\tilde{b}_{\text{in}}(\omega')\right\rangle &= \bar{n}_{\text{b}}\delta\left(\omega+\omega'\right)\\ \left\langle \tilde{b}_{\text{in}}(\omega)\,\tilde{b}_{\text{in}}^{\dagger}(\omega')\right\rangle &= (\bar{n}_{\text{b}}+1)\,\delta\left(\omega+\omega'\right)\end{aligned} \tag{5.37}$$

and

$$\begin{aligned}\left\langle \tilde{a}_{\text{in}}^{\dagger}(\omega)\,\tilde{a}_{\text{in}}(\omega')\right\rangle &= 0\\ \left\langle \tilde{a}_{\text{in}}(\omega)\,\tilde{a}_{\text{in}}^{\dagger}(\omega')\right\rangle &= \delta\left(\omega+\omega'\right),\end{aligned} \tag{5.38}$$

where $\bar{n}_{\text{b}}$ is the mechanical thermal bath occupation. The resulting PSD is

$$S_{X_{\text{HET}}X_{\text{HET}}}(\omega) = \frac{1}{2}\left(|\,A_1(-\omega_+)\,|^2\,\bar{n}_{\text{b}} + |\,A_1(\omega_-)\,|^2\,\bar{n}_b + 1\right) \tag{5.39}$$

Substituting for A_1 using Eqn. (5.31) gives

$$S_{X_{\text{HET}}X_{\text{HET}}}(\omega) = \frac{1}{2} + 2\eta_{\text{det}}\eta_{\text{cpl}}\kappa_{\text{aS}}\gamma_{\text{m}}G^2\bar{n}_{\text{b}}\left(|\,D(-\omega_+)\,|^2 + |\,D(\omega_-)\,|^2\right) \tag{5.40}$$

and substituting for D using Eqn. (5.28) we have

$$\begin{aligned}S_{X_{\text{HET}}X_{\text{HET}}}(\omega) = \frac{1}{2} &+ 2\eta_{\text{det}}\eta_{\text{cpl}}\kappa_{\text{aS}}\gamma_{\text{m}}G^2\bar{n}_{\text{b}}\times\\ &\times\left(\frac{1}{\left(G^2-\omega_+(\omega_+-\Delta)+\kappa_{\text{aS}}\gamma_{\text{m}}\right)^2+\left(\omega_+\left(\gamma_{\text{m}}+\kappa_{aS}\right)-\Delta\kappa_{\text{aS}}\right)^2}\right.\\ &+\left.\frac{1}{\left(G^2-\omega_-(\omega_-+\Delta)+\kappa_{\text{aS}}\gamma_{\text{m}}\right)^2+\left(\omega_-\left(\gamma_{\text{m}}+\kappa_{\text{aS}}\right)+\Delta\kappa_{\text{aS}}\right)^2}\right).\end{aligned} \tag{5.41}$$

When $\Delta = 0$, the above heterodyne power spectrum is symmetric. When $\Delta \neq 0$, the Δ terms bring linear and third-order terms in ω_+ and ω_- in the denominators of Eqn. (5.41) resulting in

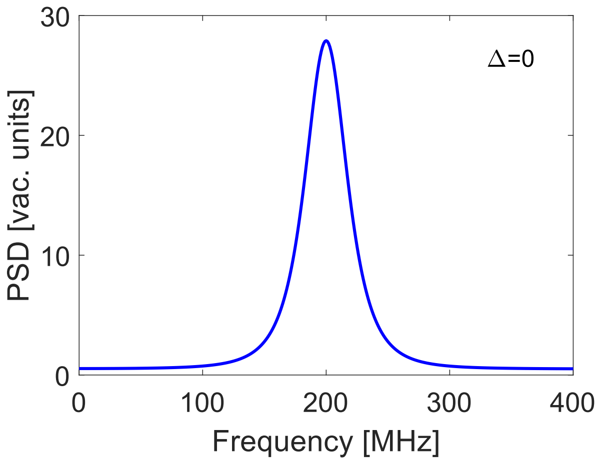

Figure 5.7: Analytical heterodyne power spectra obtained using Eqn. (5.41) for detunings $\Delta/2\pi = 0$ (left) and $\Delta/2\pi = -70$ MHz (right). Parameters: $G/2\pi = 9.6$ MHz, $\kappa_{\mathrm{aS}}/2\pi = 45.5$ MHz, $\gamma_{\mathrm{m}}/2\pi = 21$ MHz, $\eta_{\mathrm{cpl}} = 0.88$, $\eta_{\mathrm{det}} = 0.35$, $\bar{n}_{\mathrm{b}} = 555$ and $\omega_{\mathrm{HET}}/2\pi = 200$ MHz (left), and $\omega_{\mathrm{HET}}/2\pi = 140$ MHz (right).

the antisymmetric spectrum. The two instances of $\Delta = 0$ and $\Delta \neq 0$ are shown in Fig. (5.7).

5.6 Parameter regime in which the experiment operates

The thermal occupation of the mechanical bath $\bar{n}_{\mathrm{b}}$ in the high temperature limit can be determined by

$$\bar{n}_{\mathrm{b}} \sim \frac{k_{\mathrm{B}} T}{\hbar \omega_{\mathrm{m}}}, \tag{5.42}$$

where T is the bath temperature and k_{B} is the Boltzmann constant. The experiment is operated at room temperature of $T \sim 293$ K and the Brillouin signal has a frequency of $\omega_{\mathrm{m}}/2\pi \sim 11$ GHz which gives $\bar{n}_{\mathrm{b}} = 555$. The high mechanical frequency puts the system in the resolved sideband regime, where $\omega_{\mathrm{m}} >> \kappa$.

The detection efficiency η_{det} can be divided into two components: heterodyne efficiency η_{HET} and transmitted power efficiency η_{trans} between the anti-Stokes output of the microresonator and the input of the heterodyne detector. $\eta_{\mathrm{HET}} \sim 0.77$ and is mostly limited by the efficiency of the balanced detector ($\eta_{\mathrm{BD}} \sim 0.8$). The remaining contribution comes from the 50/50 beam splitter. $\eta_{\mathrm{trans}} \sim 0.8\sqrt{\eta_{\mathrm{TF}}}$ depends mainly on the circulator efficiency and the tapered fibre efficiency η_{TF}. Therefore, $\eta_{\mathrm{det}} = \eta_{\mathrm{HET}}\eta_{\mathrm{trans}} \sim 0.62\sqrt{\eta_{\mathrm{TF}}}$. All the efficiencies are determined by measuring the input and output intensity of light passing through the relevant optical components except for the efficiency of the balanced detector which is taken from the manufacturer's specification.

As explained in section 5.2, the self- and cross-Kerr effects give rise to a linear dependence between the intracavity power and detuning Δ. The slope of this relationship depends on the intensity overlap between the pump and anti-Stokes modes and therefore depends on the choice of the optical modes.

The mechanical amplitude decay rate for the silica microrod resonator is measured to be $\gamma_{\mathrm{m}}/2\pi \sim 21$ MHz by fitting the heterodyne power spectra to the model in Eqn. (5.41) [3].

The taper-resonator system can operate in three optical coupling regimes: under-, critically- and over-coupled, by bringing the tapered fibre appropriately close to the surface of the microrod resonator. Changing the distance between the tapered fibre and the resonator alters the amount of light evanescently coupled into the resonator. It therefore changes the decay rate due to the external coupling losses κ_{e}. The three coupling regimes can be summarised as follows,

$$\begin{aligned} \text{under-coupled:} \quad & \kappa_{\mathrm{e}} < \kappa_{\mathrm{i}} \\ \text{critically-coupled:} \quad & \kappa_{\mathrm{e}} = \kappa_{\mathrm{i}} \\ \text{over-coupled:} \quad & \kappa_{\mathrm{e}} > \kappa_{\mathrm{i}}. \end{aligned} \tag{5.43}$$

Scanning the resonances and changing the amount of light that is coupled into the resonator are the only degrees of freedom accessible by the experimentalist. They allow varying $\kappa_{\mathrm{aS,e}}$, but also affect the amount of light coupled into the pump mode and hence influence G. The intracavity power in the pump mode is maximised when $\kappa_{\mathrm{p,e}} = \sqrt{\kappa_{\mathrm{p,i}}^2 + \Delta_{\mathrm{L}}^2}$, so when the light is close to critically-coupled to the pump mode if the laser detuning is small. This can be derived by maximising Eqn. (4.6) with respect to $\kappa_{\mathrm{p,e}}$. Note that subscript p denotes the pump mode.

The total amplitude decay rate of the optical modes $2\kappa/2\pi$ is identified by measuring the half-width at half-maximum of the transmission dips recorded on an oscilloscope's time trace. These transmission dips are formed due to the light that results from the interference of the laser light that does not couple into the resonator and light that couples out of the resonator. The measured width can be converted from the time units to the frequency units by writing sidebands at a known modulation frequency. The intrinsic and external optical loss contributions, $2\kappa_{\mathrm{i}}/2\pi$ and $2\kappa_{\mathrm{e}}/2\pi$ respectively, can be determined by recording the cavity transmission on resonance T_0. T_0 relates to κ_{e} and κ via

$$T_0 = \left(1 - \frac{2\kappa_{\mathrm{e}}}{\kappa}\right)^2 \tag{5.44}$$

and κ_{i} can be identified via $\kappa = \kappa_{\mathrm{i}} + \kappa_{\mathrm{e}}$.

The optomechanical coupling strength G is determined by fitting the experimental power spectrum of the heterodyned light to the theoretical model in Eqn. (5.41). To verify the extracted parameters, a sequence of time-domain data is taken at varying intracavity power P_{cav} defined in Eqn. (4.6). Since $G = |\,\alpha\,|\, g_0$, a square root scaling is expected in a plot of G as a function of P_{cav} (see Fig. (5.9)).

5.6.1 Strong coupling

The high Q-factors of the optical resonator modes allow achieving the parameter regime where strong coupling between the optical and mechanical modes can be observed. This is reported in [3]. When the two modes are uncoupled they oscillate independently at frequencies ω_{aS} and ω_{m}. In an appropriate rotating frame picture, the system can be described by two eigenstates having the same eigenfrequencies, but different damping rates κ_{aS} and γ_{m} for the optical and mechanical modes respectively. When the modes are strongly coupled, the eigenstates in this picture are not degenerate in eigenfrequencies anymore and energy splitting for $\Delta = 0$ can be observed. This energy splitting is a signature of strong coupling and is referred to as normal mode splitting. The two eigenstates have now damping rates composed of a mixture of κ_{aS} and γ_{m} and more specifically, for $\Delta = 0$, they have a common damping rate of $\left(\kappa_{\mathrm{aS}} + \gamma_{\mathrm{m}}\right)/2$. The strongly coupled modes can be viewed as a single system with hybrid optomechanical modes oscillating at frequencies determined by the coupling strength G. The strong coupling condition is $G > \left(\kappa_{\mathrm{aS}} + \gamma_{\mathrm{m}}\right)/2$. To achieve this requirement, κ_{aS} has to be as small as possible, but at the same time the pump mode has to have sufficient external coupling to allow high G.

This was one of the main parts of my work with the manuscript under review [3]. The details will be given in Georg Enzian's thesis as it is a group policy to avoid repetition in theses.

5.6.2 Parameter regime for cooling of the mechanical mode

When cooling the motion of a mechanical mode, the optical anti-Stokes mode serves as a damping channel for the acoustic phonons. It is therefore beneficial to work in the over-coupled regime for the anti-Stokes mode. At the same time, it is important to operate at a high optomechanical coupling strength G which can be obtained when laser detuning is as small as possible

Parameter	Parameter abbreviation	Value	Units
Enhanced optomechanical coupling strength	$G/2\pi$	between 2.3 and 9.6	MHz
Detuning: $\omega_{\mathrm{aS}}/2\pi - \omega_{\mathrm{L}}/2\pi - \omega_{\mathrm{m}}/2\pi$	$\Delta/2\pi$	between −74 and 33	MHz
Heterodyne frequency: $\omega_{\mathrm{LO}}/2\pi - \omega_{\mathrm{aS}}/2\pi$	$\omega_{\mathrm{HET}}/2\pi$	between 140 and 200	MHz
Mechanical amplitude decay rate	$\gamma_{\mathrm{m}}/2\pi$	21	MHz
Total optical amplitude decay rate	$\kappa_{\mathrm{aS}}/2\pi$	45.5	MHz
Detection efficiency	η_{det}	0.35	-
Coupling efficiency	η_{cpl}	0.88	-
Total efficiency: $\eta_{\mathrm{det}}\eta_{\mathrm{cpl}}$	η	0.31	-
Mechanical thermal occupation	$\bar{n}_{\mathrm{b}}$	555	-
Total measurement acquisition time	t_{acq}	100	μs
Oscilloscope sampling rate	SR	10×10^9	SPS
Balanced detector bandwidth	BW	350	MHz

Table 5.1: System parameters for the mechanical state cooling experiment. SPS denotes samples per second.

and the pump mode is close to critically-coupled. Table (5.1) shows a summary of the relevant parameters used for the measurement enhanced cooling of the mechanical mode presented in the next chapter. Note that a set of time-domain data is taken for different optomechanical coupling strengths and therefore different detunings. Fig. (5.8) shows the expected linear relationship between the detuning and intracavity power for the chosen pump and anti-Stokes modes. Fig. (5.9) shows the anticipated square root scaling of the optomechanical coupling strength with the intracavity power.

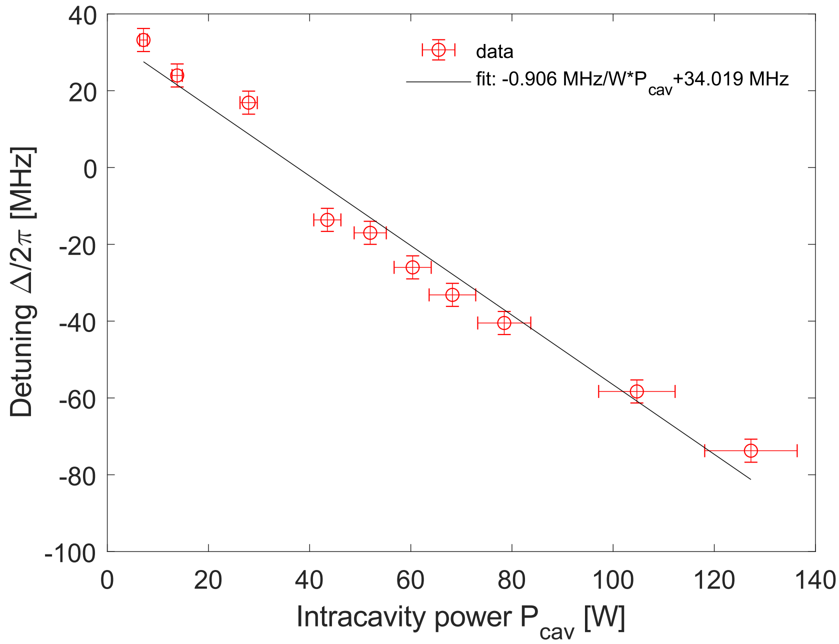

Figure 5.8: Detuning versus intracavity power curve for the selected optical mode pair. The linear relationship is expected due to the self- and cross- Kerr effects experienced by the pump and anti-Stokes modes respectively.

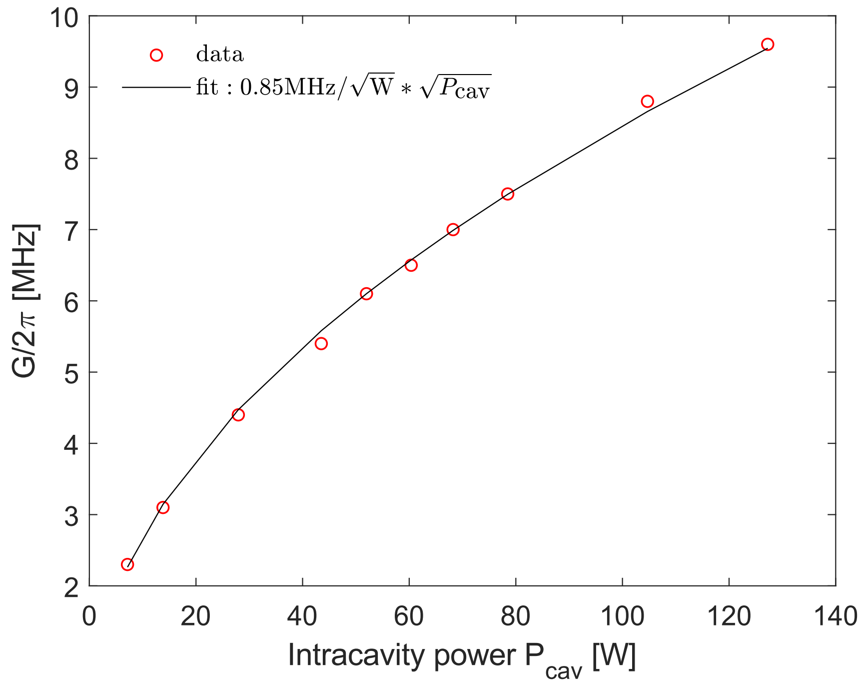

Figure 5.9: Enhanced optomechanical coupling strength versus intracavity power for the selected optical mode pair. $G = \mid \alpha \mid g_0$ is expected to have a square root scaling with P_{cav} as shown in the data.

Chapter 6

Measurement enhanced cooling

6.1 Current cooling techniques and state of the art

Cooling of mechanical motion is an important goal in many aspects of optomechanics. Its importance for fundamental science as well as practical applications, for instance metrology, makes such studies worthwhile pursuing. Gravitational wave sensing is one of the areas that started this field direction. Gravitational wave detectors consist of test masses that are driven into motion by the passing gravitational waves. The displacement of the test masses can be accurately measured using optical interferometry. Ideally, the interferometer arm lengths should be a quarter of the gravitational wave wavelength which corresponds to arm lengths of 75 km [16]. To avoid such long distances, Fabry-Perot cavities are used to increase the effective distance travelled by light inside the interferometer. The system dynamics therefore comprises mechanical motion of the test masses and the dynamics generated due to the presence of light inside the optical cavity. The behaviour of this type of optomechanical system and the associated mechanical motion cooling limits were studied by Braginskiǐ and colleagues in 1960s and 1970s.

Their studies first explored sideband cooling for optomechanical systems [21, 22] and the importance of radiation pressure shot noise in displacement measurements [25, 69, 70]. Enhanced cooling and attaining the mechanical ground state in different optomechanical platforms has since remained of major interest.

6.1.1 Sideband cooling

Laser driving a cavity optical mode on resonance ($\omega_L = \omega_{cav}$) leads to formation of optical sidebands as the mechanical motion modulates the optical field. This interaction leads to creation of photons at frequencies ($\omega_L - \omega_m$) and ($\omega_L + \omega_m$) when phonons are created and annihilated from the mechanical mode respectively. The low frequency sideband is referred to as the Stokes light whereas the high frequency sideband as the anti-Stokes light. Sideband cooling relies on red-detuning the laser light with respect to the cavity optical mode by an amount ω_m such that the Stokes light is suppressed by the cavity response. As a result, anti-Stokes scattering dominates and cooling of the mechanical mode can be achieved. Quantitative description of the heating and cooling processes are given in sections 4.4 and 4.3 for the radiation pressure and electrostrictive couplings respectively.

In the case of radiation pressure coupling, there is typically only one optical mode present. Although red-detuning the laser light with respect to this optical mode suppresses the Stokes heating process, there is a limit to how much mechanical motion can be cooled. This limit is called the quantum backaction limit and is caused by the quantum fluctuations of the radiation pressure force which lead to asymmetry in Stokes and anti-Stokes transition rates [52]. In addition to the cavity response, the former is proportional to $(\bar{n}+1)$ and the latter to $\bar{n}$, where $\bar{n}$ is the phonon occupation number in the mechanical mode. When $\bar{n}$ is appreciably larger than 1 the asymmetry in the heating and cooling transition rates has negligible effect. However, as the phonon number approaches the mechanical ground state occupation ($\bar{n} < 1$), the addition of 1 in the pre-factor for Stokes transition rates starts becoming important. It leads to the balance between the heating and cooling transition rates at a non-zero phonon number even when there is no coupling to the mechanical thermal bath ($\gamma_\mathrm{m} = 0$). In the resolved sideband regime ($\omega_\mathrm{m} \gg \kappa$), this back action occupation number is given by $\bar{n}_\mathrm{min} = (\kappa/2\omega_\mathrm{m})^2$ [26]. Sideband cooling allows optomechanical systems with appropriately low mechanical thermal bath occupation number reaching the mechanical ground state [37, 38] and quantum backaction limit [40]. All these experiments had to be carried out in cryogenic environments to achieve $\bar{n} < 1$. Earlier works had been conducted at room temperatures and allowed reducing the mechanical occupation number by a factor better than 30 using sideband cooling [34, 35].

Anti-Stokes Brillouin cooling has not been extensively explored in the field of optomechanics. Electrostrictive property of the resonator medium is responsible for the optomechanical coupling necessary for the scattering to occur. Platforms where this process is present, for instance microrod and microsphere resonators, typically allow selecting discrete optical modes. Suppression of the Stokes light is possible by identifying two discrete optical resonances separated by the mechanical frequency. Cooling of a mechanical mode inside a silica microsphere by forward Brillouin anti-Stokes scattering was reported in [39].

6.1.2 Feedback cooling

Feedback cooling in optomechanical systems relies on continuous monitoring of the optical field to gain information about the position of the mechanical oscillator. With this knowledge, it is possible to obtain an estimate of the oscillator's velocity and to apply an appropriate feedback force to oppose the mechanical motion [71]. This technique was first proposed in [42] and experimentally realised in [72]. It requires optimal estimates of quadrature expectation values which can be achieved via the stochastic master equation model of the system. Given the optimal quadrature estimates, a feedback force can be applied to the mechanical oscillator to displace it back to the origin.

Feedback cooling has been successfully implemented in different optomechanical platforms. Studies in [43, 73, 74] achieved cooling of mechanical motion to effective temperatures in the millikelvin regime and [75] used this technique for high precision force sensing. Feedback cooling was applied to enhance sideband cooling techniques [76, 45] and to modify the in-loop cooling field to observe normal mode splitting due to the decreased optical cavity linewidth [77]. More recently, Rossi et al. [46] reported feedback cooling of a nanomechanical membrane resonator from a cryogenic temperature of ~ 10 K down to its quantum ground state.

Studies in this area use phase sensitive detection schemes, such as homodyning, to measure the phase of the probe beam to estimate the mechanical position. The optimal detection strategy depends on the interaction Hamiltonian $\hat{H}_{\text{int}}$ between the optical (subscript L) and mechanical (subscript m) fields. In the case of radiation pressure coupling with the driving field on-resonance with the optical cavity, $\hat{H}_{\text{int}} \propto \hat{X}_{\text{L}}\hat{X}_{\text{m}}$ as can be seen from Eqn. (4.16). In such interactions measuring a single quadrature of light (phase), for instance via homodyning, captures all the information about the mechanical mode. This can be understood by considering the Heisenberg equation of motion between the optical quadratures $\hat{X}_{\text{L}}$ and $\hat{P}_{\text{L}}$, and $\hat{H}_{\text{int}}$. The time evolution of $\hat{P}_{\text{L}}$ is coupled to $\hat{X}_{\text{m}}$ while $\hat{X}_{\text{L}}$ remains unaffected. The beam-splitter interaction, relevant for sideband cooling, leads to a different interaction Hamiltonian $\hat{H}_{\text{int}} \propto \hat{X}_{\text{L}}^{\dagger}\hat{X}_{\text{m}} + \hat{P}_{\text{L}}^{\dagger}\hat{P}_{\text{m}}$. It couples $\hat{P}_{\text{L}}$ to $\hat{X}_{\text{m}}$ and also $\hat{X}_{\text{L}}$ to $\hat{P}_{\text{m}}$. Therefore, more information about the mirror position can be gained by monitoring two orthogonal quadratures of light for instance via heterodyning.

6.1.3 Conditional state preparation and cooling protocol for this work

Feedback cooling techniques allow reducing the thermal occupation of mechanical states by continuously monitoring the optical field coupled to the mechanical motion and feeding this information back to the system. While this technique physically cools the mechanical motion, a quantum state represents the observer's knowledge about the state of the system and as such it is affected by the act of measurement alone without the feedback. The state can be conditioned on the outcome of the measurement as a result of which its position uncertainty and hence purity are reduced. Conditional state preparation schemes were considered in pulsed optomechanics [78] and experimentally demonstrated in [44]. Optimal state estimation via continuous monitoring was reported in [41] by applying a Kalman-filtering approach. Both of the experiments relied on radiation pressure coupling and monitoring of the optical field by means of homodyning.

This chapter presents a protocol, based on a stochastic master equation model, that is applied offline to the data obtained from the optomechanical system explained in chapter 5. The protocol optimally estimates the phase space trajectories of the mechanical mode and subsequently cools it by means of reducing the uncertainty associated with its phase space coordinates. In the experiment, the evanescently coupled pump light scatters off the 11 GHz mechanical mode into the anti-Stokes mode which provides the first pre-cooling stage for the mechanical motion. The physical process respnsible for the optomechanical coupling is electrostriction and the interaction Hamiltonian takes the form of a BS interaction. The anti-Stokes light is continuously monitored by a heterodyne detector which gives more information about the mechanical position when compared to homodyne monitoring for this interaction Hamiltonian. The heterodyne data is then used offline alongside the appropriate stochastic Gaussian model of the system [79] to prepare a mechanical state conditioned on the past measurements. This effectively purifies the state by reducing its phase space variance. The analysis is applied to the data in collaboration with Klaus Mølmer and Jinglei Zhang at the University of Aarhus. Such a protocol greatly enhances sideband cooling techniques and shows superiority over the commonly used homodyne detection. A manuscript on this work is currently in preparation for submission and publication.

6.2 Effective phonon number

The figure of merit quantifying the amount of cooling for this protocol is the effective phonon number defined as [78]

$$\bar{n}_{\text{eff}} = \sqrt{\sigma_{\text{max}}^2 \sigma_{\text{min}}^2} - \frac{1}{2}, \tag{6.1}$$

where σ_{max}^2 and σ_{min}^2 are the maximum and minimum variances of the quadratures of the measured mechanical mode positioned back at the origin after the measurement. The mechanical state conditioned on the heterodyne outcome is displaced from the origin and also squeezed due to the finite heterodyne frequency. The effective phonon number defined in Eqn. (6.1) quantifies state purity and as such is insensitive to displacement and squeezing operations. It is derived by considering a displaced, squeezed thermal state and calculating its thermal occupation after displacing it back to the origin and undergoing the inverse of the squeezing operation. The derivation is as follows. Thermal occupation of the mechanical mode $\hat{b}$ is

$$\bar{n} = \langle \hat{b}^\dagger \hat{b} \rangle = \frac{1}{2} \left(\langle \hat{X}_{\text{max}}^2 \rangle + \langle \hat{P}_{\text{mim}}^2 \rangle + \mathrm{i} \langle [\hat{X}_{\text{max}}, \hat{P}_{\text{min}}] \rangle \right), \tag{6.2}$$

where $\hat{X}_{\mathrm{max}}$ and $\hat{P}_{\mathrm{min}}$ are the quadratures along which the mechanical state's variance is maximum and minimum respectively. Angular brackets denote the expectation value. Using $\langle[\hat{X}_{\mathrm{max}}, \hat{P}_{\mathrm{max}}]\rangle = \mathrm{i}$ and the fact that $\sigma^2_{\mathrm{max}} = \langle\hat{X}^2_{\mathrm{max}}\rangle$, and $\sigma^2_{\mathrm{min}} = \langle\hat{P}^2_{\mathrm{min}}\rangle$ for a squeezed thermal state positioned at the origin of phase space, the phonon number can be expressed as

$$\bar{n} = \frac{1}{2}\left(\sigma^2_{\mathrm{max}} + \sigma^2_{\mathrm{min}}\right) - \frac{1}{2}. \tag{6.3}$$

Finally, a state with no squeezing has equal quadrature variances denoted by σ^2. Since squeeze operation preserves the area element in phase space, σ^2 relates to the quadrature variances of the squeezed mechanical state via $\pi\sigma^2 = \pi\sqrt{\sigma^2_{\mathrm{max}}\sigma^2_{\mathrm{min}}}$. Using this relation, the effective phonon number is $\bar{n} = \bar{n}_{\mathrm{eff}} = \sigma^2 - \frac{1}{2} = \sqrt{\sigma^2_{\mathrm{max}}\sigma^2_{\mathrm{min}}} - \frac{1}{2}$ as defined in Eqn. (6.1).

6.3 Toy model

The following calculation is a simplified model of the mechanical motion cooling protocol, where the continuous heterodyne monitoring of the optical mode is replaced by a single projection onto a coherent state. While continuous conditioning on the measurement outcomes is an optimal strategy for learning about the system, a single shot measurement already provides some knowledge of where the mechanical mode lies in phase space. The toy model gives an intuition of how the cooling protocol behaves.

The toy model considers a beam-splitter interaction between the mechanical mode in a thermal state $\hat{\rho}_{\mathrm{m}} = 1/(\pi\bar{n}_{\mathrm{b}})\int_{-\infty}^{+\infty} \mathrm{e}^{-|\alpha|^2/\bar{n}_{\mathrm{b}}}|\alpha\rangle\langle\alpha|\mathrm{d}^2\alpha$ and optical anti-Stokes mode initially in a vacuum state $\hat{\rho}_{\mathrm{aS}} = |0\rangle\langle 0|$. The mechanical mode has initial thermal occupation $\bar{n}_{\mathrm{b}}$. $|\alpha\rangle$ denotes a coherent state with complex amplitude $\alpha = 1/\sqrt{2}\left(\langle\hat{X}_\alpha\rangle + \mathrm{i}\langle\hat{P}_\alpha\rangle\right)$ and $\mathrm{d}^2\alpha = \mathrm{d}\,\mathrm{Re}[\alpha]\,\mathrm{d}\,\mathrm{Im}[\alpha]$.

The beam splitter of amplitude reflectivity r and transmissivity $t = \sqrt{1-r^2}$ partially state-swaps the optomechanical state towards hotter optical mode and cooler mechanical mode. This results in sideband cooling of the mechanical motion. The optical output is projected onto a coherent state $|\mu\rangle$ with complex amplitude $\mu = 1/\sqrt{2}\left(\langle \hat{X}_\mu\rangle + \mathrm{i}\langle \hat{P}_\mu\rangle\right)$. Since the beam splitter couples $\hat{X}_{\mathrm{aS}}$ to $\hat{P}_{\mathrm{m}}$ and $\hat{P}_{\mathrm{aS}}$ to $\hat{X}_{\mathrm{m}}$, the projection further narrows down the uncertainty associated with the mechanical position and momentum quadratures. The toy model is shown pictorially in Fig. (6.1).

The initial optomechanichal state is

$$\hat{\rho} = \hat{\rho}_{\mathrm{m}} \otimes \hat{\rho}_{\mathrm{aS}}. \tag{6.4}$$

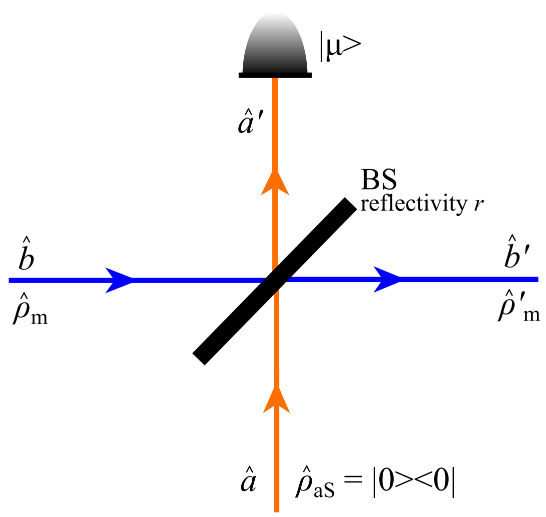

Figure 6.1: Toy model of the cooling protocol. Mechanical mode $\hat{b}$ in a thermal state $\hat{\rho}_{\mathrm{m}}$ and optical anti-Stokes mode $\hat{a}$ in a vacuum state interact on a beam splitter leading to sideband cooling of the mechanical motion. The outgoing optical field $\hat{a}'$ is then projected onto a coherent state $|\mu\rangle$ further reducing the uncertainties associates with the mechanical quadratures in mode $\hat{b}'$.

The beam splitter operator $\hat{B}$ transforms the optical $\hat{a}$ and mechanical $\hat{b}$ modes according to

$$\begin{aligned}\hat{a}' &= \hat{B}\hat{a}\hat{B}^\dagger = t\hat{a} + \mathrm{i}r\hat{b}\\ \hat{b}' &= \hat{B}\hat{b}\hat{B}^\dagger = t\hat{b} + \mathrm{i}r\hat{a}\end{aligned} \tag{6.5}$$

Using Eqn. (6.5) and the fact that amplitudes of coherent states transform the same as their annihilation operators, state ρ after the beam splitter transforms to

$$\hat{\rho}' = \hat{B}\hat{\rho}\hat{B}^\dagger = \frac{1}{\pi\bar{n}_\mathrm{b}}\int_{-\infty}^{+\infty} \mathrm{e}^{-|\alpha|^2/\bar{n}_\mathrm{b}} \left(|t\alpha\rangle_{b'}\langle t\alpha|_{b'}\right) \otimes \left(|\mathrm{i}r\alpha\rangle_{a'}\langle \mathrm{i}r\alpha|_{a'}\right) \mathrm{d}^2\alpha, \tag{6.6}$$

where subscripts a' and b' denote beam splitter output modes $\hat{a}'$ and $\hat{b}'$. After projecting the optical output mode onto coherent state $|\mu\rangle$, the remaining state in the mechanical mode is

$$\begin{aligned}\hat{\rho}'_\mathrm{m} &= \frac{N}{\pi\bar{n}_\mathrm{b}}\int_{-\infty}^{+\infty} \mathrm{e}^{-|\alpha|^2/\bar{n}_\mathrm{b}} |t\alpha\rangle_{b'}\langle t\alpha|_{b'} |\langle\mu|\mathrm{i}r\alpha\rangle|^2 \mathrm{d}^2\alpha\\ &= \frac{N}{\pi\bar{n}_\mathrm{b}}\int_{-\infty}^{+\infty} \mathrm{e}^{-|\alpha|^2/\bar{n}_\mathrm{b} - |\mu - \mathrm{i}r\alpha|^2} |t\alpha\rangle_{b'}\langle t\alpha|_{b'} \mathrm{d}^2\alpha,\end{aligned} \tag{6.7}$$

where $|\langle\mu|\mathrm{i}r\alpha\rangle|^2 = \mathrm{e}^{-|\mu-\mathrm{i}r\alpha|^2}$ was used to obtain the second line. $N = \mathrm{e}^{|\mu|^2/(1+\bar{n}_\mathrm{b}r^2)}\left(1+\bar{n}_\mathrm{b}r^2\right)$ is the normalisation constant such that $\mathrm{Tr}\left[\hat{\rho}'_\mathrm{m}\right] = 1$. To calculate the variance of the resulting mechanical position $\hat{X}_\mathrm{m}$ and momentum $\hat{P}_\mathrm{m}$ quadratures, it is useful to first compute the expectation values of $\hat{X}_\mathrm{m}$, $\hat{X}_\mathrm{m}^2$, $\hat{P}_\mathrm{m}$ and $\hat{P}_\mathrm{m}^2$. They are

$$\begin{aligned}\langle\hat{X}_\mathrm{m}\rangle &= \mathrm{Tr}\left[\hat{\rho}'_\mathrm{m}\hat{X}_\mathrm{m}\right] = \frac{\bar{n}_\mathrm{b} r\sqrt{1-r^2}}{1+\bar{n}_\mathrm{b}r^2}\langle\hat{P}_\mu\rangle\\ \langle\hat{X}_\mathrm{m}^2\rangle &= \mathrm{Tr}\left[\hat{\rho}'_\mathrm{m}\hat{X}_\mathrm{m}^2\right] = \frac{1+2\bar{n}_\mathrm{b} - \bar{n}_\mathrm{b}^2 r^2\left(-2+r^2+2\langle\hat{P}_\mu\rangle^2\left(r^2-1\right)\right)}{2\left(1+\bar{n}_\mathrm{b}r^2\right)^2}\\ \langle\hat{P}_\mathrm{m}\rangle &= \mathrm{Tr}\left[\hat{\rho}'_\mathrm{m}\hat{P}_\mathrm{m}\right] = -\frac{\bar{n}_\mathrm{b} r\sqrt{1-r^2}}{1+\bar{n}_\mathrm{b}r^2}\langle\hat{X}_\mu\rangle\\ \langle\hat{P}_\mathrm{m}^2\rangle &= \mathrm{Tr}\left[\hat{\rho}'_\mathrm{m}\hat{P}_\mathrm{m}^2\right] = \frac{1+2\bar{n}_\mathrm{b} - \bar{n}_\mathrm{b}^2 r^2\left(-2+r^2+2\langle\hat{X}_\mu\rangle^2\left(r^2-1\right)\right)}{2\left(1+\bar{n}_\mathrm{b}r^2\right)^2},\end{aligned} \tag{6.8}$$

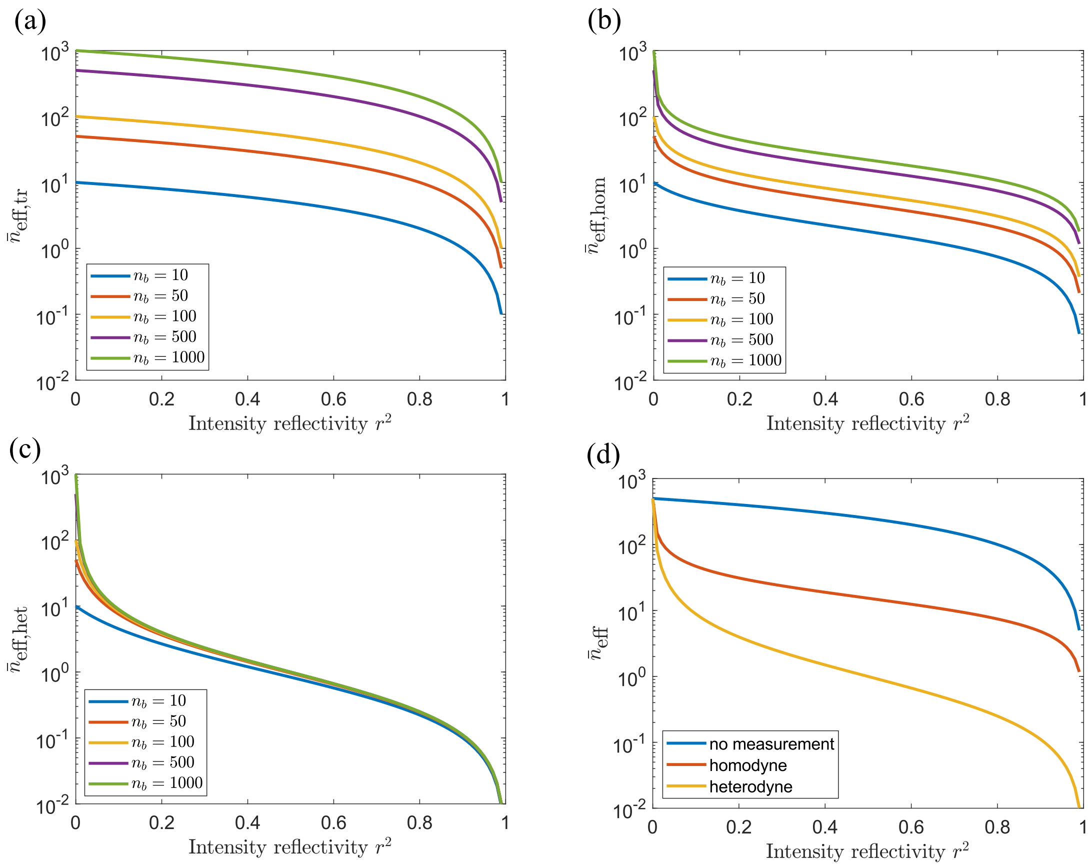

Figure 6.2: Effective phonon number given by the toy model as a function of the BS intensity reflectivity for different optical detection schemes and initial thermal occupations. **(a)** Here, $\bar{n}_{\text{eff}}$ decreases due to the BS interaction only. Therefore, to achieve low $\bar{n}_{\text{eff}}$, very small n_{b} or high r are required. **(b)** $\bar{n}_{\text{eff}}$ decreases due to the BS interaction and the information gained about one of the quadratures in the homodyne measurement. **(c)** Access to both quadratures further reduces $\bar{n}_{\text{eff}}$. When $\bar{n}_{\text{b}} r^2 >> 1$, $\bar{n}_{\text{eff}} \to \left(1 - r^2\right)/r^2$ and therefore is independent of the initial mechanical occupation number $\bar{n}_{\text{b}}$. **(d)** Direct comparison of the three detection schemes for $\bar{n}_{\text{b}} = 500$.

where $\langle \hat{X}_\mu \rangle$ and $\langle \hat{P}_\mu \rangle$ are the measured estimates of the anti-Stokes field quadratures such that $\langle \hat{X}_{\text{aS}} \rangle = \langle \hat{X}_\mu \rangle$ and $\langle \hat{P}_{\text{aS}} \rangle = \langle \hat{P}_\mu \rangle$. Therefore, the final variances of $\hat{X}_{\text{m}}$ and $\hat{P}_{\text{m}}$ are respectively

$$
\begin{aligned}
\sigma_X^2 &= \langle \hat{X}_{\text{m}}^2 \rangle - \langle \hat{X}_{\text{m}} \rangle^2 = -\frac{1}{2} + \frac{1 + \bar{n}_{\text{b}}}{1 + \bar{n}_{\text{b}} r^2} \\
\sigma_P^2 &= \langle \hat{P}_{\text{m}}^2 \rangle - \langle \hat{P}_{\text{m}} \rangle^2 = -\frac{1}{2} + \frac{1 + \bar{n}_{\text{b}}}{1 + \bar{n}_{\text{b}} r^2}.
\end{aligned}
\tag{6.9}
$$

The variances are the same because projection onto a coherent state gives the same information about $\hat{X}_\mathrm{m}$ and $\hat{P}_\mathrm{m}$, and the same is true for a heterodyne measurement operating at an infinite heterodyne frequency. In this experiment, ω_HET is finite which results in asymmetries in information gained about the two quadratures. However, since $\omega_\mathrm{HET} \sim 150$ MHz is appreciably greater than the mechanical decay rate $2\gamma_\mathrm{m}/2\pi \sim 42$ MHz, this asymmetry is not very significant. Eqn. (6.1) gives the following effective phonon number for this single coherent state projection,

$$\bar{n}_{\mathrm{eff,\,het}} = \frac{\bar{n}_\mathrm{b}\left(1-r^2\right)}{1+\bar{n}_\mathrm{b} r^2}. \tag{6.10}$$

The same procedure can be repeated to obtain effective phonon numbers when projecting the optical field onto a single quadrature and when tracing out the optical mode. The former case corresponds to a single homodyne measurement whereas the latter to ignoring the measurement outcome. The resulting effective phonon numbers for the single quadrature projection and tracing out the optical mode are respectively

$$\bar{n}_{\mathrm{eff,\,hom}} = \sqrt{\frac{1}{4} + \frac{\bar{n}_\mathrm{b}\left(1-r^2\right)\left(1+\bar{n}_\mathrm{b}\right)}{1+2\bar{n}_\mathrm{b} r^2}} - \frac{1}{2} \tag{6.11}$$

and

$$\bar{n}_{\mathrm{eff,\,tr}} = \bar{n}_\mathrm{b}\left(1-r^2\right). \tag{6.12}$$

The analytical forms in Eqn. (6.10), Eqn. (6.11) and Eqn. (6.12) show that $\bar{n}_{\mathrm{eff,\,het}} < \bar{n}_{\mathrm{eff,\,hom}} < \bar{n}_{\mathrm{eff,\,tr}}$ given $r > 0$. Plots in Fig. (6.2) further compare the three detection schemes for different $\bar{n}_\mathrm{b}$ and against each other.

6.4 Continuous measurement cooling theory

Although the toy model, presented in the previous section, gives an intuitive view of how different detection schemes perform in cooling of the mechanical mode, it does not capture the full physics of the process. In particular, it does not consider the continuous nature of the detection scheme, the finite optomechanical interaction time and the finite lifetime of the participating photons and phonons.

6.4.1 Stochastic master equation

The time evolution of this open quantum system can be appropriately modelled by a stochastic master equation. Since the monitoring of the optical mode is by means of a Gaussian detection, the suitable master equation must contain measurement involving Gaussian-distributed noise. The master equation takes the form [7, 79]

$$\mathrm{d}\hat{\rho} = -\frac{\mathrm{i}}{\hbar}\left[\hat{H},\hat{\rho}\right]\mathrm{d}t + \sum_h \mathcal{D}\left[\hat{c}_h\right]\hat{\rho}\mathrm{d}t + \sum_h \sqrt{\eta_h}\mathcal{H}\left[\hat{c}_h\right]\hat{\rho}\mathrm{d}W_h\left(t\right), \tag{6.13}$$

where $\hat{\rho}\left(t\right)$ is the state of the system, $\{\hat{c}_h\}$ are the participating dissipation operators, and $\mathcal{D}$ and $\mathcal{H}$ are the Lindblad and measurement superoperators defined as

$$\mathcal{D}\left[\hat{c}\right]\hat{\rho} = \hat{c}\hat{\rho}\hat{c}^\dagger - \frac{1}{2}\left(\hat{c}^\dagger\hat{c}\hat{\rho} + \hat{\rho}\hat{c}^\dagger\hat{c}\right) \tag{6.14}$$

and

$$\mathcal{H}\left[\hat{c}\right]\hat{\rho} = \hat{c}\hat{\rho} + \hat{\rho}\hat{c}^\dagger - \left\langle \hat{c} + \hat{c}^\dagger \right\rangle \hat{\rho}. \tag{6.15}$$

The first term on the right hand side of Eqn. (6.13) is the free Hamiltonian evolution, the second summation term describes dissipation into and out of the system and the last summation term is the information gain during the measurement of the dissipation channels with efficiency η_h. $\mathrm{d}W_h(t)$ is the associated Wiener increment which satisfies

$$\langle \mathrm{d}W_h(t)\rangle = 0, \qquad \left\langle \mathrm{d}W_h(t)\,\mathrm{d}W_h\left(t'\right)\right\rangle = 0 \text{ for } t' \neq t \tag{6.16}$$

and

$$(\mathrm{d}W_h(t))^2 = \mathrm{d}t. \tag{6.17}$$

The Wiener process is a stochastic process with normally distributed increments $\mathrm{d}W(t)$ with mean 0 and standard deviation $\sqrt{\mathrm{d}t}$. In Eqn. (6.13), it models the random nature of vacuum noise during a Gaussian measurement process. For the system presented in this work, there are three dissipation operators: $\hat{c}_1 = \sqrt{2\gamma_\mathrm{m}(\bar{n}_\mathrm{b}+1)}\hat{b}$, $\hat{c}_2 = \sqrt{2\gamma_\mathrm{m}\bar{n}_\mathrm{b}}\hat{b}^\dagger$ and $\hat{c}_3 = \sqrt{2\kappa_\mathrm{aS}}\hat{a}_\mathrm{aS}e^{-\mathrm{i}\omega_\mathrm{HET}t}$. They describe thermal phonon absorption and emission from the mechanical mode, and vacuum absorption into the monitored anti-Stokes mode respectively. The anti-Stokes mode is monitored by a heterodyne detection with total efficiency η and heterodyne frequency $\omega_\mathrm{HET}/2\pi$. The resulting stochastic master equation describing this optomechanical system is

$$\begin{aligned}\mathrm{d}\hat{\rho} = &-\frac{\mathrm{i}}{\hbar}\left[\hat{H},\hat{\rho}\right]\mathrm{d}t + 2\gamma_\mathrm{m}(\bar{n}_\mathrm{b}+1)\mathcal{D}\left[\hat{b}\right]\hat{\rho}\mathrm{d}t + 2\gamma_\mathrm{m}\bar{n}_\mathrm{b}\mathcal{D}\left[\hat{b}^\dagger\right]\hat{\rho}\mathrm{d}t + \\ &+ 2\kappa_\mathrm{aS}\mathcal{D}\left[\hat{a}_\mathrm{aS}e^{-\mathrm{i}\omega_\mathrm{HET}t}\right]\hat{\rho}\mathrm{d}t + \sqrt{2\kappa_\mathrm{aS}\eta}\mathcal{H}\left[\hat{a}_\mathrm{aS}e^{-\mathrm{i}\omega_\mathrm{HET}t}\right]\hat{\rho}\mathrm{d}W(t).\end{aligned} \tag{6.18}$$

6.4.2 Gaussian state evolution

The optomechanical state is initially Gaussian and performing a Gaussian measurement, such as heterodyne, leaves the remaining state Gaussian [80, 79]. Therefore, the system is fully described by its first and second moments at all times. The first moment is denoted by vector $\langle\hat{\mathbf{r}}\rangle = \left(\langle\hat{X}_\mathrm{m},\hat{P}_\mathrm{m},\hat{X}_\mathrm{aS},\hat{P}_\mathrm{aS}\rangle\right)^\mathrm{T}$ with $\hat{\mathbf{r}} = (\hat{r}_1,\hat{r}_2,\hat{r}_3,\hat{r}_4)^\mathrm{T}$. The covariance matrix is represented by **Cov** with elements $2\sigma^2_{jk} = \left\langle\{\hat{r}_j,\hat{r}_k\}\right\rangle - 2\left\langle\hat{r}_j\right\rangle\langle\hat{r}_k\rangle$ such that the diagonal elements are twice the variances of position and momentum operators. The evolution of first and second moments of continuously monitored Gaussian states was calculated in [79] under the conditions that the Hamiltonian is at most quadratic and operators $\{\hat{c}_h\}$ are linear in the quadrature observables. Such constraints apply to the optomechanical system presented in this work. The evolution of first and second moments in the forward direction are

$$\mathrm{d}\langle\hat{\mathbf{r}}\rangle = \mathbf{A}\langle\hat{\mathbf{r}}\rangle\,\mathrm{d}t + \left(\mathbf{Cov}\,\mathbf{B}^\mathrm{T} - \mathbf{N}^\mathrm{T}\right)\sqrt{\eta}\,\mathrm{d}\mathbf{W} \tag{6.19}$$

and

$$\frac{\mathrm{d}\mathbf{Cov}}{\mathrm{d}t} = \mathbf{A}\,\mathbf{Cov} + \mathbf{Cov}\,\mathbf{A}^\mathrm{T} + \mathbf{D} - 2\left(\mathbf{Cov}\,\mathbf{B}^\mathrm{T} - \mathbf{N}^\mathrm{T}\right)\eta\left(\mathbf{Cov}\,\mathbf{B}^\mathrm{T} - \mathbf{N}^\mathrm{T}\right)^\mathrm{T}, \tag{6.20}$$

where superscript T denotes the transpose operation. Matrices **A**, **B**, **N**, **D** and η for the system described by the master equation in Eqn. (6.18) are

$$\mathbf{A} = \begin{pmatrix} -\gamma_\mathrm{m} & -\Delta & 0 & G \\ \Delta & -\gamma_\mathrm{m} & -G & 0 \\ 0 & G & -\kappa_\mathrm{aS} & 0 \\ -G & 0 & 0 & -\kappa_\mathrm{aS} \end{pmatrix} \tag{6.21}$$

$$\mathbf{B} = \begin{pmatrix} \sqrt{(1+\bar{n}_\mathrm{b})\,\gamma_\mathrm{m}} & 0 & 0 & 0 \\ \sqrt{\bar{n}_\mathrm{b}\gamma_\mathrm{m}} & 0 & 0 & 0 \\ 0 & 0 & \sqrt{\kappa_\mathrm{aS}}\cos\left(\omega_\mathrm{HET}\,t\right) & \sqrt{\kappa_\mathrm{aS}}\sin\left(\omega_\mathrm{HET}\,t\right) \end{pmatrix} \tag{6.22}$$

$$\mathbf{N}=\begin{pmatrix}\sqrt{(1+\bar{n}_{\mathrm{b}})\,\gamma_{\mathrm{m}}} & 0 & 0 & 0\\ -\sqrt{\bar{n}_{\mathrm{b}}\gamma_{\mathrm{m}}} & 0 & 0 & 0\\ 0 & 0 & \sqrt{\kappa_{\mathrm{aS}}}\cos\left(\omega_{\mathrm{HET}}t\right) & \sqrt{\kappa_{\mathrm{aS}}}\sin\left(\omega_{\mathrm{HET}}t\right)\end{pmatrix} \tag{6.23}$$

$$\mathbf{D}=\begin{pmatrix}4\left(\frac{1}{2}+\bar{n}_{\mathrm{b}}\right)\gamma_{\mathrm{m}} & 0 & 0 & 0\\ 0 & 4\left(\frac{1}{2}+\bar{n}_{\mathrm{b}}\right)\gamma_{\mathrm{m}} & 0 & 0\\ 0 & 0 & 2\kappa_{\mathrm{aS}} & 0\\ 0 & 0 & 0 & 2\kappa_{\mathrm{aS}}\end{pmatrix} \tag{6.24}$$

and

$$\eta=\begin{pmatrix}0 & 0 & 0\\ 0 & 0 & 0\\ 0 & 0 & \eta\end{pmatrix}. \tag{6.25}$$

$\mathrm{d}\mathbf{W}=\left(\mathrm{d}W_1,\mathrm{d}W_2,\mathrm{d}W_3=\mathrm{d}W\right)^{\mathrm{T}}$ is a three element column vector, but only the last element $\mathrm{d}W$ contributes since only the anti-Stokes mode is monitored. The measured heterodyne current $\mathrm{d}y$ relates to $\mathrm{d}W$ in the interval $\mathrm{d}t$ via

$$\mathrm{d}y\left(t\right)=\left\langle\hat{c}_3+\hat{c}_3^{\dagger}\right\rangle\mathrm{d}t+\mathrm{d}W\left(t\right). \tag{6.26}$$

Substituting $\hat{c}_3=\sqrt{2\kappa_{\mathrm{aS}}}\hat{a}_{\mathrm{aS}}\mathrm{e}^{-\mathrm{i}\omega_{\mathrm{HET}}t}$ and $\hat{a}_{\mathrm{aS}}=1/\sqrt{2}\left(\hat{X}_{\mathrm{aS}}+\mathrm{i}\hat{P}_{\mathrm{aS}}\right)$ into Eqn. (6.26) gives

$$\mathrm{d}y\left(t\right)=2\sqrt{\kappa_{\mathrm{aS}}\eta}\left\langle\hat{X}_{\mathrm{aS}}\cos\left(\omega_{\mathrm{HET}}t\right)+\hat{P}_{\mathrm{aS}}\sin\left(\omega_{\mathrm{HET}}t\right)\right\rangle\mathrm{d}t+\mathrm{d}W\left(t\right). \tag{6.27}$$

The measured current $\mathrm{d}y(t)$ is therefore used in the evolution of the vector of first moments in Eqn. (6.19) via the stochastic term $\mathrm{d}W(t)$. It can be obtained by rearranging Eqn. (6.27) to give

$$\mathrm{d}W(t) = \mathrm{d}y(t) - 2\sqrt{\kappa_{\mathrm{aS}}\eta}\left\langle \hat{X}_{\mathrm{aS}}\cos(\omega_{\mathrm{HET}}t) + \hat{P}_{\mathrm{aS}}\sin(\omega_{\mathrm{HET}}t)\right\rangle \mathrm{d}t. \tag{6.28}$$

It is important to note that the covariance equation, Eqn. (6.20), is a deterministic equation and as such it only requires the knowledge of system parameters, but not the measured heterodyne current. Eqn. (6.19) on the other hand is non-deterministic and depends on the stochastic measurement outcome.

In order to apply the Gaussian state evolution formalism in Eqn. (6.19) and Eqn. (6.20), and the relation in Eqn. (6.28), the measured current needs to be normalised such that the experimental vacuum noise increment $\mathrm{d}y_{\mathrm{vac}}(t)$ corresponds to the Wiener noise increment $\mathrm{d}W(t)$ with standard deviation $\sqrt{\mathrm{d}t}$. The normalisation procedure therefore requires measuring a vacuum time trace $\mathrm{d}y_{\mathrm{vac}}(t)$. For a signal sampled at a rate $1/\mathrm{d}t$ and measured with a detector of bandwidth at least $1/\mathrm{d}t$, the normalisation corresponds to a statement

$$\sqrt{\mathrm{d}t} = \alpha\sqrt{\mathrm{Var}\left(\mathrm{d}y_{\mathrm{vac}}\right)}, \tag{6.29}$$

where α is the normalisation constant. Therefore, the measured signal of interest $\mathrm{d}y_{\mathrm{meas}}(t)$ corresponds to $\mathrm{d}y(t)$ in Eqn. (6.27) via

$$\mathrm{d}y(t) = \alpha\mathrm{d}y_{\mathrm{meas}}(t), \tag{6.30}$$

where $\alpha = \sqrt{\mathrm{d}t/\mathrm{Var}\left(\mathrm{d}y_{\mathrm{vac}}\right)}$ by using Eqn. (6.29). However, as can be seen in Table (5.1), the sampling rate of 10 GHz, corresponding to $\mathrm{d}t = 0.1$ ns, is much greater than the detector's bandwidth of 350 MHz. As a result, the sampled signal is low pass filtered by the detector's finite response and $\mathrm{d}t$ given by the inverse of the sampling rate is not the correct quantity to use for normalisation.

6.4.3 Finite bandwidth detector

The effect of the detector's bandwidth on the measured vacuum noise is shown in Fig. (5.5a). The measured vacuum spectrum is flat up to $\sim$ 350 MHz and therefore the data contains the correct flat white noise spectrum up to this frequency. This bandwidth is high enough to resolve the evolution of the system studied in this work. See Table (5.1) for system parameters. The correct normalisation is therefore such that the measured vacuum noise frequency content is the same as the expected Wiener noise frequency content for the relevant frequencies. This can be investigated by considering the cumulative power spectrum up to frequency ω for $\mathrm{d}W(t)$ and $\mathrm{d}y_{\mathrm{vac}}(t)$. In general, a cumulative power spectrum $\tilde{A}(\omega)$ for signal $f(t)$ can be defined as

$$\tilde{A}(\omega) = \sum_{\omega'<\omega} |\tilde{f}(\omega')|^2, \tag{6.31}$$

where $\tilde{f}(\omega')$ is the Fourier component of $f(t)$. The variances of $\mathrm{d}W$ and $\mathrm{d}y_{\mathrm{vac}}$ are proportional to their corresponding cumulative power spectra via Parseval's theorem as shown below,

$$\begin{aligned}
\mathrm{Var}(\mathrm{d}W) &= \frac{1}{N}\sum_{t<T} |\mathrm{d}W(t)|^2 \propto \sum_{\omega'<\omega} |\mathrm{d}\tilde{W}(\omega')|^2 = \tilde{A}_W(\omega) \\
\mathrm{Var}(\mathrm{d}y_{\mathrm{vac}}) &= \frac{1}{N}\sum_{t<T} |\mathrm{d}y_{\mathrm{vac}}(t)|^2 \propto \sum_{\omega'<\omega} |\mathrm{d}\tilde{y}_{\mathrm{vac}}(\omega')|^2 = \tilde{A}_{\mathrm{vac}}(\omega),
\end{aligned} \tag{6.32}$$

where N is the number of data points over which the variances are taken. $\tilde{A}_W(\omega)$ and $\tilde{A}_{\mathrm{vac}}(\omega)$ are the cumulative power spectra for $\mathrm{d}W(t)$ and $\mathrm{d}y_{\mathrm{vac}}(t)$ respectively. For ideal white noise, it is expected that $\tilde{A}(\omega) = k\omega$, where k is a constant. Therefore, the normalisation constant α can

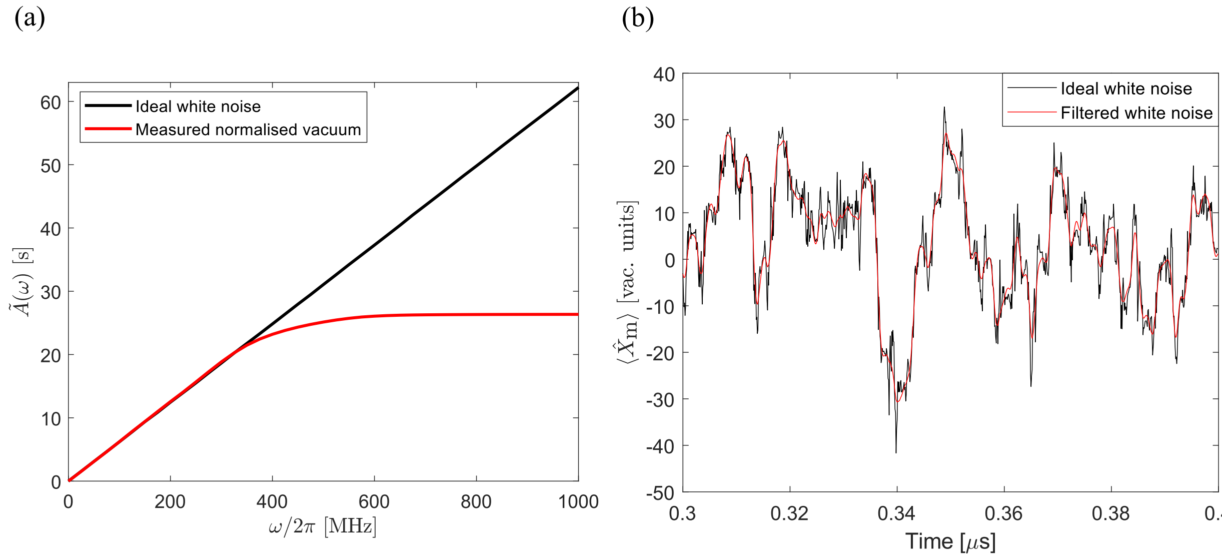

Figure 6.3: Check that the normalisation procedure in Eqn. (6.34) gives the correct vacuum noise power spectrum and mechanical oscillator's phase space trajectories up to the bandwidth of the detector. **(a)** Cumulative power spectra of the simulated ideal white noise and the measured normalised vacuum noise. The spectra are the same up to the bandwidth of the detector if the measured noise is appropriately normalised. **(b)** Simulated trajectories of the mechanical oscillator with ideal white noise and the same noise but low-pass filtered. Both cases capture the same system dynamics within the relevant time scales.

be found via

$$\sqrt{k_W} = \alpha \sqrt{k_{\text{vac}}}, \tag{6.33}$$

where $k_W = \tilde{A}_W(\omega)/\omega$ and $k_{\text{vac}} = \tilde{A}_{\text{vac}}(\omega)/\omega$ for ω satisfying $\tilde{A}_{\text{vac}}(\omega) \propto \omega$. The cumulative power spectra of the correctly normalised measured vacuum noise and the ideal white noise are shown in Fig. (6.3a). Further, Fig. (6.3b) unveils simulated trajectories of the mechanical oscillator with ideal white noise and the same noise but low-pass filtered. It shows that the action of the filter does not affect the oscillator's trajectories on time scales relevant for the system evolution if appropriate normalisation is applied .

Therefore, in the case of finite bandwidth detection, the measured current $\mathrm{d}y_{\text{meas}}(t)$ can be related to $\mathrm{d}y(t)$ in Eqn. (6.27) by substituting for α from Eqn. (6.33) into Eqn. (6.30). This yields

$$\mathrm{d}y(t) = \sqrt{\frac{k_W}{k_{\text{vac}}}}\mathrm{d}y_{\text{meas}}(t). \tag{6.34}$$

The protocol described via Eqn. (6.19) and Eqn. (6.20) with $dW(t)$ found using an appropriately normalised measurement current (Eqn. (6.27) and Eqn. (6.34)) can be used to prepare a conditional state of mechanical motion for the system studied in this work.

6.4.4 Sideband cooling analytical expression

When the optical mode is not monitored, the mechanical mode is still cooled due to the anti-Stokes scattering invoked by the beam-splitter interaction. The mechanical motion is therefore sideband cooled and this is pictorially illustrated in Fig. (5.2). The covariance evolution formalism in Eqn. (6.20) can be used to find the resulting quadrature variances of the mechanical mode without the measurement by setting $\eta = 0$. The variances can then be substituted into Eqn. (6.1) to find the effective phonon number.

Solving Eqn. (6.20) yields the following analytical expression for the effective phonon number,

$$\bar{n}_{\text{eff, sc}} = \bar{n}_{\text{b}} \gamma_{\text{m}} \frac{G^2 + \kappa_{\text{aS}}^2 + \kappa_{\text{aS}} \gamma_{\text{m}}}{\left(G^2 + \kappa_{\text{aS}} \gamma_{\text{m}}\right)\left(\kappa_{\text{aS}} + \gamma_{\text{m}}\right)}, \tag{6.35}$$

where subscript sc stands for sideband cooling. In the limit of $G^2 \gg \kappa_{\text{aS}}\left(\kappa_{\text{aS}} + \gamma_{\text{m}}\right)$, the effective phonon number is

$$\lim_{G^2 \gg \kappa_{\text{aS}}\left(\kappa_{\text{aS}} + \gamma_{\text{m}}\right)} \bar{n}_{\text{eff, sc}} = \bar{n}_{\text{b}} \frac{\gamma_{\text{m}}}{\left(\kappa_{\text{aS}} + \gamma_{\text{m}}\right)}. \tag{6.36}$$

In principle, the cooling is limited by the initial thermal bath occupation and linewidths of the optical and mechanical modes. There is no associated quantum backaction limit which exists in the radiation pressure coupling, where the minimum phonon occupation number is $\bar{n}_{\text{min}} = (\kappa/2\omega_{\text{m}})^2$ at $\gamma_{\text{m}} = 0$.

6.4.5 Measurement enhanced cooling protocol summary

The following points summarise the procedure for the measurement enhanced cooling of the mechanical mode.

1. Two optical modes of the microresonator separated by approximately 11 GHz are selected. The lower frequency mode is the pump mode, whereas the higher frequency mode is the anti-Stoke mode.

2. Laser light is evanescently coupled into the pump mode which scatters off the resonator's acoustic mode into the anti-Stokes mode. The interaction between the acoustic mode and the anti-Stokes mode can be represented by a beam-splitter Hamiltonian which leads to sideband cooling of the mechanical mode.

3. The resulting backscattered anti-Stokes light is measured in a heterodyne detector of bandwidth 350 MHz at a heterodyne frequency of $\omega_{\mathrm{HET}}/2\pi \sim 150$ MHz. The heterodyne signal is then recorded as a time trace of length 100 μs on an oscilloscope. A vacuum time trace of the same length is also measured for normalisation.

4. The mechanical state can be further cooled by means of reducing the uncertainty associated with its phase space trajectories by using the information contained in the recorded time traces. The number quantifying the amount of cooling is the effective phonon number defined in Eqn. (6.1).

5. The information about the phase space trajectories can be extracted from the time traces by using an appropriate stochastic master equation model. Since the system remains Gaussian throughout the evolution, it can be fully described by its first and second moments at all times. Their evolution is given in Eqn. (6.19) and Eqn. (6.20).

6. The covariance equation, Eqn. (6.20), is a deterministic equation and does not require the measurement record input. The equation for first moments, Eqn. (6.19), is a non-deterministic equation and the measured time trace can be input via the stochastic term $\mathrm{d}W(t)$ by using Eqn. (6.28). The measured current needs to be appropriately normalised using a vacuum time trace in conjunction with Eqn. (6.34).

7. Solving Eqn. (6.19) and Eqn. (6.20) allows estimating phase space trajectories of the optomechanical state and the associated reduced uncertainties which can also be expressed in terms of the effective phonon number.

6.5 Heterodyne versus homodyne measurement discussion

Monitoring the optical mode of an optomechanical state allows extracting information about the mechanical mode. As already highlighted in section 6.1.2, the optimal choice of the measurement depends on the optomechanical interaction Hamiltonian. The homodyne measurement is desirable for $\hat{X}_{\mathrm{L}}\hat{X}_{\mathrm{m}}$ interactions as the mechanical mode is coupled to a single quadrature of light $\hat{P}_{\mathrm{L}}$ only. The beam-splitter interaction, with interaction Hamiltonian proportional to $\hat{X}_{\mathrm{L}}^{\dagger}\hat{X}_{\mathrm{m}} + \hat{P}_{\mathrm{L}}^{\dagger}\hat{P}_{\mathrm{m}}$, encodes the information about the mechanical mode in both quadratures of light. Hence, monitoring both light quadratures, for instance via heterodyning, is more beneficial. The beam-splitter interaction corresponds to sideband cooling of the mechanical motion and as such further measurements of the optical mode enhance the amount of cooling by reducing the uncertainty of where the mechanical mode lies in phase space. The toy model, described in section 6.3, shows that a lower effective phonon occupation is achieved after heterodyning the optical mode as opposed to homodyning it. See Eqn. (6.10), Eqn. (6.11) and Fig. (6.2). Although the toy model gives a good intuitive understanding of the process, it doesn't

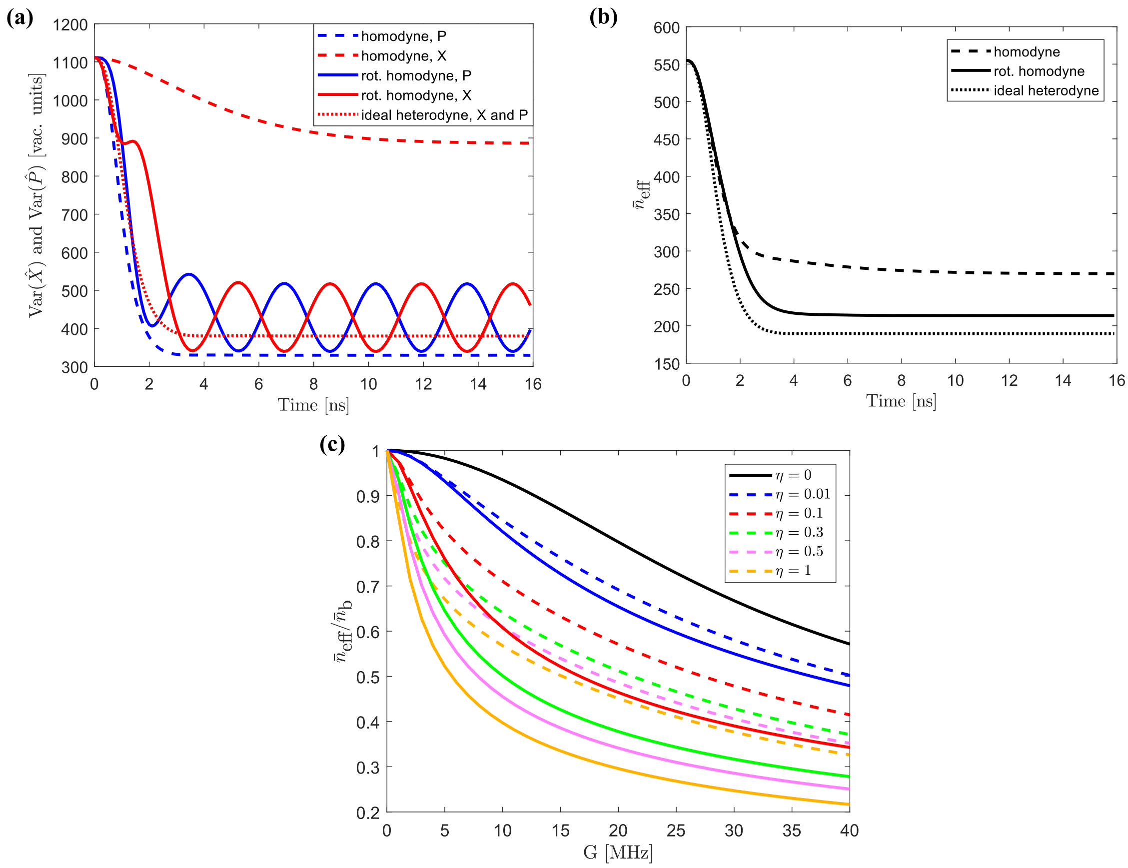

Figure 6.4: **(a)** Variances of mechanical quadratures for different measurement schemes as a function of time. **(b)** The corresponding effective phonon number. **(c)** Cooling factor as a function of optomechanical coupling strength G for different efficiencies η. Continuous lines correspond to an ideal heterodyne scheme ($\omega_{\rm HET} \to \infty$) and dashed lines to a homodyne scheme ($\omega_{\rm HET} = 0$). The curves show that the cooling factor approaches saturation for increasing values of G and η. Plots **(a)**, **(b)** and **(c)** are theoretical plots for the following system parameters: $2\kappa_{\rm aS}/2\pi = 90$ MHz, $2\gamma_{\rm m}/2\pi = 42$ MHz, $\Delta/2\pi = 0$ and $\bar{n}_{\rm b} = 555$. Plots **(a)** and **(b)** are plotted for $G/2\pi = 20$ MHz, $\eta = 0.5$ and in the case of rotating homodyne measurement, $\omega_{\rm HET} = 150$ MHz.

capture all the physics. In particular, it does not take into account the continuous nature of the measurement and the finite lifetimes of phonons and photons inside the mechanical and anti-Stokes modes respectively. The full system is studied using the stochastic master equation model of section 6.4 which can be further simplified to differential equations for means and covariances if the system is Gaussian.

While an ideal heterodyne detection operates at an infinite heterodyne frequency, the heterodyne scheme presented in this work uses $\omega_{\rm HET}/2\pi \sim 150$ MHz. Therefore, the detection scheme used in this work corresponds to a rotating homodyne measurement more precisely. Since $\omega_{\mathrm{HET}}/2\pi$ is much greater than the mechanical intensity decay rate, an ideal heterodyne measurement does not improve the rotating homodyne scheme significantly. This is shown in Fig. (6.4a) and Fig. (6.4b) for a realistic parameter regime. Fig. (6.4a) shows the oscillating variance at twice the heterodyne frequency for the rotating homodyne scheme and the corresponding variances for the homodyne and ideal heterodyne schemes. Fig. (6.4b) shows the corresponding effective phonon number, defined in Eqn. (6.1), using such detection schemes. Since the rotating homodyne variance is oscillating in time, an average over the oscillation period will be taken to obtain the variance for any future calculations.

While the heterodyne measurement uses all the anti-Stokes light to collect information about both optical quadratures, the homodyne detection uses the same light resources to learn about a single quadrature. It is therefore an interesting question to ask why it is overall more beneficial to use all the light to measure two quadratures as opposed to one quadrature but more precisely. Fig. (6.4c) provides some understanding towards this question. It shows the cooling factor, defined by

$$CF = \frac{\bar{n}_{\mathrm{eff}}}{\bar{n}_{\mathrm{b}}}, \tag{6.37}$$

for homodyne and heterodyne detections as a function of the enhanced optomechanical coupling strength G for different detection efficiencies η. In the weak coupling regime, it indeed seems that the net amount of cooling is similar for both detection schemes. However, for larger values of G, there is a saturation limit to how much a single quadrature can be cooled given by the dashed lines. A similar situation happens for η. After reaching certain efficiency, further increase in η does not gain much more information about the mechanical position.

6.6 Experimental results

Fig. (6.5) shows the outcomes of applying the Gaussian filter, described in section 6.4 and in particular summarised in subsection 6.4.5, to the time-domain data obtained by heterodyning the optical mode of the Brillouin system presented in chapter 5. The heterodyned light originated from scattering of the pump photons off the mechanical phonons to create the up-converted anti-Stokes photons that were detected. This interaction between the mechanical and anti-Stokes mode can be represented by a beam-splitter Hamiltonian (see Eqn. (5.14)) and led to sideband cooling of the mechanical mode. Ten time traces of total length of 100 μs were recorded at room temperature using an oscilloscope of sampling rate of 10 Gsamples/s. The datasets were taken for increasing values of the optomechanical strength G which has a square root scaling with the intracavity power P_{cav} as shown in Fig. (5.9). The self- and cross-Kerr effects led to optical power dependent detuning Δ between the anti-Stokes and pump modes as illustrated in Fig. (5.8). The taper-resonator coupling conditions were such that the anti-Stokes intensity decay rate was $2\kappa_{\mathrm{aS}}/2\pi \sim 91$ MHz. The total experimental efficiency was $\eta_{\mathrm{tot}} = 0.31$ and the heterodyne frequency was approximately 150 MHz. Details of the experimental setup can be found in section 5.3 and the relevant system parameters are further discussed in section 5.6 and listed in Table (5.1).

Fig. (6.5a) shows the estimated quadrature trajectories of the mechanical mode with standard deviations of the position and momentum quadratures denoted by shaded areas. The plots are for the dataset with highest $G/2\pi = 9.6$ MHz and the corresponding $\Delta/2\pi = -74$ MHz. The plots were obtained by solving the evolution equations for the first and second moments of the optomechanical state given in Eqn. (6.19) and Eqn. (6.20) respectively. The equation for the second moment gives the required variances of the mechanical phase space quadratures. It

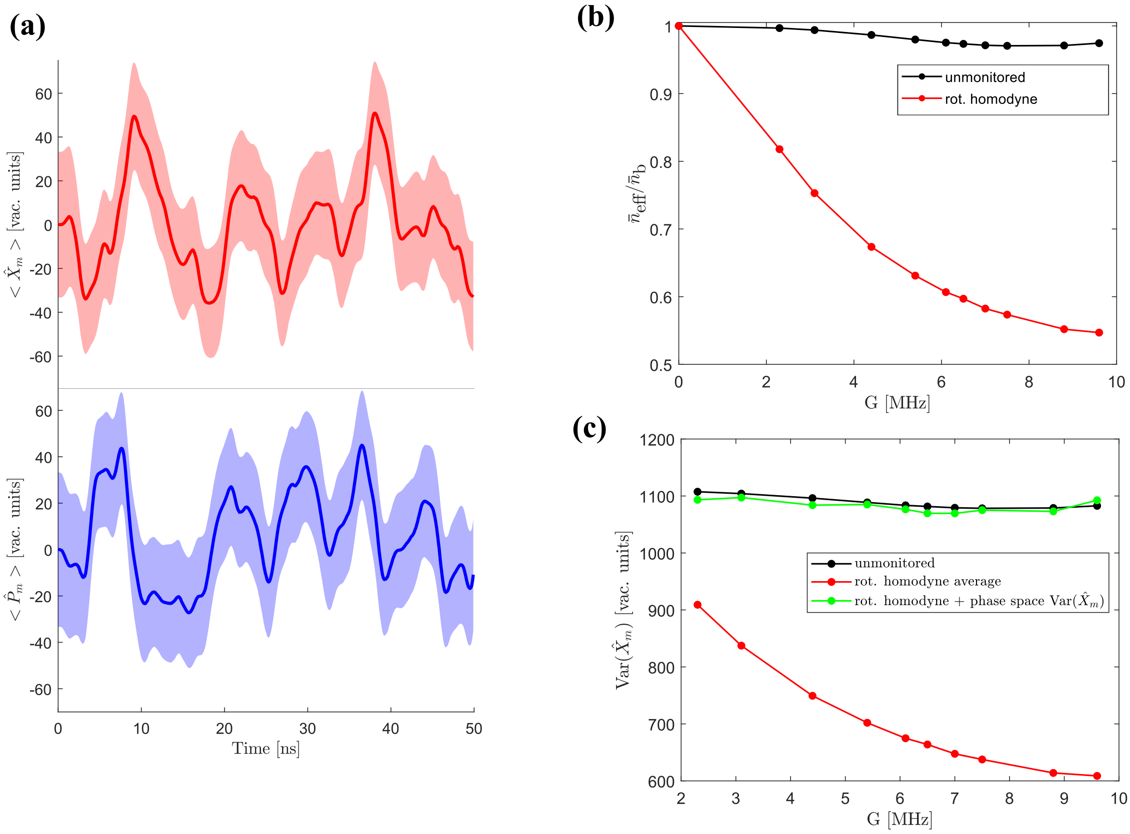

Figure 6.5: **(a)** Mechanical quadrature trajectories conditioned on the rotating homodyne measurement outcome. Shaded areas represent the standard deviations of quadratures $\hat{X}_{\rm m}$ and $\hat{P}_{\rm m}$. **(b)** Cooling achieved in the experiment (red points). Black points correspond to sideband cooling. **(c)** Total information budget before (black) and after the measurement (green). The green points are summations of the mechanical quadraturee variance after the measurement (red) and the variance of the estimated mechanical phase space trajectories during the measurement time of 100μs. The close overlap between the green and black points signifies that the formalism is self-consistent.

is a deterministic equation and therefore did not require an input from the measured current. The equation for the first moments gives the estimated phase space trajectories. It is a non-deterministic equation and as such required an input from the measurement record through the stochastic term $\mathrm{d}W(t)$ which relates to the measured current via Eqn. (6.28). The measured current was appropriately normalised so that the experimental vacuum noise increment corresponded to the Wiener noise increment with standard deviation $\sqrt{\mathrm{d}t}$ up to the bandwidth of the detector. Details of this procedure is given in subsection 6.4.3. Fig. (6.5a) illustrates that as the state evolves in time, the stochastic measurement outcome moves the mean values of $\hat{X}_\mathrm{m}$ and $\hat{P}_\mathrm{m}$ away from the original zero position. The uncertainties associated with $\hat{X}_\mathrm{m}$ and $\hat{P}_\mathrm{m}$ are reduced, and the amount by which the mechanical mode is cooled depends on two competing processes: the decoherence rates and the rate at which information is acquired during the measurement. Eventually, steady state is reached as shown in Fig. (6.4a).

The cooling factor, defined as the ratio of the effective phonon number $\bar{n}_\mathrm{eff}$ and the thermal phonon number $\bar{n}_\mathrm{b}$, for this room temperature experiment is shown in Fig. (6.5b) for the ten recorded datasets of varying G and Δ. $\bar{n}_\mathrm{b} = 555$ and $\bar{n}_\mathrm{eff}$ is defined in Eqn. (6.1) which depends on the minimum and maximum variances of the mechanical quadratures. The cooling factor therefore depends on the system parameters only regardless of whether the system is monitored or not. The black points quantify the amount of sideband cooling while the red points include the information gain due to the rotating homodyne measurement.

Since the quadrature variances and therefore the cooling factor do not require a measurement input, it is important to check that the determined system parameters are self-consistent with the enhanced measurement cooling theory. Fig. (6.5c) does that by considering the information budget for the mechanical mode before and after the measurement. It is expected that the unmonitored mechanical quadrature variance (black points) is the same as the sum of the variance after the measurement (red points) and the variance of the recorded mechanical phase space trajectories. The sum is given by the green points and requires an input of the measured current. The close overlap between green and black points suggests that the formalism is self-consistent.

6.7 Summary

The work presented in part II of this thesis explores the optomechanical interaction inside a Brillouin system comprised of a silica microrod resonator evanescently coupled to an external laser field. In particular, the study considers optical whispering gallery modes corresponding to wavelengths of ~ 1550 nm and the acoustic mode of frequency $\omega_{\mathrm{m}}/2\pi = 11$ GHz. By selecting two discrete optical modes separated by ω_{m} and pumping on the lower frequency mode, a beam-splitter interaction is created between the remaining higher frequency (anti-Stokes) mode and the mechanical mode. The interaction itself leads to sideband cooling of the mechanical mode by creating light in the anti-Stokes mode. The experiment operates at room temperature and can achieve strong coupling as reported in [3]. The anti-Stokes light is then continuously monitored by means of a heterodyne detection with a heterodyne frequency of $\omega_{\mathrm{HET}} \sim 150$ MHz. The measurement scheme is also referred to as rotating homodyne due to the finite heterodyne frequency. The experimental setup is shown in section 5.3 and the system parameters are listed in Table (5.1). The resulting heterodyne time traces are input into the appropriate Gaussian filter which describes how the system evolves under continuous monitoring. The Gaussian evolution model is explained in section 6.4. The protocol prepares a conditional state of mechanical motion with reduced effective phonon number, defined in Eqn. (6.1), which quantifies the improved purity of the state. The key conclusions are:

1. Continuous monitoring of the optical mode of an optomechanical state enhances sideband cooling of the corresponding mechanical mode.

2. Heterodyning the optical mode outperforms homodyning in cooling and purifying the mechanical state for beam-splitter interaction types since information about the mechanical mode is contained in both light quadratures.

3. A Gaussian filter [79] was successfully applied to the heterodyne time domain data obtained from a Brillouin optomechanical system at room temperature. The protocol produced a conditional state of mechanical motion with the corresponding trajectories and cooling factors shown in Fig. (6.5).

While sideband cooling is a common technique used in optomechanics and allows studying quantum regimes [37, 38, 40], appropriate filter models can enhance this technique and also be used in conjunction with feedback cooling methods. This creates opportunities for enhanced sensing applications as the thermal noise in the system is reduced.

Part III

Quantum limits in the simultaneous estimation of phase and phase diffusion

Chapter 7

Introduction to multi-parameter quantum metrology

Metrology, as the science of measurements, encapsulates a wide range of aspects from defining units of measure, developing more precise estimation schemes to understanding the fundamental limits associated with the parameter estimation process. These fundamental limits are set by quantum mechanics and as such provide deep insights into this field. In a typical estimation scenario, phase is the parameter of interest whose precision is limited by the presence of noise, such as dephasing and loss, in any experiment [10]. Although, the knowledge of phase and decoherence parameters enables the full characterisation of a system, less attention has been devoted towards studies of noise estimation schemes.

While the previous part presents an experiment to improve the sensitivity of an optomechanical system, this part describes the theory of an estimation process and the associated limits. In particular, it looks at the limits in the joint estimation of phase and phase diffusion in the Cramér-Rao bound framework with the emphasis on optical systems. The work presented in

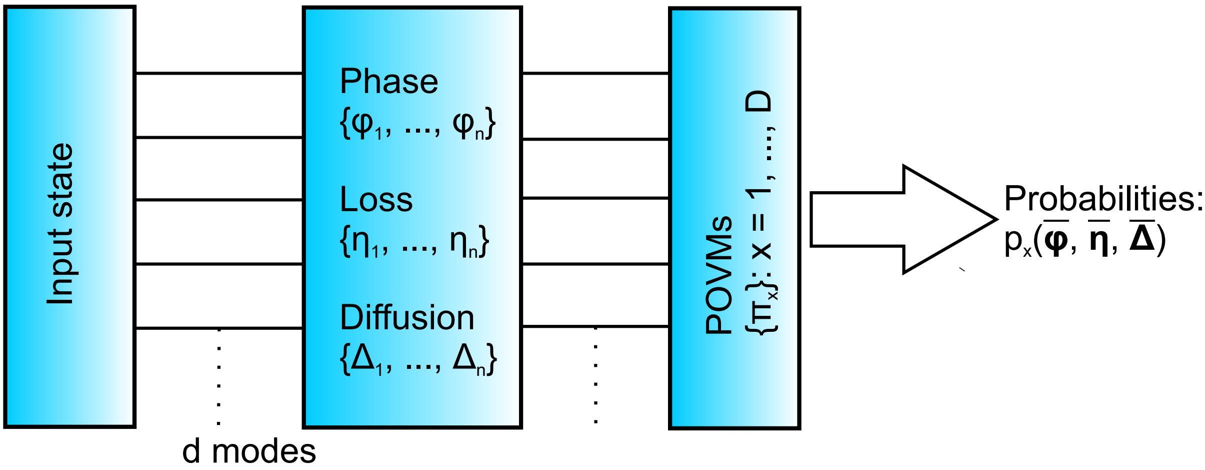

Figure 7.1: Three stages of the estimation process: 1. Probe state preparation. 2. Interaction of the probe with a parametrized system. 3. Measurement of the modified probe which results in probabilities that can be analysed to estimate the parameters of interest.

part III was published in Ref. [5] and a review article on multi-parameter quantum metrology was published in Ref. [4].

7.1 Shot noise and Heisenberg limits

As already mentioned in the main introduction, a typical estimation process can be divided into three stages: probe preparation, interaction with the system and probe readout. This is shown in Fig. (7.1). For a given interaction with the system, the choice of probe states and measurements determines the precision with which the parameters of interest can be measured. After the probe readout stage, the gathered statistics can be analysed by invoking an estimator function to yield an estimate of the parameters. All estimation schemes suffer from errors which can be either systematic or statistical. Statistical errors of a stochastic nature can be reduced through repeated interactions between the probe and the system (corresponding to M independent measurements), resulting in the typical statistical error (in standard deviation) scaling of $M^{-\frac{1}{2}}$. The origins of this scaling lies in the central limit theorem from probability theory, and is possible classically without the invocation of quantum mechanics. Given a probe of size (such as the number of particles or modes, energy) N, the best classical possible scaling is the so-called shot noise limit, whose error also scales as $N^{-\frac{1}{2}}$ [10]. Although the shot noise limit and the central limit theorem have the same quadratic dependence, they are of entirely different origins. In optics, the shot noise limit originates from the discrete nature of photons whose number distribution is Poissonian with the standard deviation of $N^{\frac{1}{2}}$, where N is the number of photons in this case.

Once the stochastic noise is suppressed, quantum mechanics is the final and most fundamental barrier to the precision of an estimation scheme. This inevitable limit is set by the quantum vacuum fluctuations and can only be overcome by invoking uniquely quantum mechanical techniques. Quantum probes endowed with such non-classical correlations can attain the so-called Heisenberg limit, identified by a N^{-1} scaling in the standard deviation [81, 82]. This enhanced scaling, leading to a more precise estimation, is at the root of the appeal of quantum metrology. Quantum metrology can find application in scientific areas from astronomy – detection of gravitational waves, to biology – imaging of biological samples sensitive to the total illumination [14, 17]. It has relevance to magnetic, electric, and gravitational field sensing, and more precise clock synchronisation protocols [83, 84].

Quantum metrology thus seeks scenarios where non-classical resources can provide improvements in the parameter estimation over the classical strategies and tries to identify the measurements that achieve quantum enhanced precisions. It must be understood that the quantum improvement can be availed only after all classical sources of stochastic noise have been suppressed. The most prominent example of this endeavour is the quest for the detection of gravitational waves using laser interferometry [85, 86].

7.2 Local and global estimation theories

Estimation theories can be categorised into global and local theories. In the global case, the parameter can be completely unknown and the estimation protocol enables finding the parameter of interest to some precision. Schemes based on the Bayesian theory, where the parameter is a random variable distributed according to some prior probability distribution, can be considered global [10, 87, 88]. On the other hand, in some circumstances, we may already have a good knowledge of the interval where the true parameter value lies. In such cases, local approaches could be beneficial to further improve the precision and accuracy of the parameters of interest. Examples of local precision bounds include the Barankin [89], Holevo [90] and Cramér-Rao bound (CRB). The last mentioned bound is of crucial importance for this part of my thesis.

7.3 Classical Cramér-Rao bound

Throughout part III of this thesis, bold quantities will refer to vectors of numbers or more generally to matrices, whereas the circumflex diacritic will denote operators.

A statistical quantity capturing the performance of an estimation process is the variance of the estimator. The estimator, labelled as T, is a function of the measured data which allows estimating the parameters of interest. Ideally, T should be unbiased, which means that its mean value should be equal to the true parameter value, and precise which means that its variance should be as low as possible. A crucial result from probability theory, the Cramér-Rao bound

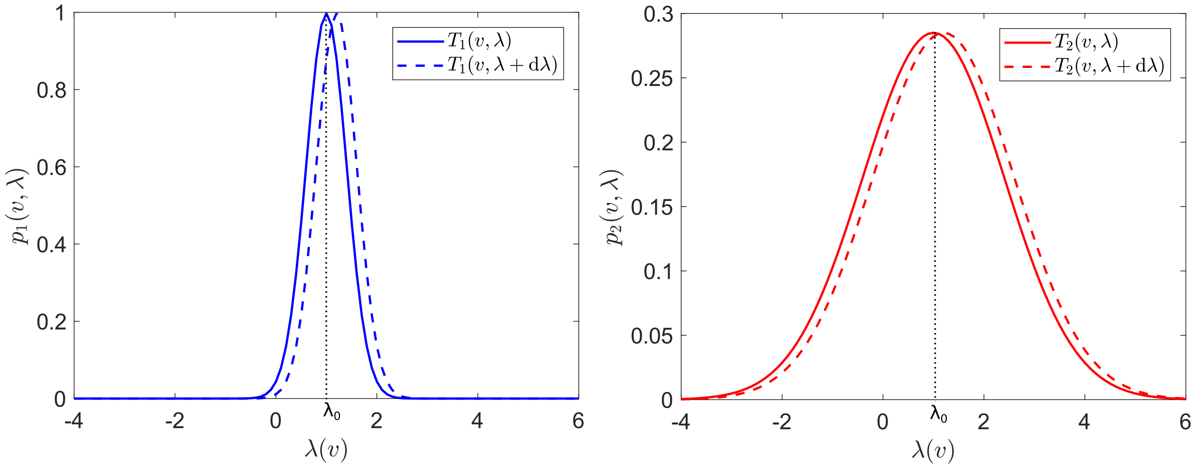

Figure 7.2: The two plots show probability distributions p_1 and p_2 associated with two estimator functions T_1 and T_2 for parameter λ (continuous curves) plotted against the possible parameter value $\lambda(v)$ based on measurements v. T_1 has narrower variance than T_2. In each plot, there is an additional distribution corresponding to parameter $\lambda + \mathrm{d}\lambda$ (dashed curves). The two distributions separated by an amount $\mathrm{d}\lambda$ are easier to distinguish in the case of T_1, where the narrower estimator variance indicates higher FI.

(CRB), states that the variance of an (unbiased) estimator is lower bounded by the inverse of the Fisher information (FI). The FI is a function of the probability distribution obtained at the end of an estimation process, and is of independent interest in probability theory, information theory, and information geometry [91]. More precisely, it is a distinguishability metric which provides a statistical distance on the space of probability distributions. It tells us how easily we can distinguish neighbouring probability distributions when separated by an infinitesimally small amount of the parameter value characterising the distributions. This is illustrated pictorially in Fig. (7.2). Therefore, the FI captures the amount of 'information' about a given parameter in a probability distribution. The single-parameter CRB is derived in the section below.

7.3.1 Single-parameter Cramér-Rao bound

The following derivation of the single-parameter CRB [92] considers a distribution $p(V;\lambda)$ of a random variable V parameterised by a single parameter λ. The distribution is normalised such that $\sum_y p\left(v_y;\lambda\right) = 1$, where the sum is taken over all possible measurement values v_y. M samples of data, $\{V^{(1)}, V^{(2)}, ..., V^{(M)}\}$ identically and independently distributed, are drawn from that distribution. The aim is to find the lower bound on the variance of an unbiased estimator $T\left(V^{(1)}, V^{(2)}, ..., V^{(M)};\lambda\right)$ for the parameter λ based on the samples $\{V^{(1)}, V^{(2)}, ..., V^{(M)}\}$. The unbiasedness condition implies $\langle T\rangle = \lambda$, where the angular brackets denote the expectation value taken with respect to $p(v;\lambda)$. The score function for $p(V;\lambda)$ for a single parameter λ and $M = 1$ is defined as

$$S = \partial_\lambda \left(\ln\left(p(V;\lambda)\right)\right) = \frac{\partial_\lambda\left(p(V;\lambda)\right)}{p(V;\lambda)} \tag{7.1}$$

with the mean value of

$$\langle S\rangle = \sum_y \frac{\partial_\lambda\left(p\left(v_y;\lambda\right)\right)}{p\left(v_y;\lambda\right)} p\left(v_y;\lambda\right) = 0. \tag{7.2}$$

The FI of parameter λ is the variance of the score given by

$$F(\lambda) = \langle S^2\rangle - \langle S\rangle^2 = \left\langle \left(\partial_\lambda\left(\ln p(V;\lambda)\right)\right)^2\right\rangle = \sum_y \frac{\left(\partial_\lambda\left(p\left(v_y;\lambda\right)\right)\right)^2}{p\left(v_y;\lambda\right)}. \tag{7.3}$$

The CRB lower bounds the variance of the estimator according to

$$\mathrm{Var}(T) \geq \frac{1}{F(\lambda)}. \tag{7.4}$$

This inequality can be proven using the Cauchy-Schwarz inequality which can be expressed as

$$\left(\mathrm{Cov}(S,T)\right)^2 \leq \mathrm{Var}(S)\,\mathrm{Var}(T), \tag{7.5}$$

where Cov(S, T) is the covariance between S and T. Using $\mathrm{Var}(S) = F(\lambda)$ and substituting in the definition of covariance, the above inequality reads

$$\langle (S - \langle S\rangle)(T - \langle T\rangle)\rangle^2 \leq F(\lambda)\,\mathrm{Var}(T). \tag{7.6}$$

Further, using $\langle S\rangle = 0$ from Eqn. (7.2), the inequality simplifies to

$$\langle ST\rangle^2 \leq F(\lambda)\,\mathrm{Var}(T)\,. \tag{7.7}$$

The quantity $\langle ST\rangle$ is

$$\langle ST\rangle = \sum_y \frac{\partial_\lambda \left(p\left(v_y;\lambda\right)\right)}{p\left(v_y;\lambda\right)} T\left(v_y;\lambda\right) p\left(v_y;\lambda\right) = \partial_\lambda \sum_y p\left(v_y;\lambda\right) T\left(v_y;\lambda\right) = 1, \tag{7.8}$$

where it is assumed that the estimator T is unbiased i.e. $\langle T\rangle = \lambda$ and that $p(v, \lambda)$ is a well behaved function such that the interchange of summation and differentiation can be performed. Substituting Eqn. (7.8) into Eqn. (7.7) proves the CRB in Eqn. (7.4) for a single data sample. The CRB for parameter λ when using M samples $\{V^{(1)}, V^{(2)}, ..., V^{(M)}\}$ takes the form

$$M\,\mathrm{Var}(T) \geq \frac{1}{F(\lambda)}. \tag{7.9}$$

It is obtained by assuming that the samples are identically and independently distributed in which case the joint probability distribution is $p\left(v^{(1)}, v^{(2)}, ..., v^{(M)};\lambda\right) = \prod_{i=1}^{M} p\left(v^{(i)};\lambda\right)$ and the resulting FI for M samples is $MF(\lambda)$.

7.3.2 Multi-parameter Cramér-Rao bound

In the multi-parameter estimation formalism, T_i denotes the i^{th} estimator of parameter λ_i and the variance of a single estimator is replaced by the covariance matrix **Cov** of the estimators with elements $\text{Cov}_{ij} = \langle T_i T_j \rangle - \langle T_i \rangle \langle T_j \rangle$. For M data samples which is equivalent to M repetitions of the experiment, **Cov** is lower bounded by

$$M\mathbf{Cov} \geq (\mathbf{F})^{-1}, \tag{7.10}$$

where **F** is the Fisher information matrix with elements

$$F_{ij} = \sum_y \frac{\partial_{\lambda_i}(p_y)\,\partial_{\lambda_j}(p_y)}{p_y}. \tag{7.11}$$

Here p_y is a shorthand notation for $p\left(v_y;\boldsymbol{\lambda}\right)$ and therefore, the probability of y^{th} measurement outcome associated with the vector of parameters $\boldsymbol{\lambda}$.

The single-parameter CRB Eqn. (7.9) as well as the multi-parameter CRB Eqn. (7.10) are guaranteed to be asymptotically saturated by the maximum likelihood estimator.

7.4 Quantum Cramér-Rao bound

The quantum version of estimation theory begins with a quantum state $\hat{\rho}_\lambda$ which undergoes an evolution depending on $\boldsymbol{\lambda}$. The resulting state $\hat{\rho}_{\boldsymbol{\lambda}}$ is measured by a set of positive operator valued measures (POVMs) $\{\hat{\Pi}_y\}$ satisfying the completeness relation $\sum_y \hat{\Pi}_y = \hat{I}$, where $\hat{I}$ is the identity matrix. This leads to probabilities given by $p_y = \text{Tr}\left[\hat{\rho}_{\boldsymbol{\lambda}}\hat{\Pi}_y\right]$. All the information about the parameters $\boldsymbol{\lambda}$ is now encapsulated in the probability distribution p_y, and can be used to estimate the parameters with a precision given by the classical FI in Eqn. (7.11). However, the FI now also depends on the POVMs $\{\hat{\Pi}_y\}$, which stand in the way of obtaining a fundamental quantum limit to the covariance Cov($\boldsymbol{\lambda}$). The mathematical task is thus that of maximising the classical FI over all POVMs giving rise to the quantum Fisher information (QFI) – a distinguishability metric on the space of quantum states which quantifies the maximum amount of "information" about a parameter attainable by a given probe state [90, 93, 82]. Lower bounding the variance of an unbiased estimator with the inverse of the QFI is the so called quantum Cramér-Rao bound (QCRB). In the multi-parameter case, QCRB takes the form

$$M\mathbf{Cov} \geq (\mathbf{H})^{-1}, \tag{7.12}$$

where $\mathbf{H}$ is the QFI matrix with elements

$$H_{ij} = \mathrm{Re}[\mathrm{Tr}[\hat{\varrho}_{\boldsymbol{\lambda}} \hat{L}_i \hat{L}_j]]. \tag{7.13}$$

Here, Re is the real part and $\hat{L}_i$ denotes the symmetric logarithmic derivative (SLD) corresponding to parameter λ_i obeying

$$2\partial_{\lambda_i}\hat{\varrho}_{\boldsymbol{\lambda}} = \hat{L}_i\hat{\varrho}_{\boldsymbol{\lambda}} + \hat{\varrho}_{\boldsymbol{\lambda}}\hat{L}_i. \tag{7.14}$$

The elements of $\mathbf{H}$ can be written in terms of the eigenbasis of the density matrix $\hat{\varrho}_{\boldsymbol{\lambda}} = \sum_k E_k |e_k\rangle\langle e_k|$ with eigenvalues E_k and eigenvectors $|e_k\rangle$, leading to

$$H_{ij} = \mathrm{Re}\left[\sum_n \frac{\partial_{\lambda_i}(E_n)\partial_{\lambda_j}(E_n)}{E_n} + 4\sum_{n,m} E_m \frac{(E_n - E_m)^2}{(E_n + E_m)^2}\langle e_n|\partial_{\lambda_i} e_m\rangle\langle\partial_{\lambda_j} e_m|e_n\rangle\right]. \tag{7.15}$$

Therefore, calculating QFI requires diagonalising the density matrix which can be a challenging task for high rank matrices. See Appendix (A.1) for a derivation of Eqn. (7.15).

The QCRB in Eqn. (7.12) gives a tighter bound than the CRB in Eqn. (7.10) which means $M\mathbf{Cov} \geq (\mathbf{F})^{-1} \geq (\mathbf{H})^{-1}$ and therefore the QCRB provides the first step in understanding the fundamental limits of quantum enhanced metrology. Single parameter QCRB can in principle be always saturated. However, an additional saturability problem arises in the quantum multi-parameter estimation due to the possible non-commutativity of quantum measurements. If the optimal measurements corresponding to the different parameters do not commute, then there is not a common eigenbasis set out of which to construct the optimal POVM. This additional aspect of quantum multi-parameter estimation is what makes quantum metrology interesting. The lower bound on the precision set by the QCRB can not be always attained when we try to simultaneously gain knowledge about multiple parameters. The non-commutativity of measurements in quantum mechanics is of crucial importance for the work presented in this part of my thesis.

7.5 Multi-parameter quantum metrology applications

For equivalent resources, simultaneous quantum estimation of multiple phases or in general, parameters corresponding to non-commuting unitary generators, provides better precision than estimating them individually [11, 94]. This has generated interest in multi-parameter quantum metrology in a variety of scenarios and contexts [95, 96, 97, 98, 99, 100, 101]. However, the myriad motivations for studying multi-parameter quantum metrology are deeply interleaved and intertwined. Nevertheless, the following presents a broad delineation of at least three broad seams of interest:

1. *Physics*: The measurements that maximise the QFI corresponding to multiple parameters need not necessarily commute. Thus, the enhancements in precision metrology

promised by quantum mechanics might eventually be thwarted by quantum mechanics. It is of principal interest in quantum information theory as it explores the information extracting capabilities of quantum measurements, and provides a rich new testing bed for understanding the nature of quantum measurements in great generality. High precision estimation is also beginning to play a role in the detection of novel phenomena such as gravitational waves [86] and should lead to discoveries yet unknown in other areas of fundamental physics.

2. *Mathematics*: The quantum Fisher information matrix – the multi-parameter extension of the QFI – is a 'metric' on the space of quantum states. Although it is not unique as in the classical case, it is minimal among all monotone metrics [102]. This makes it not only a quantity of inherent interest in quantum metrology, but also capable of unlocking novel features of the space of quantum states whose study underlies all of quantum information theory, non-commutative geometry and quantum information geometry [103, 104, 105].

3. *Technology*: Numerous high level applications intrinsically involve multiple parameters. Quantum enhanced schemes for imaging [106], microscopy, spectroscopy to high precision sensors for classical electric, magnetic, gravitational fields cannot be developed without a clear understanding of multi-parameter quantum metrology. Eventually, highly precise characterisation of components for fault-tolerant quantum technologies [107] and quantum information science [108] might also benefit from multi-parameter quantum metrology.

Chapter 8

Joint estimation of phase and phase diffusion motivation

The central role of unitary evolution in quantum mechanics makes phase estimation a salient problem in precision metrology including the sensing of magnetic and electric fields, changes in refractive index, and measurements of time and displacements. This includes some of the most challenging tasks in physics such as gravitational wave detection [15, 14, 16] as well as highly desirable applications such as biological tracking and imaging [17]. Therefore, the understanding of the fundamental limits in the precision of phase estimation set by quantum mechanics is a worthwhile endeavour.

However, in real scenarios, phase estimation schemes are invariably affected by noise that results in the loss of quantum enhancement. This reverts quantum-enhanced scalings back down to that given by the shot noise limit [109, 110, 10]. Typical noise channels include particle loss and phase diffusion. Substantial effort has been invested in studying the effect of noise on phase estimation, both theoretically and experimentally in the case of loss [111, 112, 113, 114] as well as phase diffusion [115, 116, 117, 118]. The quantum limit (although in general not tight) on the phase estimation precision in the presence of diffusion has also been obtained using a variational approach [119].

Phase diffusion is a dissipationless noise channel that describes phase drifts within the measurement time due to interaction with the environment. Instead of being a nuisance, phase diffusion can, in fact, provide useful information about the physical system that the quantum probe interacts with. This has been labelled as decoherence microscopy [120] and has found numerous applications [121] including thermometry [122, 123, 124, 125], optomechanical temperature measurements within and beyond the linearised regime [26, 126], and fundamental physics [127]. Phase fluctuations between modes of an optical interferometer are inexorable, and can be caused by mechanical strains and thermal fluctuations inside an optical fiber [128, 129]. Phase diffusion also arises in matter-wave optics, particularly in confined geometries where its precise estimation can provide information on atom-atom interaction strength [130]. The precision of cold-atom accelerometers is limited by phase diffusion resulting from rotational fluctuations and gravitational forces, whose precise estimation might help alleviate their effect [131], or be used in precise measurement of physical constants [132]. At a more fundamental level, phase diffusion is a parameter of interest in gravitational decoherence models [133, 134, 135] and dark matter detection [136]. Moreover, in circumstances where these parameters vary in time, joint estimation scheme can provide more satisfactory results.

Numerous scenarios thus exist where a precise knowledge of phase diffusion in addition to the phase parameter can furnish a better understanding of the system under study. Schemes to estimate phase and phase diffusion simultaneously have been studied recently. Theoretical studies on the joint quantum-limited estimation of phase and phase diffusion using a quantum state comprised of a large number of qubits [137] have been undertaken, as well as experimental studies on single qubit systems [138, 139]. While this work deals with collective dephasing, models considering independent dephasing have also been studied in [140].

The central challenge of joint quantum-limited estimation schemes is the possible non-commutativity of measurements in quantum mechanics. As a result, the quantum limits may not always be attainable, even in principle. The joint estimation scenarios thus inevitably lead to trade-off relations in the attainable precision for the different parameters. Such trade-off relations tell us how much information can be gained about one parameter in the expense of the knowledge about the other parameters [4]. This is unlike the case for single parameter estimation, where the quantum-enhanced limit can always be attained [93, 82]. Gill and Massar derived a bound on the trade-off relation in the joint estimation of all the parameters characterising a quantum state of which one possesses many copies [141]. Their bound for mixed states is derived for measurements acting on a single copy of the state at a time. Recently, a symmetric measurement saturating the Gill-Massar bound was found [142]. This measurement is local and equally extracts optimal information about all the parameters, but applies to pure states only. It is important to stress that the Gill-Massar bounding strategy is only tight when the number of parameters is the same as the dimension of the Hilbert space in which the quantum state resides. Since this work considers the joint estimation of phase and phase diffusion – only two parameters – using a multi-dimensional quantum probe state, the Gill-Massar strategy is excessively lax for such purposes. New methods are therefore developed to seek tighter trade-off relations.

The main goal of the work presented in part III is to understand how this trade-off relation depends on the dimension of the state. Holland-Burnett (HB) [9] states form an apt example of FPN states for this purpose. The strategy for obtaining the trade-off relations for the simultaneous quantum-limited estimation of phase and phase diffusion applies to fixed-particle number

(FPN) states. It relies on a Taylor expansion of the full density matrix in the regimes of large and small diffusion. This leads to a tridiagonal density matrix and a low-rank density matrix in the large and small diffusion regimes respectively which enables their analytic diagonalisation. This overcomes the fundamental challenge for calculating the quantum Fisher information (QFI) for mixed quantum states analytically – their explicit diagonalisation. It is also important to stress that this method differs from strategies undertaken in other works, for instance [143] where the diffusion parameter is a constant independent of the dimension of the state. In this work, the validities of the approximations put some dependence between phase diffusion and the total number of particles. The main results are as follows:

1. In the large phase diffusion regime, for any FPN state, an analytically closed-form expression for the QFI matrix is provided. See Sec. (10.1.1).

2. In the large phase diffusion regime, for any FPN state, an analytically closed-form expression for the trade-off quantity

$$\mathrm{Tr}[\mathbf{F}\mathbf{H}^{-1}] = \frac{F_{11}}{H_{11}} + \frac{F_{22}}{H_{22}}, \tag{8.1}$$

   is provided. The maximum value of this quantity is 2, when both parameters are estimated with quantum-limited precision. This work shows that in the large diffusion regime, it is possible to attain the optimal trade-off relation of $\mathrm{Tr}[\mathbf{F}\mathbf{H}^{-1}] = 2$ for certain FPN states. It therefore follows that the globally optimal trade-off relation with respect to all diffusion values also approaches 2 for such states. HB states are an example of such states in the large particle number regime. See Sec. (10.1.2).

3. In the small phase diffusion regime, for any HB states, an analytically closed-form expression for the QFI matrix is provided. Most importantly, these states allow a quantum-

enhanced estimation of phase as well as phase diffusion. See Sec. (10.2.1).

4. In the regime of phase diffusion approaching zero, for HB states of small particle numbers, a numerical evidence is presented that the maximum value of $\mathrm{Tr}[\mathbf{F}\mathbf{H}^{-1}]$ approaches 1. This implies that, in the simultaneous estimation of phase and diffusion in this regime, when we estimate one parameter at the quantum-limit we gain no precision about the other parameter. See Sec. (10.2.2).

Chapter 9

Background

9.1 Probe system

This work considers joint estimation of two parameters, phase ϕ and collective phase diffusion Δ. The investigated system is shown in Fig. (9.1). The probe state is prepared in a pure FPN state with a total number of $2K$ particles. The mathematical representations of such a state and the special case of HB states are

$$|\psi_{FPN}\rangle = \sum_{n=0}^{2K} a_n |n, 2K-n\rangle \tag{9.1}$$

and

$$|\psi_{HB}\rangle = \sum_{n=0}^{2K} b_{\frac{n}{2}} \delta_{n,2q} |n, 2K-n\rangle \tag{9.2}$$

respectively, where $q \in \mathbb{Z}\{0 : K\}$. The normalised complex amplitudes, $a_n = |a_n|\mathrm{e}^{\mathrm{i}\theta_n}$, satisfy $\sum_{n=0}^{2K} |a_n|^2 = 1$ and $b_n = \sqrt{(2n)!(2K-2n)!}/\left(2^K n!(K-n)!\right)$ is a special case of a_n which takes non-zero values only for even terms.

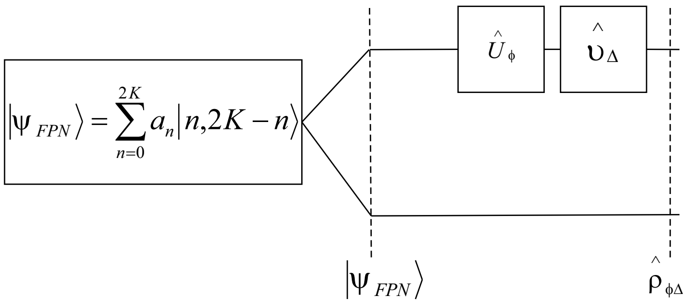

(a)

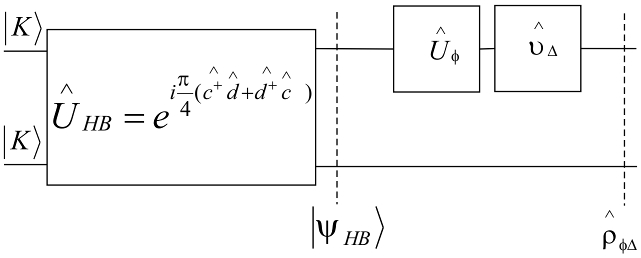

(b)

Figure 9.1: Schematic diagram of the investigated system **(a)** with a general FPN state – $\hat{\varrho}_{\phi\Delta}$ has the form of Eqn. (9.4) and **(b)** with the special case of HB states – $\hat{\varrho}_{\phi\Delta}$ has the form of Eqn. (9.5) or Eqn. (9.6). HB states are generated by acting with the unitary $\hat{U}_{HB}$ on two modes (associated with annihilation operators $\hat{c}$ and $\hat{d}$) containing equal number of particles K. In photonic systems, this corresponds to interfering two equal Fock states on a 50/50 beam splitter. It is also worth noting that $\hat{U}_\phi$ and $\hat{v}_\Delta$ commute and therefore the order in which phase shift and diffusion channel are applied is irrelevant.

The propagator of ϕ is a unitary transformation of the form $\hat{U}_\phi = \mathrm{e}^{\mathrm{i}\phi\hat{n}}$, where $\hat{n}$ is the number operator. The collective phase diffusion channel, $\hat{v}_\Delta$, is a random phase shift distributed according to a normal distribution of width Δ which acting on the probe state $\hat{\varrho}_{\mathrm{in}}$ gives

$$\hat{\varrho}_\Delta = \hat{v}_\Delta(\hat{\varrho}_{\mathrm{in}}) = \frac{1}{\sqrt{2\pi}\Delta}\int_{-\infty}^{+\infty} \mathrm{d}\epsilon\, \mathrm{e}^{-\frac{\epsilon^2}{2\Delta^2}}\, \hat{U}_\epsilon \hat{\varrho}_{\mathrm{in}} \hat{U}_\epsilon^\dagger. \tag{9.3}$$

Its effect is to exponentially erase the off-diagonal elements of the density matrix which also means reducing the information content about the parameters from the probe state.

The n^{th} component of the input FPN state acquires the phase term of $\mathrm{e}^{\mathrm{i}n\phi}$ and after passing through the phase diffusion channel, the overall state becomes mixed. The resulting density matrix is of the form,

$$\hat{\varrho} = \hat{\varrho}_{FPN} = \sum_{n,n'=0}^{2K} a_n a_{n'}^* \mathrm{e}^{\mathrm{i}\phi(n-n') - \frac{\Delta^2}{2}(n-n')^2} |n, 2K-n\rangle\langle n', 2K-n'|. \tag{9.4}$$

The particular instance of HB states can be written as

$$\hat{\varrho}_{HB} = \sum_{n,n'=0}^{2K} \delta_{n,2q}\delta_{n',2q'} b_{\frac{n}{2}} b_{\frac{n'}{2}} \mathrm{e}^{\mathrm{i}\phi(n-n') - \frac{\Delta^2}{2}(n-n')^2} |n, 2K-n\rangle\langle n', 2K-n'| \tag{9.5}$$

or equivalently

$$\hat{\varrho}_{HB} = \sum_{n,n'=0}^{K} b_n b_{n'} \mathrm{e}^{2\mathrm{i}\phi(n-n') - 2\Delta^2(n-n')^2} |2n, 2K-2n\rangle\langle 2n', 2K-2n'|, \tag{9.6}$$

where $\{q, q'\} \in \mathbb{Z}\{0 : K\}$.

9.2 Attaining the quantum limit

When solving the SLD equation, Eqn. (7.14), for a general evolved FPN state, $\hat{\varrho}$, it is useful to work in the basis that contains all the phase information, so that the resulting density matrix contains only real elements. This representation is given in Appendix (A.2). In this basis representation, $|\Gamma_{n,K,\phi,\theta}\rangle \equiv \mathrm{e}^{\mathrm{i}(\phi n + \theta_n)}|n, 2K-n\rangle$ where θ_n is the phase of each component of the input FPN state, the derivatives of $\hat{\varrho}$ with respect to ϕ and Δ are imaginary and real respectively. The SLD equation is a Lyapunov equation and since $\hat{\varrho}$ is a positive matrix, it has a unique continuous solution [144]

$$\hat{L}_i = 2\int_0^\infty \mathrm{d}t \mathrm{e}^{-\hat{\varrho}t} \partial_{\lambda_i} \hat{\varrho} \mathrm{e}^{-\hat{\varrho}t}, \tag{9.7}$$

where λ_i labels the different parameters and in our case, $i = 1$ and $i = 2$ correspond to ϕ and Δ respectively. From this form of the solution, we can conclude that $\hat{L}_1$ and $\hat{L}_2$ are imaginary and real respectively in the basis of $|\Gamma_{n,K,\phi,\theta}\rangle$. With this and using Hermiticity of SLDs, $\hat{L}_1$ and $\hat{L}_2$ can be expressed as,

$$\hat{L}_1 = \mathrm{i} \sum_{n,n'=0}^{2K} f_{n,n',\Delta} |\Gamma_{n,K,\phi,\theta}\rangle\langle\Gamma_{n',K,\phi,\theta}| \tag{9.8}$$

and

$$\hat{L}_2 = \sum_{n,n'=0}^{2K} g_{n,n',\Delta} |\Gamma_{n,K,\phi,\theta}\rangle\langle\Gamma_{n',K,\phi,\theta}|, \tag{9.9}$$

where $\{f_{n,n',\Delta}, g_{n,n',\Delta}\} \in \Re$, and $f_{n,n',\Delta} = -f_{n',n,\Delta}$ and $g_{n,n',\Delta} = g_{n',n,\Delta}$. Since all the phases can be absorbed in the basis and according to Eqn. (7.13), the QFI elements are basis independent, the whole QFI matrix is ϕ independent. Additionally, the off-diagonal elements of the QFI matrix are necessarily zero since trace of the product of two real matrices and one imaginary is imaginary as a result of which the real part is zero. Therefore, the QFI matrix for phase and phase diffusion for any input pure FPN state is of the form

$$\mathbf{H} = \begin{pmatrix} H_{11} & 0 \\ 0 & H_{22} \end{pmatrix}, \tag{9.10}$$

where subscripts 1 and 2 refer to ϕ and Δ, as noted earlier. H_{11} and H_{22} correspond to the maximum information content in the individual estimation of ϕ and Δ respectively. Obtaining a general closed-form of the quantum limits for this system is a difficult task because the evolved density matrix has the rank of $(2K+1)$ for FPN and $(K+1)$ for the special case of HB states, and the diagonalisation of such matrices is a challenging problem for arbitrary K. To obtain a better understanding, analytical expressions in the regimes of large and small phase diffusion are derived. For intermediate values of phase diffusion, a numerical approach is employed to solve for the SLDs and calculate the QFI (see Appendix (A.3)).

The limits on the covariance matrix set by the QFI are not necessarily attainable in multi-parameter estimation scenarios due to the possible non-commutativity of optimal measurements. A sufficient condition for saturating the QCRB is $[\hat{L}_1, \hat{L}_2] = 0$ which does not hold for a general FPN state or the special case of HB states. This implies that the optimal POVMs in the individual parameter estimation constructed from the eigenvectors of the SLDs do not commute in general and will not saturate the two-parameter QCRB. A weaker condition, which is sufficient and necessary, for saturating the multi-parameter QCRB is $\mathrm{Tr}\left[\hat{\varrho}\left[\hat{L}_1, \hat{L}_2\right]\right] = 0$. However, calculating this quantity numerically shows that it is non-zero for some fixed-particle number pure states. It is found to be zero for HB states for particle numbers up to 158, but this is also based on a numerical routine as opposed to an analytical proof. Additionally, to fullfil the multi-parameter saturability condition given by the expectation value of the commutator of the SLDs, it is necessary to consider multiple copies of the state and collective measurements. Although such strategy can bring further enhancements in the attainable joint precision [138, 140], it is harder to treat theoretically and implement experimentally [145]. Therefore, as a first step, this work is restricted to single copies of the state only. Additionally, the measurements are confined to a class of projective measurements as they optimise the FI of the associated probability distribution [141, 146].

The figure of merit considered in this work is the trace of the covariance matrix which for our two parameter case, ϕ and Δ, is minimised when the off-diagonal elements of the FI matrix are zero. We can therefore compute how close the minimum variances of the estimators for phase and phase diffusion parameters ($\mathrm{Var}_{\mathrm{min}}(\phi)$ and $\mathrm{Var}_{\mathrm{min}}(\Delta)$ respectively) associated with a given measurement compare with the QCRB by considering the ratios of the corresponding diagonal elements of the FI and QFI matrices. This is given by

$$\mathrm{Tr}[\mathbf{FH}^{-1}] = \frac{F_{11}}{H_{11}} + \frac{F_{22}}{H_{22}} = \frac{H_{11}^{-1}}{M\mathrm{Var}_{\min}(\phi)} + \frac{H_{22}^{-1}}{M\mathrm{Var}_{\min}(\Delta)} \tag{9.11}$$

which is the bound studied in this work. The higher the bound, the higher precision we can attain about the two parameters simultaneously. Its upper limit is set by the QCRB which in the case of our two-parameter estimation problem gives $\mathrm{Tr}[\mathbf{FH}^{-1}] \leq 2$. This quantity has been considered in previous works such as [141, 138, 142].

The optimal bound $\mathrm{Tr}\left[\mathbf{FH}^{-1}\right]_{\max}$ with respect to all projective measurements, similarly to the QFI, is ϕ insensitive. The reason is the following: the phase dependence of the bound arises because the input state $\hat{\varrho}_{in}$ acquires phase in the unitary transformation $\hat{U}_\phi = \mathrm{e}^{\mathrm{i}\phi\hat{n}}$. If some optimal value of phase which maximises the bound in Eqn. (9.11) is changed by an amount ζ due to a unitary transformation $\hat{U}_\zeta = \mathrm{e}^{\mathrm{i}\zeta\hat{n}}$ we can always reverse the action of this unitary by applying $\hat{U}_\zeta^{-1}$ in our optimal measurement. As a result, the optimal bounds depend only on the particle number and the phase diffusion parameter.

Though highly desirable, the maximisation of $\mathrm{Tr}[\mathbf{FH}^{-1}]$ over all projective measurements is in general exigent. This is partially due to the lack of knowledge of the closed form of the QFI for a general phase diffusion parameter and particle number, and partially due to the need to optimise over a complex space containing $2d-2$ parameters, where d is the dimension of the Hilbert space of the input probe state, factor of two accounts for the fact that we have real and imaginary parameters and subtraction of two accounts for normalisation and global phase. This work therefore, explores this aspect analytically in the regime of large (for a general FPN state) and small (for the special case of HB states) Δ, and provides numerical results for the general Δ regime (for HB states).

Chapter 10

Results for different diffusion regimes

10.1 Large diffusion regime

The off-diagonal elements of the FPN density matrix in Eqn. (9.4) decay exponentially in Δ. If Δ is sufficiently large, we can neglect all the off-diagonals except for the one (k^{th} off-diagonal) that is closest to the main diagonal and contributes non-zero elements. This approximation corresponds to Taylor expansion of $\hat{\varrho}$ to the order of $2k^2$ in $x = \mathrm{e}^{-\Delta^2/4}$ about $x = 0$ which results in the approximate, tridiagonal density matrix,

$$\hat{\varrho}_{\mathrm{L}\Delta} = \sum_{n,n'=0}^{2K} a_n a_{n'}^* \mathrm{e}^{\mathrm{i}\phi(n-n')} x^{2(n-n')^2} (\delta_{n,n'} + \delta_{n,n'\pm k}) |n, 2K-n\rangle\langle n', 2K-n'|, \tag{10.1}$$

where subscript LΔ identifies the large phase diffusion approximation. The case of $k = 1$ corresponds to an FPN state, where the first off-diagonal contributes non-zero elements and this is the last off-diagonal of the density matrix that we keep. The instance of $k = 2$ corresponds to a state, where the first off-diagonal has all zero elements and the second off-diagonal contributes non-zero elements, and therefore this is the last one that we keep. HB states are a good

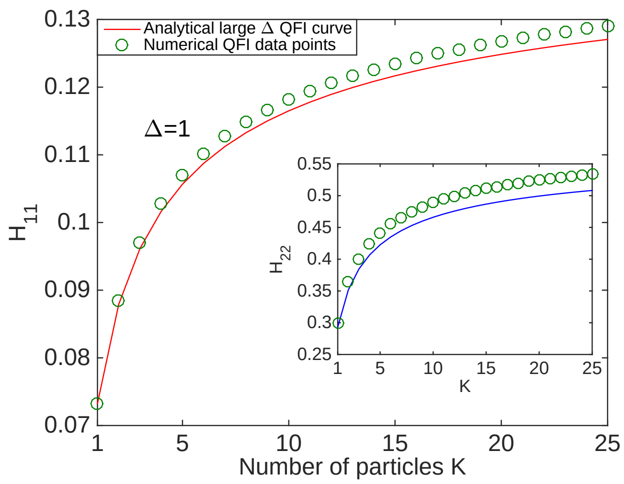

Figure 10.1: Diagonal QFI matrix elements as a function of K for HB states in the large phase diffusion approximation. K is the particle number in each of the two input modes of the unitary generating the HB state (see Fig. (9.1)). Both H_{11} and H_{22} are increasing functions of K as expected from Eqn. (10.4) and Eqn. (10.5). The accuracy of the analytical expressions gets worse as K increases which is expected from the validity constraint in Eqn. (10.3). In general, the approximation for H_{22} is less accurate than for H_{11} due to the factor of Δ^2 appearing in Eqn. (10.5) as explained in the main text.

example of the $k = 2$ case, where in fact only even numbered off-diagonals contribute non-zero elements. Also, in the case of HB states, $a_n = b_{\frac{n}{2}} \delta_{n,2q}$ as defined in Eqn. (9.2). The approximation in Eqn. (10.1) is valid when

$$\Delta^{(FPN)} \geq \sqrt{\frac{2}{(k+1)^2} \ln\left(\frac{2K}{f}\right)} \tag{10.2}$$

and

$$\Delta^{(HB)} \geq \sqrt{\frac{1}{8} \ln\left(\frac{K}{f}\right)} \tag{10.3}$$

for a general FPN and the special case of HB states respectively, where f is the allowed relative error on the density matrix (see Appendix (A.4) for details). This shows the $\sqrt{\ln(K)}$ dependence on the threshold value of Δ for the desired relative error.

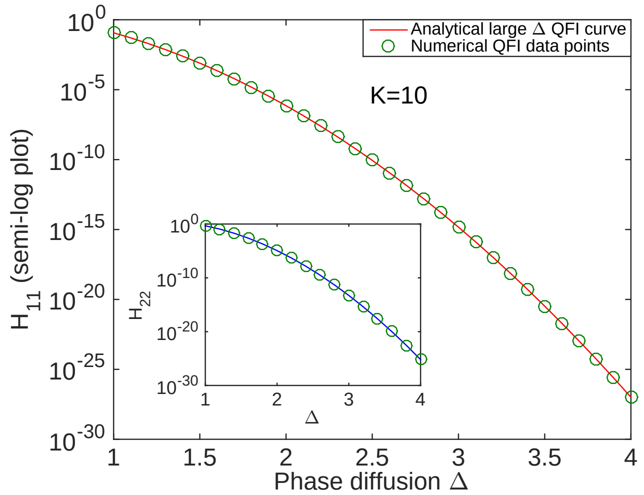

Figure 10.2: Semi-log plot of the diagonal QFI matrix elements as a function of Δ for HB states in the large phase diffusion approximation. H_{11} and H_{22} show an exponential decrease with respect to Δ as expected due to the exponential erasing of the off-diagonal elements of the density matrix. We present the y-axis on the logarithmic scale to show that the QFI elements go to zero at large Δ. A complementary, linear plot of the QFI as a function of Δ is shown in Fig. (A.3) of Appendix (A.7) which magnifies the calculation error at smaller phase diffusion values. The analytical approximations show a good agreement with the numerical data. At $K = 25$ and $\Delta = 1$, the relative error of the analytical values with respect to the numerical values of H_{11} and H_{22} are 1.6% and 4.9% respectively. This behaviour improves at larger Δ values and at $K = 25$ and $\Delta = 1.2$, the relative errors reduce to 0.3% for H_{11} and 0.9% for H_{22}.

10.1.1 Quantum limit

In order to gain an intuition for the form of the SLDs in the large Δ approximation, the SLD equation described in Eqn. (7.14) can be solved for small values of K. This gives us an ansatz for the SLDs for ϕ and Δ, $\hat{L}_{1,\mathrm{L}\Delta}$ and $\hat{L}_{2,\mathrm{L}\Delta}$ respectively, shown in Eqn. (A.25) and Eqn. (A.26) of Appendix (A.5). The SLDs are accurate to the order of x^{2k^2} which can be proven by substituting them into the left and right hand sides of the SLD equation to verify that the equality holds within the approximation. This is shown in Appendix (A.5). It is worth noting that the presence of the factor of Δ in $\hat{L}_{2,\mathrm{L}\Delta}$ decreases its order of accuracy from x^{2k^2} to $x^{2k^2-4\Delta^{-2}\ln(\Delta)}$.

The resulting QFI elements, $H_{11,\mathrm{L}\Delta}$ and $H_{22,\mathrm{L}\Delta}$, are given by

$$H_{11,\mathrm{L}\Delta} = 4k^2 x^{4k^2} \sum_{n=k}^{2K} \frac{|a_n|^2 |a_{n-k}|^2}{|a_n|^2 + |a_{n-k}|^2}, \tag{10.4}$$

$$H_{22,\mathrm{L}\Delta} = 4k^4 \Delta^2 x^{4k^2} \sum_{n=k}^{2K} \frac{|a_n|^2 |a_{n-k}|^2}{|a_n|^2 + |a_{n-k}|^2}, \tag{10.5}$$

where the sums above are upper-bounded by 1/2 (see Appendix (A.6)). For HB states, this can be attained in the regime of large K. This upper bound implies the loss of quantum enhancement in the large phase diffusion regime as at some point increasing the particle number in the input probe state will have no influence on the precision of our estimation scheme. The exponential decrease of $H_{11,\mathrm{L}\Delta}$ and $H_{22,\mathrm{L}\Delta}$ with respect to Δ is to be expected since the effect of phase diffusion is to exponentially erase the off-diagonal elements of the density matrix. Again, the accuracy of $H_{22,\mathrm{L}\Delta}$ is decreased from x^{4k^2} to $x^{4k^2-4\Delta^{-2}\ln(\Delta^2)}$ due to the presence of the Δ^2 factor. The calculation of the $H_{11,\mathrm{L}\Delta}$ term is shown in Appendix (A.6).

The analytical quantum limits given in Eqn. (10.4) and Eqn. (10.5) are compared with the values obtained using a numerical routine developed in MATLAB (see Appendix (A.3)) for HB states. The resulting curves are shown in Fig. (10.1) and Fig. (10.2). Further, we provide a numerical phase diffusion validity plot in Fig. (A.1) of Appendix (A.4), also for HB states. The plot shows the threshold values of Δ for which the approximation is valid as a function of particle number (K) when the maximum allowed relative error ($\delta H_{ii}/H_{ii}$) is 0.05.

10.1.2 Trade-off relation

To find the maximal joint information bound for our problem, we are required to maximise $\mathrm{Tr}\left[\mathbf{F}\mathbf{H}^{-1}\right]$ with respect to all projective measurements $|v_y\rangle = \sum_{n=0}^{2K} r_{y,n} \mathrm{e}^{\mathrm{i}X_{y,n}} |n, 2K-n\rangle$ which form a POVM set $\{|v_y\rangle\langle v_y|\}$ for the considered Hilbert space. Such optimisation is shown in Appendix (A.8) in the large Δ regime. For any FPN state with coefficients $a_n = |a_n|e^{i\theta_n}$, the phase $X_{y,n}$ of the optimal projectors must satisfy

$$X_{y,n} = X_{y,n-k-1} - 2X_{y,n-k} - \theta_{n-k-1} + 2\theta_{n-k} - \theta_n. \tag{10.6}$$

Additionally, we assume that the magnitudes $r_{y,n}$ of the optimal projectors are equally weighted which gives

$$r_{y,n} = \frac{1}{\sqrt{\frac{2K}{k}+1}}. \tag{10.7}$$

This last choice in Eqn. (10.7) is motivated by the results from the simulated annealing algorithm which searches through the space of projective measurements to maximise the bound for HB states. The numerics is performed in the small particle number regime and shows that the bound becomes Δ independent for large values of Δ (see Fig. (10.8) of Sec. (10.3)). The associated optimal projectors have the structure as given by Eqn. (10.6) and Eqn. (10.7). The resulting bound, $\mathrm{Tr}[\mathbf{FH}^{-1}]$, in the simultaneous estimation of ϕ and Δ in the large phase diffusion regime is

$$\mathrm{Tr}[\mathbf{FH}^{-1}] = \frac{\left(\sum_{n=k}^{2K} |a_n||a_{n-k}|\right)^2}{\sum_{n=k}^{2K} \frac{|a_n|^2|a_{n-k}|^2}{|a_n|^2+|a_{n-k}|^2}}. \tag{10.8}$$

See Appendix (A.8) for derivation. This bound reaches the QCRB for two-parameter estimation, i.e. $\mathrm{Tr}\left[\mathbf{FH}^{-1}\right] = 2$, when $|a_n| = |a_{n-k}|$ for $n \in \mathbb{Z}\{k : 2K\}$. This shows that the globally optimal bound with respect to all diffusion values will also approach the QCRB for such states. For HB states, the condition $|a_n| = |a_{n-k}|$ coincides with the large particle number (K) regime. Plot of the bound in Eqn. (10.8) as a function of K in the case of HB states is shown in Fig. (10.3). The inlay plot shows the asymptotic attainability of the QCRB at large K, whereas the main plot shows the comparison with the numerical optimization routine based on the simulated

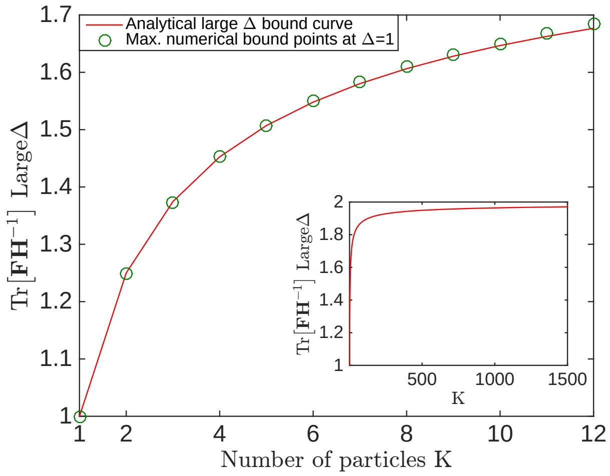

Figure 10.3: Joint information bound in estimating ϕ and Δ simultaneously as a function of K for HB states in the large phase diffusion regime. The main plot compares the analytical bound in Eqn. (10.8) with the optimal bound at $\Delta = 1$ found using the simulated annealing algorithm. The two methods show a good agreement which suggests that the POVM defined in Eqn. (10.7) and Eqn. (10.6) is indeed optimal in the special case of HB states for the investigated small K regime. The inlay plot displays the analytical bound for a higher range of K values in the case of HB states. It shows that the bound approaches the upper limit of 2 set by the QCRB for large K. At $K = 1500$, the analytical bound is 1.97.

annealing algorithm. At large values of Δ, the analytical bound in Eqn. (10.8), obtained using the POVM defined in Eqn. (10.6) and Eqn. (10.7), provides a good agreement with the numerical data in the case of HB states. However, an analytical proof of the optimality of this POVM for a general FPN state in the large phase diffusion regime remains an open question.

10.2 Small diffusion regime

The analysis for the small phase diffusion regime is restricted to the special case of HB states. In this regime, the HB density matrix in Eqn. (9.6) is Taylor-expanded to the second order in Δ for H_{11} and to the fourth order in Δ for H_{22} near $\Delta = 0$. The reason for the fourth order Taylor expansion in Δ in the case of H_{22} is to ensure that the corresponding SLD equation, $2\partial_\Delta\hat{\varrho} = \hat{L}_2\hat{\varrho} + \hat{\varrho}\hat{L}_2$, is accurate to at least second order in Δ as we lose one order in Δ on the left hand side due to the differentiation with respect to Δ.

The Taylor-expanded forms of the evolved HB density matrix to the second and fourth order in Δ are respectively

$$\hat{\varrho}_{1,\mathrm{S}\Delta} = \sum_{n,n'=0}^{K} b_n b_{n'} \mathrm{e}^{2\mathrm{i}\phi(n-n')}(1-2\Delta^2(n-n')^2)|2n, 2K-2n\rangle\langle 2n', 2K-2n'| \tag{10.9}$$

and

$$\hat{\varrho}_{2,\mathrm{S}\Delta} = \sum_{n,n'=0}^{K} b_n b_{n'} \mathrm{e}^{2\mathrm{i}\phi(n-n')}(1-2\Delta^2(n-n')^2+2\Delta^4(n-n')^4)|2n, 2K-2n\rangle\langle 2n', 2K-2n'|, \tag{10.10}$$

where subscript SΔ identifies the small phase diffusion approximation. The validity of the approximation is evaluated by comparing the last kept non-zero term with the first neglected non-zero term. When expressing $\hat{\varrho}$ as $\hat{\varrho}_{1,\mathrm{S}\Delta}$, the approximation made is $\Delta^2 \ll 1/\left(n-n'\right)^2$. This inequality can be further tightened by taking $\left(n-n'\right) = K$ which gives

$$\Delta^2 \ll \frac{1}{K^2}. \tag{10.11}$$

The equivalent validity constraint can be derived for $\hat{\varrho}_{2,\mathrm{S}\Delta}$ which has the same form as Eqn. (10.11) but with an extra factor of $3/2$ in front.

Expanding Eqn. (10.9) and Eqn. (10.10), we get a set ($\mathcal{W}_1$) of 3 linearly independent vectors describing $\hat{\varrho}_{1,\mathrm{S}\Delta}$ and a set ($\mathcal{W}_2$) of 5 linearly independent vectors describing $\hat{\varrho}_{2,\mathrm{S}\Delta}$. The elements of sets $\mathcal{W}_1$ and $\mathcal{W}_2$ are defined as follow,

$$\mathcal{W}_1 = \{|w_1\rangle\ , |w_2\rangle, |w_3\rangle\} \tag{10.12}$$

and

$$\mathcal{W}_2 = \{|w_1\rangle\ , |w_2\rangle, |w_3\rangle, |w_4\rangle\ , |w_5\rangle\} \tag{10.13}$$

where $|w_k\rangle = \sum_{n=0}^{K} n^{k-1}|\varphi_n\rangle$ with $|\varphi_n\rangle = b_n \mathrm{e}^{2\mathrm{i}\phi n}|2n, 2K-2n\rangle$. See Appendix (A.9) for the proof of linear independence of the elements of sets $\mathcal{W}_1$ and $\mathcal{W}_2$. Since $\hat{\varrho}_{1,\mathrm{S}\Delta}$ and $\hat{\varrho}_{2,\mathrm{S}\Delta}$ are spanned by 3 and 5 linearly independent vectors respectively, they can be expressed as 3×3 and 5×5 dimensional matrices if an appropriate orthonormal basis set is chosen. This is crucial since it overcomes the problem of diagonalising a $(K+1)$ dimensional matrix. The orthonormal sets can be found by orthonormalising the vectors $\{|w_1\rangle, |w_2\rangle, ..., |w_5\rangle\}$ using the Gram-Schmidt procedure and they are denoted by $\mathcal{V}_1 = \{|v_1\rangle, |v_2\rangle, |v_3\rangle\}$ and $\mathcal{V}_2 = \{|v_1\rangle, |v_2\rangle, |v_3\rangle, |v_4\rangle, |v_5\rangle\}$ for $\hat{\varrho}_{1,\mathrm{S}\Delta}$ and $\hat{\varrho}_{2,\mathrm{S}\Delta}$ respectively. The Gram-Schmidt procedure and its results are shown in Appendix (A.10). Given $\mathcal{V}_1$ and $\mathcal{V}_2$, we can now perform the basis change of $\hat{\varrho}_{1,\mathrm{S}\Delta}$ and $\hat{\varrho}_{2,\mathrm{S}\Delta}$ by applying

$$\hat{\varrho}' = \sum_{i,j=0}^{N} \mathrm{Tr}\left[|v_j\rangle\langle v_i|\hat{\varrho}\right]|v_i\rangle\langle v_j|, \tag{10.14}$$

where N is the number of basis vectors forming a complete set. The resulting 3×3 and 5×5 density matrices, written in the basis $\mathcal{V}_1$ and $\mathcal{V}_2$, are

$$\hat{\varrho}'_{1,\mathrm{S}\Delta} = \begin{pmatrix} b_{11} & 0 & b_{13} \\ 0 & b_{22} & 0 \\ b_{13} & 0 & 0 \end{pmatrix} \tag{10.15}$$

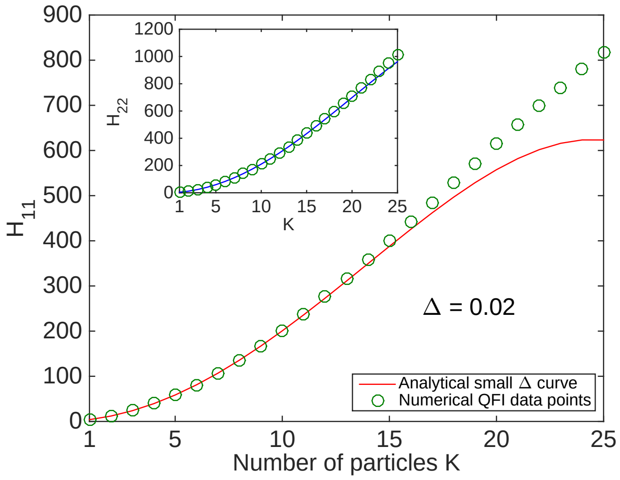

Figure 10.4: Diagonal QFI matrix elements as a function of K for HB states in the small phase diffusion approximation. As expected, H_{11} and H_{22} are increasing functions of K showing the approximate Heisenberg scaling of K^2. The approximation becomes worse at larger K values for a given Δ as expected from the validity constraints in Eqn. (10.11). In general, H_{22} is more accurate than H_{11} because in this case the density matrix of the probe state is Taylor expanded to the fourth order in Δ rather than second order in Δ.

and

$$\hat{\varrho}'_{2,\mathrm{S}\Delta} = \begin{pmatrix} c_{11} & 0 & c_{13} & 0 & c_{15} \\ 0 & c_{22} & 0 & c_{24} & 0 \\ c_{13} & 0 & c_{33} & 0 & 0 \\ 0 & c_{24} & 0 & 0 & 0 \\ c_{15} & 0 & 0 & 0 & 0 \end{pmatrix}, \tag{10.16}$$

where $b_{ij} \in \Re$ and $c_{ij} \in \Re$ and these matrix elements are functions of K and Δ only. The exact forms of the entries in terms of K and Δ are given in Appendix (A.11). It is worth noting that the reduced matrix elements have no ϕ dependence, whereas the orthonormal basis vectors defining these matrices have no Δ dependence.

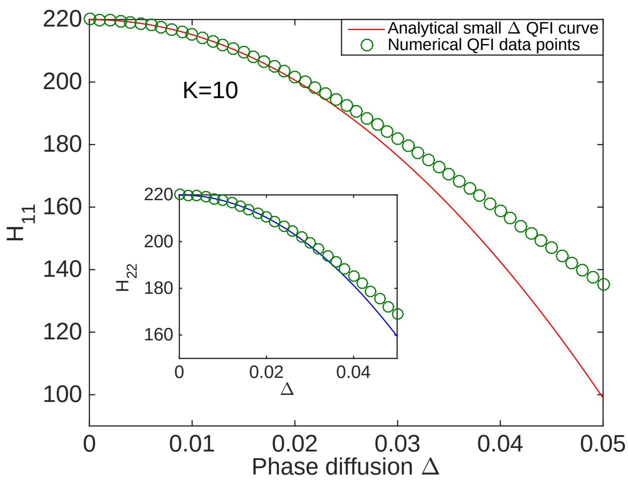

Figure 10.5: Diagonal QFI matrix elements as a function of Δ for HB states in the small phase diffusion approximation. Both H_{11} and H_{22} are decreasing functions of Δ in this regime. For a given value of K the approximation gets worse at larger Δ which agrees with the validity constraints in Eqn. (10.11). At $K = 20$ and $\Delta = 0.02$, the relative error of the analytical values with respect to the numerical values of H_{11} and H_{22} are 9% and 2% respectively. The accuracy improves at smaller Δ values and at $K = 20$ and $\Delta = 0.018$, the relative errors reduce to 6% for H_{11} and 1% for H_{22}.

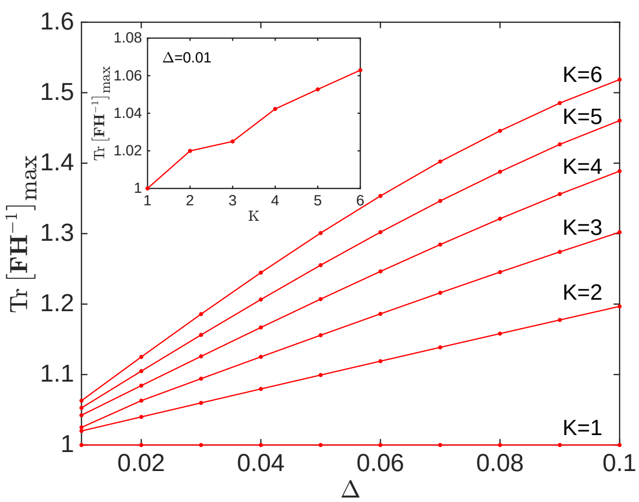

Figure 10.6: Bound on the joint estimation of phase and diffusion for HB states, numerically optimised with respect to orthonormal proejctive measurements. K labels different particle numbers. The main plot shows that the bound $\mathrm{Tr}\left[\mathbf{FH}^{-1}\right]$ as $\Delta \to 0$ for the considered K values. The inlay plot shows the optimal bound as a function of K for the smallest sampled Δ of 0.01.

10.2.1 Quantum limit

Diagonalisation of matrices in Eqn. (10.15) and Eqn. (10.16) is greatly simplified due to their sparse structure. In particular, $\hat{\varrho}'_{1,\mathrm{S}\Delta}$ can be expressed as a direct sum of 2×2 and 1×1 matrices, whereas $\hat{\varrho}'_{2,\mathrm{S}\Delta}$ as a direct sum of 3×3 and 2×2 matrices. The diagonalisation of these matrices reveals that one of the eigenvalues of $\hat{\varrho}'_{1,\mathrm{S}\Delta}$ and two eigenvalues of $\hat{\varrho}'_{2,\mathrm{S}\Delta}$ are negative up to the order of Δ^4 and Δ^6 respectively. Therefore, they are zero within our small phase diffusion approximation and they do not contribute towards reconstructing our Taylor expanded density matrices. Consequently, $\hat{\varrho}'_{1,\mathrm{S}\Delta}$ is a rank 2 matrix and $\hat{\varrho}'_{2,\mathrm{S}\Delta}$ rank 3 matrix within the small phase diffusion approximation. See Appendix (A.11) for details of the diagonalisation procedure and the results. The alternative form of the QFI expression in terms of the eigenbasis of the density matrix, given in Eqn. (7.15), can be used to find H_{11} and H_{22} within the small phase diffusion approximation. The resulting diagonal QFI matrix elements (when keeping second order in Δ terms only) corresponding to the HB probe state are

$$H_{11,\mathrm{S}\Delta} = 2K(K+1) - (2K(K+1))^2\Delta^2, \tag{10.17}$$

and

$$H_{22,\mathrm{S}\Delta} = 2K(K+1) - \frac{1}{2}(2K(K+1))^2\Delta^2. \tag{10.18}$$

The first of these expressions shows that the presence of phase diffusion diminishes the precision attainable in the estimation of phase. This has been anticipated before [10, 115, 116, 117, 138], but we now provide an exact expression for HB states. The second expression shows that it is possible to achieve a quantum-enhanced estimation of the phase diffusion parameter. This is because the QFI for Δ scales quadratically with K, while any classical strategy with K

particles will only lead to a QFI scaling at most linearly in K. Figures (10.4) and (10.5) show the comparison of the obtained analytical expressions in Eqn. (10.17) and Eqn. (10.18) with the numerical data points. Additionally, numerical phase diffusion validity plot for this approximation is shown in Fig. (A.4) of Appendix (A.11).

10.2.2 Trade-off relation

The trade-off relation in the limit of $\Delta \to 0$ for an arbitrary POVM set $\{\pi_y\}$ composed of projectors $|v_y\rangle = \sum_{n=0}^{K} r_{y,n} \mathrm{e}^{\mathrm{i}X_{y,n}} |2n, 2K-2n\rangle$ is

$$\mathrm{Tr}\left[\mathbf{FH}^{-1}\right] = \frac{2}{K(K+1)} \times \sum_{y=0}^{K} \frac{\left(\sum_{n,n'=0}^{K} R_{y,n,n'} \sin\left(\Theta_{y,n,n'}\right)\left(n-n'\right)\right)^2 + 4\Delta^2\left(\sum_{n,n'=0}^{K} R_{y,n,n'} \cos\left(\Theta_{y,n,n'}\right)\left(n-n'\right)^2\right)^2}{\sum_{n,n'=0}^{K} R_{y,n,n'} \cos\left(\Theta_{y,n,n'}\right)}, \tag{10.19}$$

where $\Theta_{y,n,n'} = \left(X_{y,n'} - X_{y,n} + 2\phi(n-n')\right)$ and $R_{y,n,n'} = r_{y,n} r_{y,n'} b_n b_{n'}$. The term independent of Δ corresponds to F_{11}/H_{11}, whereas the remaining term containing the factor of Δ^2 corresponds to F_{22}/H_{22}. Details of the derivation are given in Appendix (A.12). Equation (10.19) shows that in the regime of $\Delta \to 0$, to attain high precision about Δ, we require some Δ dependence in the POVM to reduce the effect of the Δ^2 factor appearing in the F_{22} term. Without knowing this further structure of the optimal POVM, standard maximisation seems to be a challenging task.

To gain some intuition of what the trade-off relation might be as $\Delta \to 0$, numerical results based on a simulated annealing algorithm are presented in the small particle number regime. The results suggest that the bound in the joint estimation of phase and phase diffusion using HB states approaches 1 as Δ approaches 0. Figure (10.6) shows this tendency with the smallest

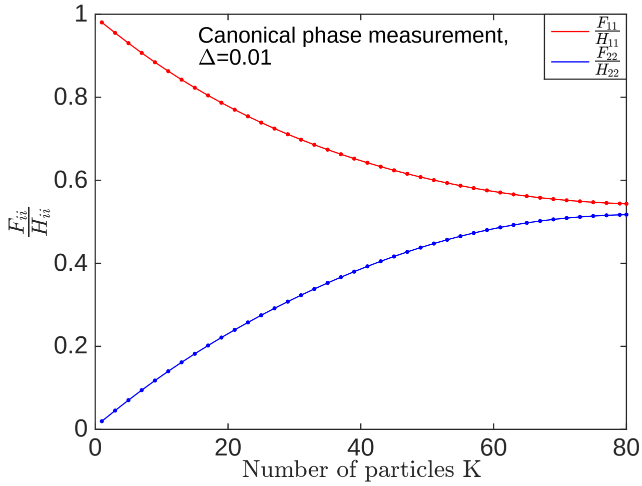

Figure 10.7: Numerical results with the canonical phase measurement POVM at $\Delta = 0.01$. In the high particle number regime (considered within the simulation), the POVM gives significant information about both phase and diffusion with the total trade-off $\mathrm{Tr}\left[\mathbf{F}\mathbf{H}^{-1}\right]$ of approximately 1.06.

sampled Δ of 0.01.

Although the diagonal elements of the QFI matrix (H_{11} and H_{22}) reach maximum at $\Delta = 0$, the above mentioned numerical results (performed for small particle numbers) suggest that the opposite is the case for the joint information bound. As an example, we consider the canonical phase measurement POVM [19, 20], corresponding to a projection onto the phase state $|\psi\rangle = \sum_{n=0}^{\infty} \mathrm{e}^{\mathrm{i}ny}|n\rangle$, which for our two-mode HB probe state has the form,

$$|v_y\rangle = \frac{1}{\sqrt{2\pi}} \sum_{n=0}^{K} \mathrm{e}^{\mathrm{i}ny}|n, 2K - n\rangle. \tag{10.20}$$

This POVM was suggested in Ref. [137] as an optimal measurement for estimating both phase and diffusion in the large particle number regime using the cosine state.

The canonical phase measurement has no Δ dependence and therefore for our scheme, according to Eqn. (10.19), the FI of the diffusion parameter gets vanishingly small as $\Delta \to 0$.

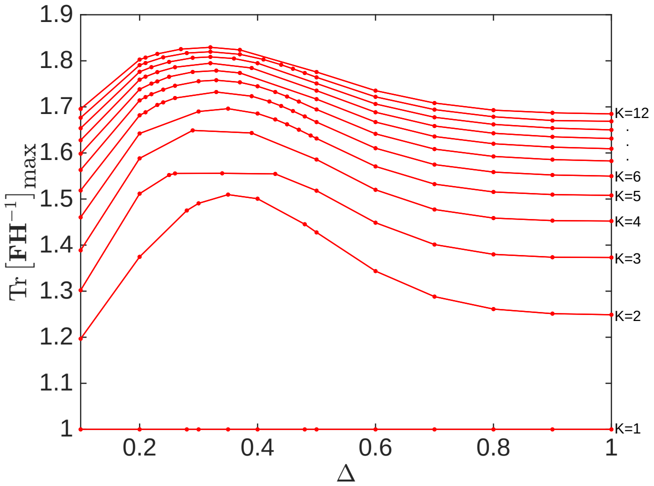

Figure 10.8: Numerical optimal join information bound for HB probe states for different Δ and K values obtained using the simulated annealing search algorithm. The bound peaks at some intermediate diffusion value (between 0.3 and 0.4) for the considered particle numbers.

However, it is still possible to extract some information about Δ using this POVM if Δ is not too small. We numerically simulate the performance of this measurement in our estimation scheme for $\Delta = 0.01$ and particle number (K) regime between 1 and 80. The results presented in Fig. (10.7) show that in the high particle number regime (considered within the simulation), we can extract significant information about both ϕ and Δ.

10.3 Trade-off for intermediate diffusion

The analytical understanding of the trade-off (valid for arbitrary Δ values) in the joint estimation of phase and diffusion for a general FPN state and in the special case of HB states remains an open question. However, the large diffusion analysis shows that for FPN states with equally weighted magnitudes the joint information bound approaches 2 which is the upper bound set by the QCRB. For HB states, this corresponds to the large particle number regime. Since this is true in the large diffusion regime and $\mathrm{Tr}\left[\mathbf{FH}^{-1}\right] \leq 2$ then it has to also apply to the globally

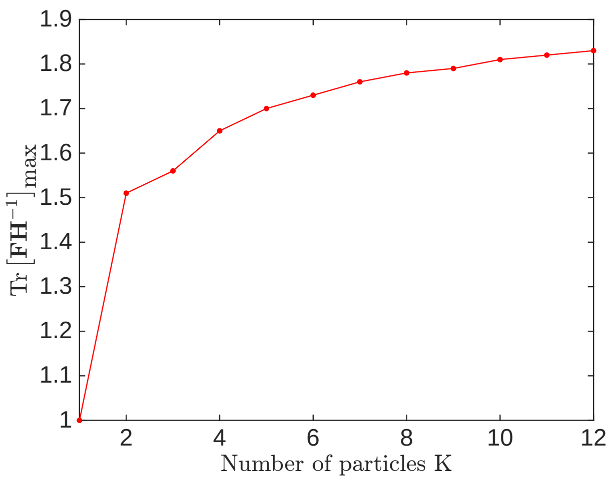

Figure 10.9: Globally maximal joint information bound with respect to all Δ values plotted as a function of K for HB states.

maximal bound across all diffusion values for such states.

Simulated annealing algorithm was used to perform a numerical search on the space of projective measurements to maximise the joint information bound at a given Δ and K values in the case of HB states. The results are shown in Fig. (10.8) and Fig. (10.9). The bound peaks at intermediate values of Δ (between 0.3 and 0.4) for the considered K values. As K increases, the numerics suggests that this maximal bound also increases but at a decreasing rate for higher K values. As explained at the beginning of this section, we expect this maximal bound to reach the upper limit of 2 set by the QCRB.

10.4 Summary

In any physical system, noise processes are always present and to be able to include them in the estimation schemes is an important step towards real-life, robust metrology. In fact, in many circumstances, noise itself may be the parameter that we require to gain the knowledge of. This brings us to the situation, where the simultaneous estimation of unitary and non-unitary parameters is of interest. The presence of non-unitary parameters (noise) typically makes the analysis of the system much harder since one has to deal with mixed states as opposed to pure states.

In this work, the problem of quantum-limited joint estimation of phase and collective dephasing was studied in the framework of QCRB using FPN states. The QFI for this system is a diagonal matrix whose elements are derived in the regimes of large (for a general FPN state) and small (for the special case of HB states) diffusion by performing Taylor expansion of the evolved density matrix in the appropriate limits. The results are shown in Eqn. (10.4), Eqn. (10.5), Eqn. (10.17) and Eqn. (10.18).

One of the goals of this research was to answer how closely the precision promised by the QFI can be attained when one tries to estimate phase and diffusion simultaneously by performing projective measurements acting on a single copy of the state. Of particular interest was to understand how this attainability is affected by the dimension of the state which in the instance of HB states is equal to $(K+1)$. Although the QFI is attainable in the individual estimation of parameters [4], it is not necessarily so in the joint estimation schemes due to the possible non-compatibility of optimal measurements. This gives rise to bounds quantifying how much information can be gained about one parameter in the expense of the knowledge about the other parameters. Such bounds are of fundamental importance in quantum mechanics and therefore worth pursuing. They were studied in previous works for different schemes [138, 141, 142] and defined by $\mathrm{Tr}\left[\mathbf{F}\mathbf{H}^{-1}\right]$. In general, the QFI as well as the optimal bound are phase independent.

The analytical joint information bound for phase and collective diffusion is derived in the large diffusion regime (for a general FPN state) by assuming the optimal POVM to be composed of projectors with components of equally weighted magnitudes. The choice of this POVM was motivated by the results from the simulated annealing algorithm which searched through the space of projective measurements to maximise the bound for the special case of HB states. The POVM and the associated bound are shown in Eqn. (10.6), Eqn. (10.7) and Eqn. (10.8).

The analytical bound in the small phase diffusion regime is more difficult to derive due to the more complex structure of the optimal POVM. The results suggest that this POVM should contain some diffusion dependence in order to obtain significant FI for the vanishing diffusion parameter as $\Delta \to 0$ (see Sec. (10.2.2)). A numerical routine was therefore employed and found that in the small particle number regime for HB states the bound $\mathrm{Tr}\left[\mathbf{FH}^{-1}\right]$ gets close to 1 as $\Delta \to 0$. Moreover, if diffusion is not too small then it is possible to obtain significant FI for both ϕ and Δ with a POVM which is Δ independent. This is the case for the canonical phase measurement where the numerical results, performed at $\Delta = 0.01$ and for particle number (K) between 1 and 80, show exactly this for higher K values.

The main conclusions are:

1. The QFI matrix in the small phase diffusion regime shows that HB probe states can achieve nearly Heisenberg like scaling not only for phase, but also for diffusion in the instances where the second order in diffusion terms are very small. This is promising for areas where estimation of small diffusive noise parameters is of interest such as thermometry.

2. In principle, quantum-limited simultaneous estimation of phase and phase diffusion is possible in the large phase diffusion regime for FPN states whose components are of equal magnitude. However, the quantum limits themselves decrease exponentially with diffusion and therefore, this is of practical importance in the instances where we are limited to such states. Nevertheless, this result advances the analytical understanding of this simultaneous estimation scheme. Additionally, it shows that the globally maximal bound

across all diffusion values, which may or may not coincide with the large phase diffusion regime, will also saturate the QCRB for such states.

3. As diffusion approaches zero, the numerical simulations for HB states suggest that one cannot achieve the quantum-limited precision for both parameters and the associated trade-off relation, $\mathrm{Tr}\left[\mathbf{F}\mathbf{H}^{-1}\right]$, approaches one. Therefore, the individual estimation of parameters is always favourable in such instances. However, the simultaneous estimation is sometimes unavoidable, for instance in imaging, and it is important to have the knowledge of the associated limitations. This numerical evidence still awaits an analytical understanding.

While this work provides several results on the simultaneous estimation of phase and phase diffusion and the relevant framework for further studies of quantum-limited estimation schemes in the presence of noise, there are still some immediate open questions:

1. The QFI matrix for HB states and general FPN states for arbitrary diffusion strength.
2. Analytical joint estimation bound in the small, and ideally, in arbitrary diffusion regimes.
3. Structure of the optimal POVM in the small, and ideally, in the general diffusion case.
4. Proof of optimality of the POVM in Eqn. (10.7) in the large diffusion regime.
5. Translation of the optimal POVMs into feasible experiments enabling optimal joint estimation of phase and diffusion.
6. Finally, the problem of estimating phase diffusion in the presence of loss and phase [147], and the quantum-limited estimation of phase diffusion simultaneously with multiple phases [148, 11, 94, 149, 4] also remain unaddressed.

Chapter 11

Overall thesis conclusion

Metrology has come a long way since its beginnings that can be traced back to the beginnings of humankind. It allowed improving people's quality of life by aiding the development of medicine, telecommunication, transport, navigation and sensing technologies. The advances in quantum physics can further benefit this field by exploring new platforms to reach higher sensitivities and studying the fundamental limits in the achievable precision in different estimation schemes. The quest for gravitational waves is a great example of this. The field of metrology is very broad and covers many areas. The work presented in this thesis investigated two aspects of metrology:

1. Optomechanical state estimation – experimental work

2. Precision bounds in quantum multi-parameter estimation – theoretical work.

The optomechanics project, presented in part II, considers a Brillouin system inside a microresonator evanescently coupled to an external laser field at room temperature. The system consists of one acoustic mode and two optical whispering gallery modes separated by the mechanical frequency of 11 GHz. The lower frequency optical (pump) mode is injected with the laser light which leads to scattering of the pump photons off the mechanical (acoustic) phonons into the higher frequency (anti-Stokes) mode. As a result, the mechanical mode is sideband cooled and the interaction between the mechanical and anti-Stokes modes can be represented by a beam-splitter interaction Hamiltonian with the pump mode acting as an auxiliary field. See Fig. (5.2). The anti-Stokes mode is continuously monitored by a heterodyne detector. The resulting data, in the form of oscilloscope's time traces, are input offline to an appropriate stochastic Gaussian model [79] developed in collaboration with Klaus Mølmer and Jinglei Zhang at the University of Aarhus. Such protocol, described in details in chapter 6, optimally uses the data to estimate phase space trajectories of the mechanical mode and subsequently enhances sideband cooling of this mode by means of reducing the uncertainty associated with its phase space coordinates. This effectively purifies the state and the results are shown in Fig (6.5). Another important message of part II is that heterodyne detection beats the commonly used in optomechanics homodyne detection in the amount of cooling that can be achieved for beam-splitter type interaction Hamiltonians. This is discussed in details in section 6.5. The experimental protocol presented in part II will have a positive contribution in the areas of optomechanics and sensing, and the manuscript for publication from this work is currently in preparation.

The quantum multi-parameter estimation project, presented in part III, theoretically considers the problem of simultaneous estimation of unitary and non-unitary parameters. While many metrology protocols consider interferometric phase as the parameter of interest, the presence of noise is unavoidable in real-life systems and will degrade the achievable precision associated with the unitary parameters. Additionally, the noise parameters may be the parameters of interest and their precise identification certainly improves our knowledge of the studied system. The precision with which the parameters can be estimated is determined by the choice of probe states and measurements. The main work presented in part III explores the simultaneous estimation of phase and phase diffusion in the framework of quantum Cramér-Rao bound using fixed-particle number states. In particular, the work aims to identify the quantum limits associated with the parameters in the form of quantum Fisher information matrix, defined in Eqn. (7.13), and whether these limits can be achieved simultaneously. The joint attainability of the precision limits can be quantified via the trade-off relation quantity defined in Eqn. (9.11) and it arises due to the possible non-commutativity of measurements in quantum mechanics.

Holland-Burnett states were considered in this work as the special case of fixed-particle number states which allow reaching the non-classical Heisenberg scaling in noise free phase estimation schemes. One of the goals of this research was to investigate how the attainability of the quantum limits given by quantum Fisher information is affected by the dimension of the state. Holland-Burnett states are a good choice for this as their dimension scales with the number of particles. The main results of this project include the derivation of the analytical quantum Fisher information matrices in the limits of large (Eqn. (10.4) and Eqn. (10.5)) and small (Eqn. (10.17) and Eqn. (10.18)) diffusive noise. The large diffusion limit is performed for a general fixed-particle number state whereas the small diffusion limit for the special case of Holland-Burnett states. In the limit of small diffusive noise, Holland-Burnett states attain the Heisenberg scaling in the individual estimation of both phase and phase diffusion. However, here, numerical simulations suggest that knowing one parameter precisely implies little information about the other parameter. Therefore, individual parameter estimation in this regime is favourable. The large diffusion analysis suggests that optimal estimation of both parameters simultaneously is possible. However, larger values of the noise parameter degrades the advantage of using non-classical schemes. Nevertheless, the result provides a more complete analytical understanding of the problem. The trade-off quantity for intermediate diffusion values was also considered numerically for Holland-Burnett states of low particle numbers. The results in Fig (10.9) suggest that the trade-off relation can reach close to its optimal value of 2 as the number of particles in the state and hence its dimension increases. This work was published in [5] and a review article on the topic of multi-parameter quantum metrology was published in [4]. The studies presented here provide the relevant framework for works concerning quantum-limited estimation with noise. In particular, it gives a starting point for imaging applications, where a multi-parameter estimation problem arises naturally.

Appendix A

Appendix for part III

A.1 QFI matrix elements in terms of the eigenbasis of the density matrix of the input probe state

The following is a proof for the alternative formula of the QFI matrix elements (H_{ij}), given in Eqn. (7.15), in terms of the eigenbasis of the density matrix of the input probe state. The SLD equation given by Eqn. (7.14) is the so called Lyapunov matrix equation which has a solution

$$\hat{L}_i = 2\int_0^\infty \mathrm{d}t \mathrm{e}^{-\hat{\varrho}_{\boldsymbol{\lambda}} t} \partial_{\lambda_i} \hat{\varrho}_{\boldsymbol{\lambda}} \mathrm{e}^{-\hat{\varrho}_{\boldsymbol{\lambda}} t}. \tag{A.1}$$

Writing $\hat{\varrho}_{\boldsymbol{\lambda}}$ in its eigenbasis, $\hat{\varrho}_{\boldsymbol{\lambda}} = \sum_k E_k |e_k\rangle\langle e_k|$, and applying the definition of an exponential function, $\mathrm{e}^{-\hat{\varrho}_{\boldsymbol{\lambda}} t} = \sum_{k=0}^{\infty} \frac{(-\hat{\varrho}_{\boldsymbol{\lambda}} t)^k}{k!}$ we obtain

$$\hat{L}_i = 2\sum_{n,m} \frac{\langle e_m | \partial_{\lambda_i} \hat{\varrho}_{\boldsymbol{\lambda}} | e_n\rangle}{E_n + E_m} |e_m\rangle\langle e_n|. \tag{A.2}$$

$\hat{L}_i\hat{L}_j$ can therefore be written as

$$\hat{L}_i\hat{L}_j = 4\sum_{n,m,n'} \frac{\langle e_m|\partial_{\lambda_i}\hat{\varrho}_{\boldsymbol{\lambda}}|e_n\rangle}{E_n+E_m}\frac{\langle e_n|\partial_{\lambda_j}\hat{\varrho}_{\boldsymbol{\lambda}}|e_{n'}\rangle}{E_{n'}+E_n}|e_m\rangle\langle e_{n'}|. \tag{A.3}$$

Writing $\hat{\varrho}_{\boldsymbol{\lambda}}$ in its eigenbasis form, the following expression for $\hat{\varrho}_{\boldsymbol{\lambda}}L_iL_j$ can be obtained,

$$\hat{\varrho}_{\boldsymbol{\lambda}}\hat{L}_i\hat{L}_j = 4\sum_{n,m,n'} E_m\frac{\langle e_m|\partial_{\lambda_i}\hat{\varrho}_{\boldsymbol{\lambda}}|e_n\rangle}{E_n+E_m}\frac{\langle e_n|\partial_{\lambda_j}\hat{\varrho}_{\boldsymbol{\lambda}}|e_{n'}\rangle}{E_{n'}+E_n}|e_m\rangle\langle e_{n'}|. \tag{A.4}$$

Taking the trace of the above expression and using the eigenbasis form for $\partial_{\lambda_i}\hat{\varrho}_{\boldsymbol{\lambda}}$, i.e. $\partial_{\lambda_i}\hat{\varrho}_{\boldsymbol{\lambda}} = \sum_k \partial_{\lambda_i}E_k|e_k\rangle\langle e_k| + E_k|\partial_{\lambda_i}e_k\rangle\langle e_k| + E_k|e_k\rangle\langle\partial_{\lambda_i}e_k|$, we get

$$\begin{aligned}\mathrm{Tr}[\hat{\varrho}_{\boldsymbol{\lambda}}\hat{L}_i\hat{L}_j] = 4\sum_{n,m}\frac{E_m}{(E_n+E_m)^2}&(\delta_{n,m}\partial_{\lambda_i}E_n + (E_n-E_m)\langle\partial_{\lambda_i}e_n|e_m\rangle)(\delta_{n,m}\partial_{\lambda_j}E_m \\ &+ (E_m-E_n)\langle\partial_{\lambda_j}e_m|e_n\rangle).\end{aligned} \tag{A.5}$$

Multiplying the brackets, using $\partial_{\lambda_i}\langle e_n|e_m\rangle \equiv \langle\partial_{\lambda_i}e_n|e_m\rangle + \langle e_n|\partial_{\lambda_i}e_m\rangle = 0$ and taking the real part of the resulting expression, the required formula for H_{ij} is

$$H_{ij} = \mathrm{Re}\left[\sum_n \frac{\partial_{\lambda_i}(E_n)\partial_{\lambda_j}(E_n)}{E_n} + 4\sum_{n,m}E_m\frac{(E_n-E_m)^2}{(E_n+E_m)^2}\langle e_n|\partial_{\lambda_i}e_m\rangle\langle\partial_{\lambda_j}e_m|e_n\rangle\right]. \tag{A.6}$$

A.2 FPN state in the phase dependent basis

Complex amplitudes, a_n, of $\hat{\varrho}$ can be written in the exponential form as $a_n = |a_n|\mathrm{e}^{\mathrm{i}\theta_n}$, where $\theta_n \in \{0, 2\pi\}$. With this, $\hat{\varrho}$ can be expressed as,

$$\hat{\varrho} = \sum_{n,n'=0}^{2K} |a_n||a_{n'}|\mathrm{e}^{\mathrm{i}[\phi(n-n')+\theta_n-\theta_{n'}]}\mathrm{e}^{-\frac{\Delta^2}{2}(n-n')^2}|n, 2K-n\rangle\langle n', 2K-n'|. \tag{A.7}$$

All the phases can be absorbed into the basis of $\hat{\varrho}$ and the same is true for its derivatives. Therefore, operating in this new basis, $|\Gamma_{n,K,\phi,\theta}\rangle = e^{\mathrm{i}(\phi n+\theta_n)}|n,2K-n\rangle$, all the matrix elements of $\hat{\varrho}$ and $\partial_\Delta\hat{\varrho}$ are positive, and all the elements of $\partial_\phi\hat{\varrho}$ are imaginary. The corresponding matrix representations are,

$$\hat{\varrho} = \sum_{n,n'=0}^{2K} |a_n||a_{n'}|\mathrm{e}^{-\frac{\Delta^2}{2}(n-n')^2}|\Gamma_{n,K,\phi,\theta}\rangle\langle\Gamma_{n',K,\phi,\theta}|, \tag{A.8}$$

$$\partial_\phi\hat{\varrho} = \mathrm{i}\sum_{n,n'=0}^{2K} (n-n')|a_n||a_{n'}|\mathrm{e}^{-\frac{\Delta^2}{2}(n-n')^2}|\Gamma_{n,K,\phi,\theta}\rangle\langle\Gamma_{n',K,\phi,\theta}|, \tag{A.9}$$

$$\partial_\Delta\hat{\varrho} = -\Delta\sum_{n,n'=0}^{2K} (n-n')^2|a_n||a_{n'}|\mathrm{e}^{-\frac{\Delta^2}{2}(n-n')^2}|\Gamma_{n,K,\phi,\theta}\rangle\langle\Gamma_{n',K,\phi,\theta}|. \tag{A.10}$$

A.3 Quantum Fisher information numerical routine

The numerical routine for calculating QFI relies on vectorising the SLD equation, given in Eqn. (7.14), so that it becomes

$$2|\partial_{\lambda_i}\hat{\varrho}\rangle = [\hat{\varrho}\otimes\hat{I} + \hat{I}\otimes\hat{\varrho}^{\mathrm{T}}]|L_i\rangle, \tag{A.11}$$

where $\hat{I}$ is the identity matrix. $\hat{\varrho}$ can be written in its eigenbasis representation as $\hat{\varrho} = VDV^\dagger$, where V is the matrix of eigenvectors of $\hat{\varrho}$ and D is the corresponding diagonal matrix of eigenvalues. Similarly, $\hat{\varrho}^{\mathrm{T}}$ can be expressed as $V^\star DV^{\mathrm{T}}$. Therefore, the right hand side of Eqn. (A.11) becomes

$$\begin{aligned}
&[\hat{\varrho}\otimes\hat{I} + \hat{I}\otimes\hat{\varrho}^T]|L_i\rangle = \\
&= [(V\otimes V^\star)(D\otimes\hat{I})(V^\dagger\otimes V^T) \\
&\quad + (V\otimes V^\star)(\hat{I}\otimes D)(V^\dagger\otimes V^T)]|L_i\rangle \\
&= (V\otimes V^\star)(D\otimes\hat{I} + \hat{I}\otimes D)(V\otimes V^\star)^\dagger|L_i\rangle.
\end{aligned} \tag{A.12}$$

$|L_i\rangle$ can therefore be found by taking the inverse of $D \otimes \hat{I} + \hat{I} \otimes D$ so that it can be written as

$$|L_i\rangle = 2(V \otimes V^\star)(D \otimes \hat{I} + \hat{I} \otimes D)^{-1}(V \otimes V^\star)^\dagger)|\partial_{\lambda_i}\hat{\varrho}\rangle. \tag{A.13}$$

The numerical QFIs can then be found by putting $|L_i\rangle$ back into its matrix form and substituting it into Eqn. (7.13).

A.4 Validity of the large diffusion approximation

We evaluate the error associated with the large phase diffusion approximation by considering norm one of the matrix composed of the neglected elements of the original density matrix $\hat{\varrho}$ (Eqn. (9.4)). Therefore, the error ϵ can be expressed as

$$\epsilon = \sum_{n,n'=0}^{2K} \left|\hat{\varrho}_{n,n'} - \hat{\varrho}_{L\Delta n,n'}\right| = \sum_{\substack{n,n'=0,\\ n\neq n',\\ n\neq n'\pm k}}^{2K} |a_n||a_{n'}|x^{2(n-n')^2}, \tag{A.14}$$

where we used the fact that the magnitude of the complex exponential is 1. We can overestimate the error by setting the power of x to the lowest possible number, $(n-n')_{min} = k+1$, which corresponds to the first off-diagonal that is negligible within the approximation. For the special case of HB states, $k = 2$, but also $(n-n')_{min} = k+2$ since only even numbered off-diagonals contribute non-zero elements to the density matrix. With this, the errors for a general FPN state and for the special case of HB states (where $a_n = b_{\frac{n}{2}}\delta_{n,2q}$ as defined in Eqn. (9.2)) are respectively

$$\epsilon^{(FPN)} \leq x^{2(k+1)^2}\left(-1 + \sum_{\substack{n,n'=0,\\ n\neq n'\pm k}}^{2K} |a_n||a_{n'}|\right) \tag{A.15}$$

and

$$\epsilon^{(HB)} \leq x^{2(k+2)^2}\left(-1+\sum_{\substack{n,n'=0,\\ n\neq n'\pm k}}^{2K}|a_n||a_{n'}|\right) = x^{32}\left(-1+\sum_{\substack{n,n'=0,\\ n\neq n'\pm 1}}^{K} b_n b_{n'}\right). \tag{A.16}$$

The summation term in Eqn. (A.15) and Eqn. (A.16) consists of two sums, one positive $\sum_{n,n'=0}^{2K}|a_n||a_{n'}|$ and one negative $2\sum_{n=k}^{2K}|a_n||a_{n-k}|$. To further overestimate the error, we can set the negative part of the summation to zero. Additionally, to derive a closed form of the error in terms of K, we can overestimate the error even further by setting $|a_n| = |a_{n'}|$. This is due to the arithmetic-harmonic mean inequality for positive numbers, $(|a_n|+|a_{n'}|)/2 \geq 2|a_n||a_{n'}|/(|a_n|+|a_{n'}|)$, which can be re-written as $|a_n||a_{n'}| \leq \left(|a_n|^2+|a_{n'}|^2\right)/2$ with equality when $|a_n| = |a_{n'}|$. The amount by which the errors are overestimated gets worse when $k > 1$ since some of the coefficients a_n are zero. We can account for this in the case of HB states by reducing the Hilbert space from $2K$ to K as shown in Eqn. (A.16). We therefore obtain the following errors

$$\epsilon^{(FPN)} \leq x^{2(k+1)^2}\left(-1+\sum_{n,n'=0}^{2K}|a_n|^2\right) = 2Kx^{2(k+1)^2} \tag{A.17}$$

and

$$\epsilon^{(HB)} \leq Kx^{32}. \tag{A.18}$$

We evaluate the validity of the approximation by defining the error ϵ (equations (A.15), (A.16), (A.17) and (A.18)) as some fraction f of the sum of the elements of the original density matrix $\hat{\varrho}$. Therefore,

$$\epsilon = f\sum_{n,n'=0}^{2K}\left|\varrho_{n,n'}\right| = \sum_{n,n'=0}^{2K}|a_n||a_{n'}|x^{2(n-n')^2}. \tag{A.19}$$

We can tighten our error bound by using the lowest possible value of $\sum_{n,n'=0}^{2K}\left|\varrho_{n,n'}\right|$ which is 1. This effectively demands our error to be smaller than that given in Eqn. (A.19) and re-defines it as,

$$\epsilon = f. \tag{A.20}$$

This translates to the following regimes of Δ within which our approximation is valid,

$$\Delta^{(FPN)} \geq \sqrt{\frac{2}{(k+1)^2} \ln\left(\frac{2K}{f}\right)} \tag{A.21}$$

or in terms of the coefficients, a_n, of the FPN state

$$\Delta^{(FPN)} \geq \sqrt{\frac{2}{(k+1)^2}} \sqrt{\ln\left[\frac{1}{f}\left(-1+\sum_{\substack{n,n'=0,\\ n\neq n'\pm k}}^{2K} |a_n||a_{n'}|\right)\right]} \tag{A.22}$$

and

$$\Delta^{(HB)} \geq \sqrt{\frac{1}{8} \ln\left(\frac{K}{f}\right)} \tag{A.23}$$

or in terms of the coefficients of the HB state b_n

$$\Delta^{(HB)} \geq \sqrt{\frac{1}{8} \ln\left[\frac{1}{f}\left(-1+\sum_{\substack{n,n'=0,\\ n\neq n'\pm k}}^{K} b_n b_{n'}\right)\right]}. \tag{A.24}$$

Eqn. (A.21) and Eqn. (A.23) show the $\sqrt{\ln(K)}$ dependence on the threshold value of Δ for the considered relative error f.

The exact numerical validity plot for the actual QFI is shown in Fig. (A.1) in the case of HB states. It shows the minimum values of Δ as a function of particle number (K) when the highest allowed relative error ($\delta H_{ii}/H_{ii}$) is 0.05.

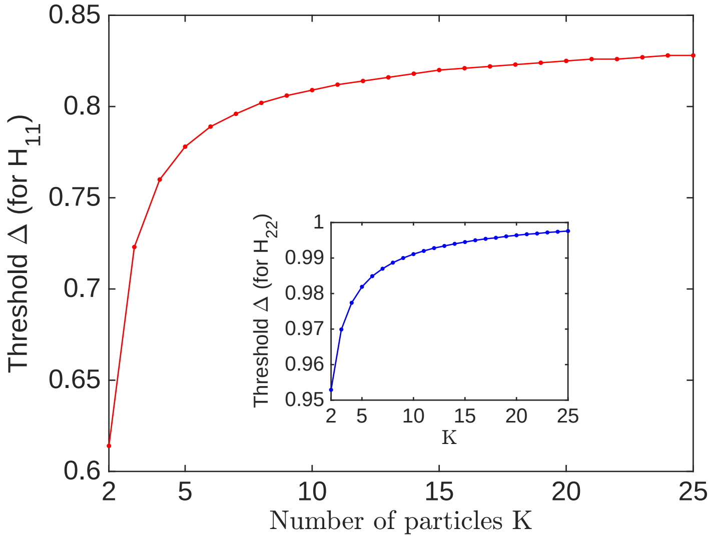

Figure A.1: Phase diffusion numerical validity plot within the large phase diffusion approximation for HB states. The figure shows the threshold values of Δ as a function of particle number (K) when the highest allowed relative error on the QFI is 0.05. $K = 1$ case is not shown as it already gives a tridiagonal density matrix and therefore an exact solution valid for all Δ.

A.5 SLD matrices in the large diffusion regime

In the large Δ approximation, the SLDs for a general FPN state are given by the following expressions,

$$\hat{L}_{1,\mathrm{L}\Delta} = 2\mathrm{i}x^{2k^2} \sum_{n,n'=0}^{2K} (n-n') \frac{a_n a_{n'}^*}{|a_n|^2 + |a_{n'}|^2} \mathrm{e}^{\mathrm{i}\phi(n-n')} \delta_{n,n'\pm k} |n, 2K-n\rangle\langle n', 2K-n'| \tag{A.25}$$

and

$$\hat{L}_{2,\mathrm{L}\Delta} = -2k^2 \Delta x^{2k^2} \sum_{n,n'=0}^{2K} \frac{a_n a_{n'}^*}{|a_n|^2 + |a_{n'}|^2} \mathrm{e}^{\mathrm{i}\phi(n-n')} \delta_{n,n'\pm k} |n, 2K-n\rangle\langle n', 2K-n'|, \tag{A.26}$$

where subscripts 1 and 2 refer to ϕ and Δ respectively. The above SLDs can be substituted into the SLD equation, Eqn. (7.14), to check that these are the correct solutions within the approximation. Firstly, we perform such verification for $\hat{L}_{1,\mathrm{L}\Delta}$. The left hand side of the SLD equation is,

$$
\begin{aligned}
2\partial_\phi \hat{\varrho}_{\mathrm{L}\Delta} &= 2\mathrm{i} \sum_{n,n'=0}^{2K} a_n a_{n'}^* (n-n') \mathrm{e}^{\mathrm{i}\phi(n-n')} x^{2(n-n')^2} (\delta_{n,n'} + \delta_{n,n'\pm k}) |n, 2K-n\rangle\langle n', 2K-n'| \\
&= 2\mathrm{i} x^{2k^2} \sum_{n,n'=0}^{2K} a_n a_{n'}^* (n-n') \mathrm{e}^{\mathrm{i}\phi(n-n')} \delta_{n,n'\pm k} |n, 2K-n\rangle\langle n', 2K-n'|,
\end{aligned}
\tag{A.27}
$$

where $\delta_{n,n'}$ does not contribute any non-zero terms due to the factor of $(n-n')$ appearing in the summation. To calculate the right hand side of the SLD equation, we require expressions for $\hat{\varrho}_{\mathrm{L}\Delta}\hat{L}_{1,\mathrm{L}\Delta}$ and $\hat{L}_{1,\mathrm{L}\Delta}\hat{\varrho}_{\mathrm{L}\Delta}$,

$$
\begin{aligned}
\hat{\varrho}_{\mathrm{L}\Delta}\hat{L}_{1,\mathrm{L}\Delta} = 2\mathrm{i} x^{2k^2} &\sum_{n,n',m'=0}^{2K} (n-n') \frac{a_n |a_{n'}|^2 a_{m'}^*}{|a_n|^2 + |a_{n'}|^2} \mathrm{e}^{i\phi(n-m')} x^{2(n'-m')^2} \\
&\qquad \times (\delta_{n',m'} + \delta_{n',m'\pm k}) \delta_{n,n'\pm k} |n, 2K-n\rangle\langle m', 2K-m'| \\
= 2\mathrm{i} x^{2k^2} &\sum_{n,n'=0}^{2K} (n-n') \frac{a_n a_{n'}^* |a_{n'}|^2}{|a_n|^2 + |a_{n'}|^2} \mathrm{e}^{\mathrm{i}\phi(n-n')} \delta_{n,n'\pm k} |n, 2K-n\rangle\langle n', 2K-n'|
\end{aligned}
\tag{A.28}
$$

and

$$
\begin{aligned}
\hat{L}_{1,\mathrm{L}\Delta}\hat{\varrho}_{\mathrm{L}\Delta} &= (\hat{\varrho}_{\mathrm{L}\Delta}\hat{L}_{1,\mathrm{L}\Delta})^\dagger \\
&= 2\mathrm{i} x^{2k^2} \sum_{n,n'=0}^{2K} (n-n') \frac{a_n a_{n'}^* |a_n|^2}{|a_n|^2 + |a_{n'}|^2} \mathrm{e}^{\mathrm{i}\phi(n-n')} \delta_{n,n'\pm k} |n, 2K-n\rangle\langle n', 2K-n'|.
\end{aligned}
\tag{A.29}
$$

In obtaining Eqn. (A.28) and Eqn. (A.29), we keep terms of order up to x^{2k^2} only. The right hand side of the SLD equation is a sum of Eqn. (A.28) and Eqn. (A.29) and hence

$$
\begin{aligned}
\hat{\varrho}_{\mathrm{L}\Delta}\hat{L}_{1,\mathrm{L}\Delta} + \hat{L}_{1,\mathrm{L}\Delta}\hat{\varrho}_{\mathrm{L}\Delta} &= 2\mathrm{i} x^{2k^2} \sum_{n,n'=0}^{2K} (n-n') \frac{a_n a_{n'}^* (|a_n|^2 + |a_{n'}|^2)}{|a_n|^2 + |a_{n'}|^2} \mathrm{e}^{\mathrm{i}\phi(n-n')} \delta_{n,n'\pm k} |n, 2K-n\rangle\langle n', 2K-n'| \\
&= 2\mathrm{i} x^{2k^2} \sum_{n,n'=0}^{2K} (n-n') a_n a_{n'}^* \mathrm{e}^{\mathrm{i}\phi(n-n')} \delta_{n,n'\pm k} |n, 2K-n\rangle\langle n', 2K-n'|
\end{aligned}
\tag{A.30}
$$

which is equal to Eqn. (A.27) i.e. $2\partial_\phi \hat{\varrho}_{\mathrm{L}\Delta}$. Therefore, Eqn. (A.25) gives the correct expression for $\hat{L}_{1,\mathrm{L}\Delta}$ up to the order of $x^{2k^2} = \mathrm{e}^{-2k^2\Delta^2/4}$. A similar proof can be constructed for $\hat{L}_{2,\mathrm{L}\Delta}$, however, here the order of accuracy is attenuated from x^{2k^2} to $x^{2k^2-4\Delta^{-2}\ln(\Delta)}$ due to the presence of the factor of Δ.

A.6 QFI elements in the large diffusion regime

The following is the calculation of $H_{11,\mathrm{L}\Delta}$, QFI corresponding to the individual estimation of phase, in the large diffusion regime for a general FPN state. Firstly, we calculate $\hat{L}^2_{1,\mathrm{L}\Delta}$,

$$
\begin{aligned}
(\hat{L}_{1,\mathrm{L}\Delta})^2 = -4x^{4k^2} \sum_{n,n',m'=0}^{2K} (n-n')(n'-m') \frac{a_n a^*_{m'} |a_{n'}|^2}{(|a_n|^2+|a_{n'}|^2)(|a_{n'}|^2+|a_{m'}|^2)} \mathrm{e}^{\mathrm{i}\phi(n-m')} \delta_{n,n'\pm k}\delta_{n',m'\pm k} \\
\times |n,2K-n\rangle\langle m',2K-m'|.
\end{aligned}
\tag{A.31}
$$

With this,

$$
\begin{aligned}
\hat{\varrho}_{\mathrm{L}\Delta}(\hat{L}_{1,\mathrm{L}\Delta})^2 &= -4x^{4k^2} \sum_{l,n,n',m'=0}^{2K} (n-n')(n'-m') \frac{a_l |a_n|^2 |a_{n'}|^2 a^*_{m'}}{(|a_n|^2+|a_{n'}|^2)(|a_{n'}|^2+|a_{m'}|^2)} \mathrm{e}^{\mathrm{i}\phi(l-m')} x^{2(l-n)^2} \\
&\quad \times \delta_{n,n'\pm k}\delta_{n',m'\pm k}(\delta_{l,n}+\delta_{l,n\pm k})|l,2K-l\rangle\langle m',2K-m'| \\
&= -4x^{4k^2} \sum_{n,n',m'=0}^{2K} (n-n')(n'-m') \frac{a_n |a_n|^2 |a_{n'}|^2 a^*_{m'}}{(|a_n|^2+|a_{n'}|^2)(|a_{n'}|^2+|a_{m'}|^2)} \mathrm{e}^{\mathrm{i}\phi(n-m')} \\
&\quad \times \delta_{n,n'\pm k}\delta_{n',m'\pm k}|n,2K-n\rangle\langle m',2K-m'|,
\end{aligned}
\tag{A.32}
$$

where in Eqn. (A.32), terms of order higher than x^{4k^2} are neglected as explained in the main text. The total neglected term is given by δq_ϕ,

$$\begin{aligned}\delta q_\phi = -4x^{4k^2} \sum_{l,n,n',m=0}^{2K} (n-n')(n'-m)\frac{a_l|a_n|^2|a_{n'}|^2 a_m^*}{(|a_n|^2+|a_{n'}|^2)(|a_{n'}|^2+|a_m|^2)}\mathrm{e}^{\mathrm{i}\phi(l-m)}x^{2(l-n)^2} \\ \times\,\delta_{n,n'\pm k}\delta_{n',m\pm k}\delta_{l,n\pm k}|l,2K-l\rangle\langle m,2K-m|.\end{aligned} \tag{A.33}$$

Taking the trace of the neglected term in Eqn. (A.33) gives zero and therefore neglecting terms of order higher than x^{4k^2} contributes no error to the actual QFI. Taking the trace of Eqn. (A.32) gives,

$$\begin{aligned}\mathrm{Tr}[\hat{\varrho}_{\mathrm{L}\Delta}(\hat{L}_{1,\mathrm{L}\Delta})^2] &= 4x^{4k^2}\sum_{n,n'=0}^{2K}(n-n')^2\frac{|a_n|^4|a_{n'}|^2}{(|a_n|^2+|a_{n'}|^2)^2}\delta_{n,n'\pm k} \\ &= 4k^2x^{4k^2}\left(\sum_{n=k}^{2K}\frac{|a_n|^4|a_{n-k}|^2}{(|a_n|^2+|a_{n-k}|^2)^2}+\sum_{n'=k}^{2K}\frac{|a_{n'-k}|^4|a_{n'}|^2}{(|a_{n'-k}|^2+|a_{n'}|^2)^2}\right) \\ &= 4k^2x^{4k^2}\sum_{n=k}^{2K}\frac{|a_n|^2|a_{n-k}|^2}{|a_n|^2+|a_{n-k}|^2}.\end{aligned} \tag{A.34}$$

As all the terms in the above expression are real then this is also equal to $H_{11,\mathrm{L}\Delta}$. The same procedure can be performed to calculate $H_{22,\mathrm{L}\Delta}$, QFI corresponding to the individual estimation of Δ. In this case, the neglected term also contributes zero to the actual QFI.

We can upper-bound the summation term, $A=\sum_{n=k}^{2K}|a_n|^2|a_{n-k}|^2/\left(|a_n|^2+|a_{n-k}|^2\right)$, appearing in Eqn. (A.34) by noting that the terms inside the sum have the form of the harmonic mean and therefore,

$$A \le \frac{1}{2}\sum_{n=k}^{2K}\frac{|a_n|^2+|a_{n-k}|^2}{2} \tag{A.35}$$

with the equality when $|a_n|^2=|a_{n-k}|^2$ for $n\in\mathbb{Z}\{k:2K\}$. Further, we can expand the sum on the

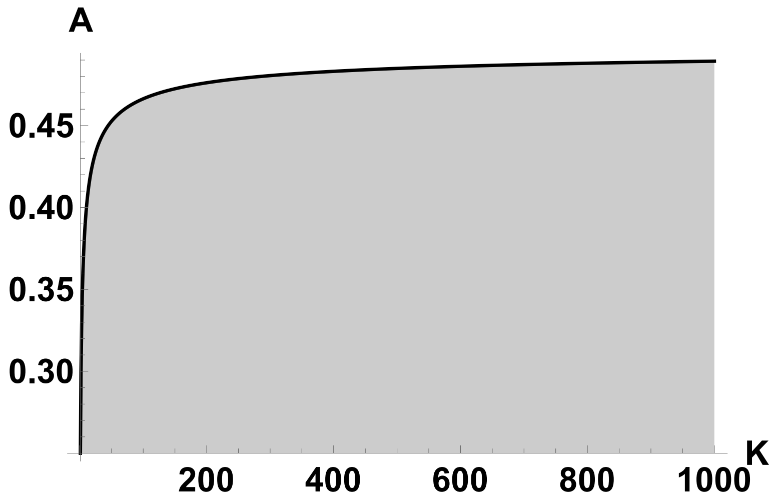

Figure A.2: The summation term (A) in Eqn. (A.34) gets close to 1/2 at large K. For K = 1000, A = 0.49.

right hand side and re-group its elements to give

$$A \leq \frac{1}{4}(|a_0|^2 + \ldots + |a_{2K}|^2 + |a_k|^2 + \ldots + |a_{2K-k}|^2). \tag{A.36}$$

Using $\sum_{n=0}^{2K} |a_n|^2 = 1$ we obtain

$$A \leq \frac{1}{2} - \frac{1}{4}\sum_{n=0}^{k-1}(|a_n|^2 + |a_{2K-n}|^2) \tag{A.37}$$

which gives the upper bound of 1/2 when $\sum_{n=0}^{k-1}(|a_n|^2 + |a_{2K-n}|^2)/4 = 0$.

For HB states, the upper bound of 1/2 is reached when $\left(|b_0|^2 + |b_K|^2\right)/4 = 0$. This condition and hence the upper bound is asymptotically reached when K becomes large as shown in Fig. (A.2).

A.7 Complementary QFI plot to Fig. (10.2)

Fig. (A.3) shows a linear plot of the QFI as a function of Δ for large phase diffusion values.

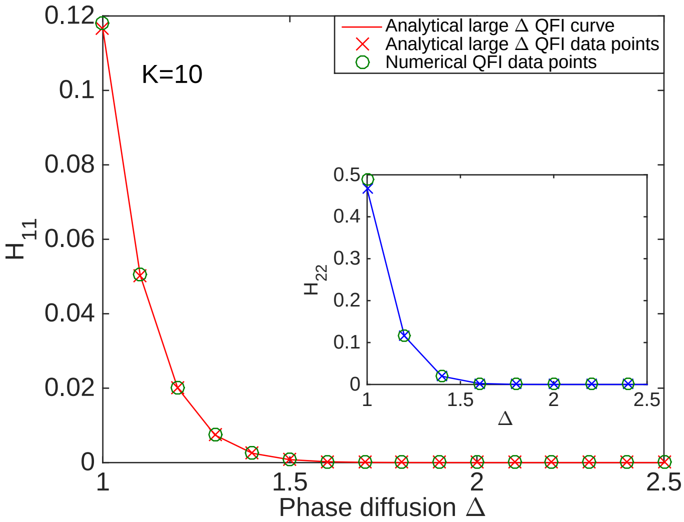

Figure A.3: Complementary figure to Fig. (10.2) showing a linear plot of the QFI as a function of Δ for large phase diffusion values. Additionally to the curve, we plotted the sampled Δ points for the analytical QFI expression (crosses) to magnify the calculation error for smaller Δ values.

A.8 Trade-off in the large diffusion regime

We consider orthonormal projective measurments acting on a single copy of the evolved FPN state, given in Eqn. (9.4). Such a measurement can be realized by a POVM set $\{|v_y\rangle\langle v_y|\}$, where

$$|v_y\rangle = \sum_{n=0}^{2K} r_{y,n} \mathrm{e}^{\mathrm{i}X_{y,n}} |n, 2K-n\rangle \tag{A.38}$$

with $r_{y,n} \in \Re\{0:1\}$ and $X_{y,n} \in \Re\{0:2\pi\}$. The completeness relation, $\sum_{y=0}^{2K} |v_y\rangle\langle v_y| = \hat{\mathbb{1}}$, and the normalisation give the following constraints respectively,

$$\sum_{y=0}^{2K} r_{y,n} r_{y,n'} \mathrm{e}^{\mathrm{i}(X_{y,n}-X_{y,n'})} = \delta_{n,n'} \tag{A.39}$$

and

$$\sum_{n=0}^{2K} r_{y,n}^2 = 1. \tag{A.40}$$

The probability associated with the y^{th} outcome and its corresponding derivatives with respect to ϕ and Δ are given by,

$$p_y = \langle v_y|\hat{\varrho}_{L\Delta}|v_y\rangle = \sum_{n=0}^{2K} r_{y,n}^2|a_n|^2 + 2x^{2k^2}\sum_{n=k}^{2K} r_{y,n}r_{y,n-k}|a_n||a_{n-k}|\cos(\Theta_{y,n,k}) \tag{A.41}$$

$$\partial_\phi p_y = -2kx^{2k^2}\sum_{n=k}^{2K} r_{y,n}r_{y,n-k}|a_n||a_{n-k}|\sin\left(\Theta_{y,n,k}\right) \tag{A.42}$$

and

$$\partial_\Delta p_y = -2k^2\Delta x^{2k^2}\sum_{n=k}^{2K} r_{y,n}r_{y,n-k}|a_n||a_{n-k}|\cos\left(\Theta_{y,n,k}\right), \tag{A.43}$$

where $\Theta_{y,n,k} = \left(X_{y,n-k} - X_{y,n} + \theta_n - \theta_{n-k} + k\phi\right)$. Using Eqn. (7.11), the resulting elements of the Fisher information matrix, F_{11} and F_{22}, corresponding to the individual estimation of ϕ and Δ are given by,

$$\begin{aligned} F_{11} &= 4k^2x^{4k^2}\sum_{y=0}^{2K}\left(\frac{\left(\sum_{n=k}^{2K} r_{y,n}r_{y,n-k}|a_n||a_{n-k}|\sin\left(\Theta_{y,n,k}\right)\right)^2}{\sum_{n=0}^{2K}\left(r_{y,n}^2|a_n|^2\right) + 2x^{2k^2}\sum_{n=k}^{2K}\left(r_{y,n}r_{y,n-k}|a_n||a_{n-k}|\cos\left(\Theta_{y,n,k}\right)\right)}\right) \\ &= 4k^2x^{4k^2}\sum_{y=0}^{2K}\left(\frac{\left(\sum_{n=k}^{2K} r_{y,n}r_{y,n-k}|a_n||a_{n-k}|\sin\left(\Theta_{y,n,k}\right)\right)^2}{\sum_{n=0}^{2K} r_{y,n}^2|a_n|^2}\right) \end{aligned} \tag{A.44}$$

and

$$\begin{aligned} F_{22} &= 4k^4\Delta^2x^{4k^2}\sum_{y=0}^{2K}\left(\frac{\left(\sum_{n=k}^{2K} r_{y,n}r_{y,n-k}|a_n||a_{n-k}|\cos\left(\Theta_{y,n,k}\right)\right)^2}{\sum_{n=0}^{2K}\left(r_{y,n}^2|a_n|^2\right) + 2x^{2k^2}\sum_{n=k}^{2K}\left(r_{y,n}r_{y,n-k}|a_n||a_{n-k}|\cos\left(\Theta_{y,n,k}\right)\right)}\right) \\ &= 4k^4\Delta^2x^{4k^2}\sum_{y=0}^{2K}\left(\frac{\left(\sum_{n=k}^{2K} r_{y,n}r_{y,n-k}|a_n||a_{n-k}|\cos\left(\Theta_{y,n,k}\right)\right)^2}{\sum_{n=0}^{2K} r_{y,n}^2|a_n|^2}\right), \end{aligned} \tag{A.45}$$

where we neglect orders higher than x^{4k^2} to obtain the final expressions. The trade-off, $\mathrm{Tr}\left[\mathbf{FH}^{-1}\right] = F_{11}/H_{11} + F_{22}/H_{22}$, is calculated using quantum limits found in Eqn. (10.4) and Eqn. (10.5). It is

$$\begin{aligned}
\mathrm{Tr}[\mathbf{FH}^{-1}] &= \frac{1}{s}\sum_{y=0}^{2K}\Bigg(\frac{1}{\sum_{n=0}^{2K} r_{y,n}^2|a_n|^2}\sum_{n,n'=k}^{2K} r_{y,n}r_{y,n-k}r_{y,n'}r_{y,n'-k}|a_n||a_{n-k}||a_{n'}||a_{n'-k}| \\
&\qquad \times \left(\sin\left(\Theta_{y,n,k}\right)\sin\left(\Theta_{y,n',k}\right) + \cos\left(\Theta_{y,n,k}\right)\cos\left(\Theta_{y,n',k}\right)\right)\Bigg) \\
&= \frac{1}{s}\sum_{y=0}^{2K}\left(\frac{\sum_{n,n'=k}^{2K} r_{y,n}r_{y,n-k}r_{y,n'}r_{y,n'-k}|a_n||a_{n-k}||a_{n'}||a_{n'-k}|\cos\left(\Theta_{y,n,k}-\Theta_{y,n',k}\right)}{\sum_{n=0}^{2K} r_{y,n}^2|a_n|^2}\right),
\end{aligned} \tag{A.46}$$

where $s = \sum_{n=k}^{2K}|a_n|^2|a_{n-k}|^2/\left(|a_n|^2+|a_{n-k}|^2\right)$ and to obtain the final expression, we used the identity $\cos(a-b) = \cos(a)\cos(b) + \sin(a)\sin(b)$. Since s, $r_{y,n}$ and $|a_n|$ in Eqn. (A.46) are positive then the trade-off is maximised when $\cos\left(\Theta_{y,n,k}-\Theta_{y,n',k}\right) = 1$. Further, assuming projectors whose coefficients have equally weighted magnitudes i.e. $r_{y,n} = 1/\sqrt{\frac{2K}{k}+1}$, we get the trade-off as given by Eqn. (10.8).

A.9 Linear independence of the elements of sets $\mathcal{W}_1$ and $\mathcal{W}_2$

Sets $\mathcal{W}_1$ and $\mathcal{W}_2$ are described in Eqn. (10.12) and Eqn. (10.13). Their elements consist of vectors $|w_k\rangle = \sum_{n=0}^{K} n^{k-1}|\varphi_n\rangle$ for $k = \{1,\dots,N\}$, where N (number of vector elements) is 3 for $\mathcal{W}_1$ and 5 for $\mathcal{W}_2$. We are interested in a situation, where $(K+1) \geq N$ since the size of the density matrix in the number basis is $(K+1)\times(K+1)$. A set is linearly dependent if one of the vectors in the set can be expressed as a linear combination of the other vectors. If none of the vectors is linearly dependent then the set is said to be linearly independent. Mathematically, the linear independence can be stated as

$$\begin{aligned}
&\sum_{k=1}^{N} c_{k-1}\sum_{n=0}^{K} n^{k-1}|\varphi_n\rangle = 0 \\
&\text{iff}\, c_{k-1} = 0 \,\text{for}\, k = \{1,\dots,N\}.
\end{aligned} \tag{A.47}$$

The above condition can be re-written as

$$\begin{aligned}
&\sum_{n=0}^{K}\left(\sum_{k=1}^{N} c_{k-1} n^{k-1}\right)|\varphi_n\rangle = 0 \\
&\text{iff}\, c_{k-1} = 0\,\text{for}\, k = \{1, \dots, N\}
\end{aligned} \tag{A.48}$$

and since vectors $\varphi_n = b_n \mathrm{e}^{2\mathrm{i}\phi n}|2n, 2K-2n\rangle,\ n = \{0, \dots, K\}$ are orthogonal then the condition for linear independence can be further simplified to

$$\begin{aligned}
&\sum_{k=1}^{N} c_{k-1} n^{k-1} = c_0 + c_1 n + c_2 n^2 + \dots + c_N n^N = 0 \\
&\text{for}\, n = \{0, \dots, K\} \\
&\text{iff}\, c_{k-1} = 0\,\text{for}\, k = \{1, \dots, N\}.
\end{aligned} \tag{A.49}$$

We, therefore, obtain $(K+1)$ distinct, simultaneous equations, corresponding to cases $n = \{0, \dots, K\}$, with N unknowns. However, the first equation ($n = 0$ case) imposes condition $c_0 = 0$. Therefore, after solving for the first N equations we will obtain two equations relating two unknowns, but there will be a contradiction because the two unknowns (in each of the two equations) will be related by a different constant factor because the coefficients in front of c_{k-1} take different values for each equation. Therefore, if $(K+1) \geq N$ then $\sum_{k=1}^{N} c_{k-1} n^{k-1}$ can only be satisfied if $c_{k-1} = 0\,\text{for}\, k = \{1, \dots, N\}$ as required by the linear independence condition.

To see this, we can consider an example of $\mathcal{W}_1$ set containing $N = 3$ vectors and $K = 2$. We get the following 3 simultaneous equations,

$$\begin{aligned}
&c_0 = 0 \\
&c_0 + c_1 + c_2 = 0 \\
&c_0 + 2c_1 + 4c_2 = 0.
\end{aligned} \tag{A.50}$$

It is clear that if $c_0 = 0$, as required by the first equation in (A.50), then the remaining two equations, will be in contradiction.

A.10 Gram Schmidt procedure and orthonormal sets $\mathcal{V}_1$ and $\mathcal{V}_2$

The first vector $|w_1\rangle$ of sets $\mathcal{W}_1$ and $\mathcal{W}_2$, given in equations (10.12) and (10.13), is already normalised and therefore, it can be taken as the first element $|v_1\rangle$ of the orthonormal sets $\mathcal{V}_1$ and $\mathcal{V}_2$. The remaining vectors are found using

$$|v_{k+1}\rangle = \frac{|w_{k+1}\rangle - \sum_{i=1}^{K}\langle v_i|w_{k+1}\rangle|v_i\rangle}{\||w_{k+1}\rangle - \sum_{i=1}^{K}\langle v_i|w_{k+1}\rangle|v_i\rangle\|}. \tag{A.51}$$

The Gram Schmidt procedure produces the following orthonormal basis set,

$$\begin{aligned}
|v_1\rangle &= \sum_{n=0}^{K}|\varphi_n\rangle,\\
|v_2\rangle &= \frac{2\sqrt{2}\sum_{n=0}^{K}(n-\frac{K}{2})|\varphi_n\rangle}{\sqrt{\prod_{n=0}^{1}(n+K)}},\\
|v_3\rangle &= \frac{8\sqrt{2}\sum_{n=0}^{K}((n-\frac{K}{2})^2-\frac{K}{8}(K+1))|\varphi_n\rangle}{\sqrt{\prod_{n=0}^{3}(n+K-1)}},\\
|v_4\rangle &= \frac{-\sqrt{2}}{\sqrt{\prod_{n=0}^{5}(n+K-2)}}\sum_{n=0}^{K}(K-2n)(2+(-3+K)K+16n(n-K))|\varphi_n\rangle,\\
|v_5\rangle &= \frac{\sqrt{2}}{\sqrt{\prod_{n=0}^{7}(n+K-3)}}\sum_{n=0}^{K}(\prod_{n'=0}^{3}(K-n')-32K(2+(K-1)K)n\\
&\qquad +32(2+K(5K-1))n^2-256Kn^3+128n^4)|\varphi_n\rangle.
\end{aligned} \tag{A.52}$$

A.11 Reduced HB density matrix and its diagonalisation in the small diffusion regime

In the small Δ approximation, the HB density matrix can be Taylor expanded to the second and fourth order in Δ about $\Delta = 0$, as shown in Eqn. (10.9) and Eqn. (10.10). The entries of $\hat{\varrho}'_{1,S\Delta}$ (see Eqn. (10.15)) in terms of K and Δ are

$$
\begin{aligned}
b_{11} &= 1 - \frac{\Delta^2}{2} K(K+1), \\
b_{13} &= -\frac{\Delta^2}{4\sqrt{2}} \sqrt{\prod_{n=0}^{3} (n+K-1)}, \\
b_{22} &= \frac{\Delta^2}{2} K(K+1),
\end{aligned}
\tag{A.53}
$$

and the entries of $\hat{\varrho}'_{2,S\Delta}$ (see Eqn. (10.16)) are

$$
\begin{aligned}
c_{11} &= 1 + \frac{\Delta^2}{32} K(K+1)(-16 + \Delta^2(-2 + 9K(K+1))), \\
c_{13} &= \frac{1}{8\sqrt{2}} \sqrt{\prod_{n=0}^{3} (n+K-1)(-2\Delta^2 + \Delta^4(-1 + 2K(K+1)))}, \\
c_{15} &= \frac{\Delta^4}{64\sqrt{2}} \sqrt{\prod_{n=0}^{7} (n+K-3)}, \\
c_{22} &= -\frac{\Delta^2}{8} K(K+1)(-4 + \Delta^2(-2 + 3K(K+1))), \\
c_{24} &= -\frac{\Delta^4}{16} \sqrt{K(K+1) \prod_{n=0}^{5} (n+K-2)}, \\
c_{33} &= \frac{3\Delta^4}{32} \prod_{n=0}^{3} (n+K-1).
\end{aligned}
\tag{A.54}
$$

The eigenvalue equation corresponding to $\hat{\varrho}'_{1,S\Delta}$ can be written as

$$\begin{pmatrix} b_{11} & 0 & b_{13} \\ 0 & b_{22} & 0 \\ b_{13} & 0 & 0 \end{pmatrix} \begin{pmatrix} x_1 \\ x_2 \\ x_3 \end{pmatrix} = E^{(1)} \begin{pmatrix} x_1 \\ x_2 \\ x_3 \end{pmatrix}, \tag{A.55}$$

where $E^{(1)}$ and $|e^{(1)}\rangle = x_1|v_1\rangle + x_2|v_2\rangle + x_3|v_3\rangle$ are the eignenvalues and eigenvectors (the basis vectors are given in Eqn. (A.52)) of $\hat{\varrho}'_{1,\mathrm{S}\Delta}$. The matrix equation gives 3 simultaneous equations of the form

$$\begin{aligned} b_{11}x_1 + b_{13}x_3 &= E^{(1)}x_1 \\ b_{22}x_2 &= E^{(1)}x_2 \\ b_{13}x_1 &= E^{(1)}x_3. \end{aligned} \tag{A.56}$$

The second equation in (A.56) gives the first eigenvalue and eigenvector of

$$E_1^{(1)} = b_{22} \tag{A.57}$$

and

$$|e_1^{(1)}\rangle = |v_2\rangle. \tag{A.58}$$

The remaining two equations form a 2×2 matrix with eigenvalue equation

$$\begin{pmatrix} b_{11} & b_{13} \\ b_{13} & 0 \end{pmatrix} \begin{pmatrix} x_1 \\ x_3 \end{pmatrix} = E^{(1)} \begin{pmatrix} x_1 \\ x_3 \end{pmatrix} \tag{A.59}$$

and characteristic polynomial of $(E^{(1)})^2 - b_{11}E^{(1)} - b_{13}^2$. The resulting eigenvalues and the corresponding eigenvectors are

$$
\begin{aligned}
E_2^{(1)} &= \frac{b_{11} - \sqrt{b_{11}^2 + 4b_{13}^2}}{2} \\
E_3^{(1)} &= \frac{b_{11} + \sqrt{b_{11}^2 + 4b_{13}^2}}{2}
\end{aligned}
\tag{A.60}
$$

and

$$
\begin{aligned}
|e_2^{(1)}\rangle &= \frac{E_2^{(1)}}{b_{13}}|v_1\rangle + |v_3\rangle \\
|e_3^{(1)}\rangle &= \frac{E_3^{(1)}}{b_{13}}|v_1\rangle + |v_3\rangle.
\end{aligned}
\tag{A.61}
$$

Eigenvectors $|e_2^{(1)}\rangle$ and $|e_3^{(1)}\rangle$ need to be normalised by dividing them by the magnitude of the vectors. $E_1^{(1)}$ and $|e_1^{(1)}\rangle$ contain terms of order up to Δ^2, however, $E_2^{(1)}$ and $|e_2^{(1)}\rangle$, and $E_3^{(1)}$ and $|e_3^{(1)}\rangle$ contain also terms of higher order. Additionally, eigenvalue $E_2^{(1)}$ appears to be negative, however, further Taylor expanding this eigenvalue reveals that it is in fact zero within the approximation. Taylor expansion of the eigenvalues and eigenvectors to the second order in Δ about $\Delta = 0$ results in the following eigenvalues and normalised eigenvectors,

$$
\begin{aligned}
E_1^{(1)} &= b_{22} \\
E_2^{(1)} &= 0 \\
E_3^{(1)} &= b_{11}
\end{aligned}
\tag{A.62}
$$

and

$$
\begin{aligned}
|e_1^{(1)}\rangle &= |v_2\rangle \\
|e_2^{(1)}\rangle &= -b_{13}|v_1\rangle + |v_3\rangle \\
|e_3^{(1)}\rangle &= -|v_1\rangle - b_{13}|v_3\rangle.
\end{aligned}
\tag{A.63}
$$

These eigenvectors and eigenvalues reconstruct the HB density matrix accurate to the second order in Δ. Therefore, Taylor expanding the evolved HB density matrix to the second order in Δ about $\Delta = 0$ in fact produces a rank 2 matrix within the approximation which can be used when calculating H_{11}. Note that neglecting the higher order terms fits within the original constraint of $\Delta^2 \ll 1/K^2$.

The same procedure is applied to $\hat{\varrho}'_{2,\mathrm{S}\Delta}$ which can be described by the following 5 simultaneous equations,

$$
\begin{aligned}
c_{11}y_1 + c_{13}y_3 + c_{15}y_5 &= E^{(2)}y_1 \\
c_{22}y_2 + c_{24}y_4 &= E^{(2)}y_2 \\
c_{13}y_1 + c_{33}y_3 &= E^{(2)}y_3 \\
c_{24}y_2 &= E^{(2)}y_4 \\
c_{15}y_1 &= E^{(2)}y_5,
\end{aligned}
\tag{A.64}
$$

where $E^{(2)}$ and $|e^{(2)}\rangle = y_1|v_1\rangle + y_2|v_2\rangle + y_3|v_3\rangle + y_4|v_4\rangle + y_5|v_5\rangle)$ are the eignenvalues and eigenvectors of $\hat{\varrho}'_{2,\mathrm{S}\Delta}$. Since y_2 and y_4 occur only in the second and fourth equation of (A.64) and y_1, y_3 and y_5 in the first, third and fifth equation of (A.64) then $\hat{\varrho}'_{2,\mathrm{S}\Delta}$ can be written as a direct sum of 2×2 and 3×3 matrices with the following eigenvalue equations,

$$\begin{pmatrix} c_{22} & c_{24} \\ c_{24} & 0 \end{pmatrix} \begin{pmatrix} y_2 \\ y_4 \end{pmatrix} = E^{(2)} \begin{pmatrix} y_2 \\ y_4 \end{pmatrix} \tag{A.65}$$

and

$$\begin{pmatrix} c_{11} & c_{13} & c_{15} \\ c_{13} & c_{33} & 0 \\ c_{15} & 0 & 0 \end{pmatrix} \begin{pmatrix} y_1 \\ y_3 \\ y_5 \end{pmatrix} = E^{(2)} \begin{pmatrix} y_1 \\ y_3 \\ y_5 \end{pmatrix}. \tag{A.66}$$

The 2×2 matrix gives eigenvalues

$$\begin{aligned} E_1^{(2)} &= \frac{c_{22} - \sqrt{c_{22}^2 + 4c_{24}^2}}{2} \\ E_2^{(2)} &= \frac{c_{22} + \sqrt{c_{22}^2 + 4c_{24}^2}}{2} \end{aligned} \tag{A.67}$$

with the corresponding eigenvectors

$$\begin{aligned} |e_1^{(2)}\rangle &= \frac{E_1^{(2)}}{c_{24}} |v_2\rangle + |v_4\rangle, \\ |e_2^{(2)}\rangle &= \frac{E_2^{(2)}}{c_{24}} |v_2\rangle + |v_4\rangle, \end{aligned} \tag{A.68}$$

where the eigenvectors need to be normalised by dividing them by the vector magnitude.

The 3×3 matrix has a characteristic polynomial α of the form of a cubic equation

$$\alpha = k(E^{(2)})^3 + l(E^{(2)})^2 + mE^{(2)} + n, \tag{A.69}$$

where $k = -1$, $l = (c_{33} + c_{11})$, $m = (-c_{11}c_{33} + c_{15}^2 + c_{13}^2)$ and $n = -c_{15}^2 c_{33}$. The resulting eigenvalue solutions and the corresponding eigenvectors are

$$E_i^{(2)} = -\frac{1}{3k}\left(l + u_i C + \frac{\zeta_0}{u_i C}\right) \tag{A.70}$$

and

$$|e_i^{(2)}\rangle = \frac{E_i^{(2)}}{c_{15}}|v_1\rangle + \frac{1}{c_{13}}\left(\frac{(E_i^{(2)})^2}{c_{15}} - c_{15} - \frac{c_{11}E_i^{(2)}}{c_{15}}\right)|v_3\rangle + |v_5\rangle, \tag{A.71}$$

where $i = \{3,4,5\}$, $u_1 = 1$, $u_2 = \left(-1+\mathrm{i}\sqrt{3}\right)/2$, $u_3 = \left(-1-\mathrm{i}\sqrt{3}\right)/2$, $C = \left(\left(\zeta_1 + \sqrt{-27k^2\zeta}\right)/2\right)^{1/3}$, $\zeta_0 = (l^2 - 3km)$, $\zeta_1 = (2l^3 - 9klm + 27k^2 n)$ and $\zeta = (18klmn - 4l^3 n + l^2 m^2 - 4km^3 - 27k^2 n^2)$. This time, eigenvalues $E_1^{(2)}$ and $E_4^{(2)}$ appear to be negative, however, Taylor expanding the eigenvalues to the fourth order in Δ about $\Delta = 0$, we get

$$\begin{aligned}
E_1^{(2)} &= 0\\
E_2^{(2)} &= c_{22}\\
E_3^{(2)} &= c_{11} + \frac{K(1+K)(-2+K(1+K))\Delta^4}{32}\\
E_4^{(2)} &= 0\\
E_5^{(2)} &= \frac{2}{3}c_{33}.
\end{aligned} \tag{A.72}$$

The corresponding normalised eigenvectors expanded to the fourth order in Δ are not shown since they are complicated functions of K and Δ. The zero eigenvalues and the corresponding eigenvectors do not contribute when reconstructing the density matrix accurate to the fourth order in Δ. The remaining non-zero eigenvalues ($E_2^{(2)}$, $E_3^{(2)}$ and $E_5^{(2)}$) and the corresponding

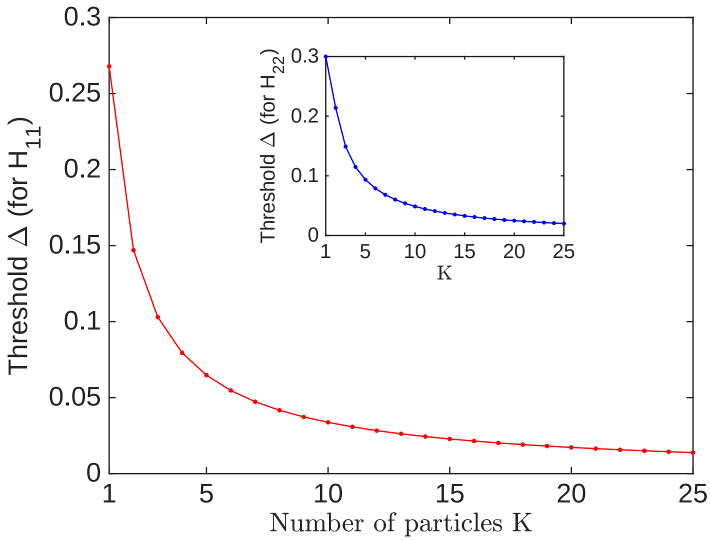

Figure A.4: Phase diffusion validity plot for the small phase diffusion approximation for HB states. The figure shows the threshold values of Δ as a function of particle number (K) when the highest allowed relative error on the QFI ($\delta H_{ii}/H_{ii}$) is 0.05.

eigenvectors reconstruct the density matrix accurate to the fourth order in Δ when using their full forms given in Eqn. (A.67), Eqn. (A.68), Eqn. (A.70) and Eqn. (A.71). The reason to use the full forms is that the eigenvectors (corresponding to $E_2^{(2)}$, $E_3^{(2)}$ and $E_5^{(2)}$) contain Δ^{-4} terms and therefore higher order terms in the expansion are required to ensure that we do not lose the fourth order terms in Δ due to cancellations.

These eigenvalues and eigenvectors can then be used to calculate the diagonal elements of the QFI matrix by using Eqn. (7.15). These elements are given in Eqn. (10.17) and Eqn. (10.18) of the main text.

Fig. (A.4) represents the phase diffusion validity plot for the small Δ approximation. It shows the maximum allowed phase diffusion values as a function of K when the highest allowed relative error on the QFI ($\delta H_{ii}/H_{ii}$) is 0.05.

A.12 Joint estimation trade-off for HB states as $\Delta \to 0$

Similarly to the approach taken when calculating the trade-off in the large phase diffusion approximation (shown in Appendix (A.8)), we use the HB density matrix expanded to the second order in Δ about $\Delta = 0$ (Eqn. (10.9)) and a complete POVM set $\{\pi_y\}$ composed of projectors $|v_y\rangle = \sum_{n=0}^{K} r_{y,n} \mathrm{e}^{\mathrm{i}X_{y,n}} |2n, 2K-2n\rangle$ to calculate the probability associated with the y^{th} outcome. The probability and its corresponding derivatives with respect to ϕ and Δ are,

$$p_y = \langle v_y | \hat{\varrho}_{1,\mathrm{S}\Delta} | v_y \rangle = \sum_{n,n'=0}^{K} R_{y,n,n'} (1 - 2\Delta^2 (n-n')^2) \cos(\Theta_{y,n,n'}), \tag{A.73}$$

$$\partial_\phi p_y = -2 \sum_{n,n'=0}^{K} R_{y,n,n'} (1 - 2\Delta^2 (n-n')^2)(n-n') \sin\left(\Theta_{y,n,n'}\right) \tag{A.74}$$

and

$$\partial_\Delta p_y = -4\Delta \sum_{n,n'=0}^{K} R_{y,n,n'} (n-n')^2 \cos\left(\Theta_{y,n,n'}\right), \tag{A.75}$$

where $\Theta_{y,n,n'} = \left(X_{y,n'} - X_{y,n} + 2\phi(n-n')\right)$ and $R_{y,n,n'} = r_{y,n} r_{y,n'} b_n b_{n'}$. The associated diagonal elements of the Fisher information matrix, F_{11} and F_{22}, corresponding to the individual estimation of ϕ and Δ respectively are,

$$\begin{aligned} F_{11} &= \sum_{y=0}^{K} \left(\frac{4\left(\sum_{n,n'=0}^{K} R_{y,n,n'} \sin\left(\Theta_{y,n,n'}\right)\left(n-n'\right)\left(1-2\Delta^2\left(n-n'\right)^2\right)\right)^2}{\sum_{n,n'=0}^{K} R_{y,n,n'} \cos\left(\Theta_{y,n,n'}\right)\left(1-2\Delta^2\left(n-n'\right)^2\right)} \right) \\ &\approx \sum_{y=0}^{K} \left(\frac{4\left(\sum_{n,n'=0}^{K} R_{y,n,n'} \sin\left(\Theta_{y,n,n'}\right)\left(n-n'\right)\right)^2}{\sum_{n,n'=0}^{K} R_{y,n,n'} \cos\left(\Theta_{y,n,n'}\right)} \right) \end{aligned} \tag{A.76}$$

and

$$\begin{aligned} F_{22} &= \sum_{y=0}^{K} \left(\frac{16\Delta^2 \left(\sum_{n,n'=0}^{K} R_{y,n,n'} \cos\left(\Theta_{y,n,n'}\right) \left(n-n'\right)^2 \right)^2}{\sum_{n,n'=0}^{K} R_{y,n,n'} \cos\left(\Theta_{y,n,n'}\right) \left(1 - 2\Delta^2 (n-n')^2\right)} \right) \\ &\approx \sum_{y=0}^{K} \left(\frac{16\Delta^2 \left(\sum_{n,n'=0}^{K} R_{y,n,n'} \cos\left(\Theta_{y,n,n'}\right) \left(n-n'\right)^2 \right)^2}{\sum_{n,n'=0}^{K} R_{y,n,n'} \cos\left(\Theta_{y,n,n'}\right)} \right), \end{aligned} \tag{A.77}$$

where the approximations are made assuming that $\Delta \to 0$ so that terms containing $2\Delta^2 \left(n-n'\right)^2$ are negligible compared to 1. Using the QFI expressions found in Eqn. (10.17) and Eqn. (10.18) and assuming $\Delta \to 0$ so that terms containing $2K(K+1)\Delta^2$ are negligible compared to 1, we can compute $\mathrm{Tr}\left[\mathbf{FH}^{-1}\right]$

$$\begin{aligned} &\mathrm{Tr}\left[\mathbf{FH}^{-1}\right] = \\ &= \frac{2}{K(K+1)} \sum_{y=0}^{K} \frac{\left(\sum_{n,n'=0}^{K} R_{y,n,n'} \sin\left(\Theta_{y,n,n'}\right) \left(n-n'\right) \right)^2 + 4\Delta^2 \left(\sum_{n,n'=0}^{K} R_{y,n,n'} \cos\left(\Theta_{y,n,n'}\right) \left(n-n'\right)^2 \right)^2}{\sum_{n,n'=0}^{K} R_{y,n,n'} \cos\left(\Theta_{y,n,n'}\right)}. \end{aligned} \tag{A.78}$$

The Δ term appearing in the trade-off in Eqn. (A.78) cannot be simply neglected (by invoking $\Delta \to 0$) because we require to compare terms of the form: $\sin\left(\Theta_{y,n,n'}\right) \sin\left(\Theta_{y,m,m'}\right)$ and $4\Delta^2 \cos\left(\Theta_{y,n,n'}\right) \cos\left(\Theta_{y,m,m'}\right) \left(n-n'\right) \left(m-m'\right)$. If the phase of the POVM has some Δ dependence then it is not straightforward which term dominates. In fact, to obtain significant Fisher information for the diffusion parameter for decreasing values of Δ, we would expect some Δ dependence in the POVM to reduce the effect of the Δ^2 factor. Without knowing further structure of the optimal POVM, standard optimisation is a difficult task to perform. However, the numerical results based on the simulated annealing algorithm suggest that as $\Delta \to 0$ the trade-off approaches 1 (see Fig. (10.6) of the main text).

Bibliography

[1] S. Gupta, *Units of Measurement – Past, Present and Future. International System of Units*Springer Series in Materials Science (Springer Science and Business Media, 2009).

[2] T. Quinn and J. Kovalevsky, *The development of modern metrology and its role today*, Phil. Trans. R. Soc. A **363**, 2307 (2005).

[3] G. Enzian, M. Szczykulska, J. Silver, L. D. Bino, S. Zhang, I. A. Walmsley, P. Del'Haye, and M. R. Vanner, *Observation of Brillouin optomechanical strong coupling with an 11 GHz mechanical mode*, Optica **6**, 7 (2019).

[4] M. Szczykulska, T. Baumgratz, and T. Datta, *Multi-parameter quantum metrology*, Advances in Physics: X **1**, 621 (2016).

[5] M. Szczykulska, T. Baumgratz, and A. Datta, *Reaching for the quantum limits in the simultaneous estimation of phase and phase diffusion*, Quantum Science and Technology **2**, 044004 (2017).

[6] K. Jacobs and D. A. Steck, *A straightforward introduction to continuous quantum measurement*, Contemporary Physics **47**, 279 (2006).

[7] H. M. Wiseman and G. J. Milburn, *Quantum Measurement and Control* (Cambridge University Press, 2009).

[8] M. A. Nielsen and I. L. Chuang, *Quantum Computation and Quantum Information: 10th Anniversary Edition*, 10th edition (Cambridge University Press, New York, NY, USA, 2011).

[9] M. J. Holland and K. Burnett, *Interferometric detection of optical phase shifts at the Heisenberg limit*, Phys. Rev. Lett. **71**, 1355 (1993).

[10] R. Demkowicz-Dobrzański, M. Jarzyna, and J. Kołodyński, *Quantum Limits in Optical Interferometry*, **60**, 345 (2015).

[11] P. C. Humphreys, M. Barbieri, A. Datta, and I. A. Walmsley, *Quantum Enhanced Multiple Phase Estimation*, Phys. Rev. Lett. **111**, 070403 (2013).

[12] I. Bialynicki-Birula, *The Wigner functional of the electromagnetic field*, Optics Communications **179**, 237 (2000).

[13] G. Adesso, S. Ragy, and A. R. Lee, *Continuous Variable Quantum Information: Gaussian States and Beyond*, Open Systems & Information Dynamics **21**, 1440001 (2014).

[14] C. M. Caves, *Quantum-mechanical noise in an interferometer*, Phys. Rev. D **23**, 1693 (1981).

[15] C. M. Caves, K. S. Thorne, R. W. P. Drever, V. D. Sandberg, and M. Zimmermann, *On the measurement of a weak classical force coupled to a quantum-mechanical oscillator. I. Issues of principle*, Rev. Mod. Phys. **52**, 341 (1980).

[16] L. Blair, D.and Ju, C. Zhao, L. Wen, and et. al, *Gravitational wave astronomy: the current status*, Sci. China-Phys. Mech. Astron. **58**, 120402 (2015).

[17] M. A. Taylor and W. P. Bowen, *Quantum metrology and its application in biology*, Physics Reports **615**, 1 (2016).

[18] S. Pang and T. A. Brun, *Quantum metrology for a general Hamiltonian parameter*, Phys. Rev. A **90**, 022117 (2014).

[19] H. M. Wiseman and R. B. Killip, *Adaptive single-shot phase measurements: The full quantum theory*, Phys. Rev. A **57**, 2169 (1998).

[20] J.-P. Pellonpää and J. Schultz, *Measuring the canonical phase with phase-space measurements*, Phys. Rev. A **88**, 012121 (2013).

[21] V. B. Braginskiĭ and A. B. Manukin, *Ponderomotive Effects of Electromagnetic Radiation*, Sov. Phys. JETP **25**, 653 (1967).

[22] V. B. Braginskiĭ, A. B. Manukin, and M. Y. Tikhonov, *Investigation of Dissipative Ponderomotive Effects of Electromagnetic Radiation*, Sov. Phys. JETP **31**, 829 (1970).

[23] K. Tsubono, S. Hiramatsu, and H. Hirakawa, *Cavity Transducer for Subatomic Mechanical Vibration*, Jpn. J. Appl. Phys. **16**, 1641 (1977).

[24] K. Tsubono, M. Ohashi, and H. Hirakawa, *Parametric Transducer for Gravitational Radiation Detector*, Jpn. J. Appl. Phys. **25**, 622 (1986).

[25] V. B. Braginskiĭ, *Classical and Quantum Restrictions on the Detection of Weak Disturbances of a Macroscopic Oscillator*, Sov. Phys. JETP **26**, 831 (1968).

[26] M. Aspelmeyer, T. J. Kippenberg, and F. Marquardt, *Cavity optomechanics*, Rev. Mod. Phys. **86**, 1391 (2014).

[27] M. Metcalfe, *Applications of cavity optomechanics*, Appl. Phys. Rev. **1**, 031105 (2014).

[28] R. Manenti, A. F. Kockum, A. Patterson, T. Behrle, J. Rahamim, G. Tancredi, F. Nori, and P. J. Leek, *Circuit quantum acoustodynamics with surface acoustic waves*, Nat. Commun. **8**, 2041 (2017).

[29] A. Pontin, J. E. Lang, A. Chowdhury, P. Vezio, F. Marino, B. Morana, E. Serra, F. Marin, and T. S. Monteiro, *Imaging Correlations in Heterodyne Spectra for Quantum Displacement Sensing,* Phys. Rev. Lett. **120**, 020503 (2018).

[30] W. Zhang, Y. Han, B. Xiong, and L. Zhou, *Optomechanical force sensor in a non-Markovian regime,* New Journal of Physics **19**, 083022 (2017).

[31] D. Hempston, J. Vovrosh, M. ToroÅ¡, G. Winstone, M. Rashid, and H. Ulbricht, *Force sensing with an optically levitated charged nanoparticle,* Applied Physics Letters **111**, 133111 (2017).

[32] V. B. Braginskiĭ and S. P. Vyatchanin, *Low quantum noise tranquilizer for Fabry–Perot interferometer,* Phys. Lett. A **293**, 228 (2002).

[33] C. H. Metzger and K. Karrai, *Cavity cooling of a microlever,* Nature **432**, 1002 (2004).

[34] O. Arcizet, P.-F. Cohadon, T. Briant, M. Pinard, and A. Heidmann, *Radiation-pressure cooling and optomechanical instability of a micromirror,* Nature **444**, 71 (2006).

[35] S. Gigan, H. R. Böhm, M. Paternostro, F. Blaser, G. Langer, J. B. Hertzberg, K. C. Schwab, D. Bäuerle, M. Aspelmeyer, and A. Zeilinger, *Self-cooling of a micromirror by radiation pressure,* Nature **444**, 67 (2006).

[36] F. Marquardt, J. P. Chen, A. A. Clerk, and S. M. Girvin, *Quantum Theory of Cavity-Assisted Sideband Cooling of Mechanical Motion,* Phys. Rev. Lett. **99**, 093902 (2007).

[37] J. D. Teufel, T. Donner, D. Li, J. W. Harlow, M. S. Allman, K. Cicak, A. J. Sirois, J. D. Whittaker, K. W. Lehnert, and R. W. Simmonds, *Sideband cooling of micromechanical motion to the quantum ground state,* Nature **475**, 359 (2011).

[38] J. Chan, T. P. M. Alegre, A. H. Safavi-Naeini, J. T. Hill, A. Krause, S. Gröblacher, M. Aspelmeyer, and O. Painter, *Laser cooling of a nanomechanical oscillator into its quantum ground state,* Nature **478**, 89 (2011).

[39] G. Bahl, M. Tomes, F. Marquardt, and Carmon, *Observation of spontaneous Brillouin cooling,* Nat. Phys. **8**, 203 (2012).

[40] R. W. Peterson, T. P. Purdy, N. S. Kampel, R. W. Andrews, P.-L. Yu, K. W. Lehnert, and C. A. Regal, *Laser Cooling of a Micromechanical Membrane to the Quantum Backaction Limit,* Phys. Rev. Lett. **116**, 063601 (2016).

[41] W. Wieczorek, S. G. Hofer, J. Hoelscher-Obermaier, R. Riedinger, K. Hammerer, and M. Aspelmeyer, *Optimal State Estimation for Cavity Optomechanical Systems,* Phys. Rev. Lett. **114**, 223601 (2015).

[42] S. Mancini, D. Vitali, and P. Tombesi, *Optomechanical Cooling of a Macroscopic Oscillator by Homodyne Feedback,* Phys. Rev. Lett. **80**, 688 (1998).

[43] D. Kleckner and D. Bouwmeester, *Sub-kelvin optical cooling of a micromechanical resonator,* Nature **444**, 75 (2006).

[44] M. R. Vanner, J. Hofer, G. D. Cole, and M. Aspelmeyer, *Cooling-by-measurement and mechanical state tomography via pulsed optomechanics,* Nat. Commun. **4**, 1 (2013).

[45] M. Rossi, N. Kralj, S. Zippilli, R. Natali, A. Borrielli, G. Pandraud, E. Serra, G. Di Giuseppe, and D. Vitali, *Enhancing Sideband Cooling by Feedback-Controlled Light,* Phys. Rev. Lett. **119**, 123603 (2017).

[46] M. Rossi, D. Mason, J. Chen, Y. Tsaturyan, and A. Schliesser, *Measurement-based quantum control of mechanical motion,* arXiv:1805.05087 (2018).

[47] A. Dorsel, J. D. McCullen, P. Meystre, E. Vignes, and H. Walther, *Optical Bistability and Mirror Confinement Induced by Radiation Pressure,* Phys. Rev. Lett. **51**, 1550 (1983).

[48] M. Tomes, F. Marquardt, G. Bahl, and T. Carmon, *Quantum-mechanical theory of optomechanical Brillouin cooling,* Phys. Rev. A **84**, 063806 (2011).

[49] K. J. Vahala, *Optical microcavities,* Nature **424**, 839 (2003).

[50] P. Del'Haye, S. A. Diddams, and S. B. Papp, *Laser-machined ultra-high-Q microrod resonators for nonlinear optics,* Appl. Phys. Lett. **102**, 221119 (2013).

[51] T. J. Kippenberg and K. J. Vahala, *Cavity Optomechanics: Back-Action at the Mesoscale,* Science **321**, 1172 (2008).

[52] A. A. Clerk, M. H. Devoret, S. M. Girvin, F. Marquardt, and R. J. Schoelkopf, *Introduction to quantum noise, measurement, and amplification,* Rev. Mod. Phys. **82**, 1155 (2010).

[53] L. Brillouin, *Diffusion de la lumière et des rayons X par un corps transparent homogène,* Ann. Phys. (Paris) **17**, 88 (1922).

[54] R. W. Boyd, *Nonlinear Optics,* 3rd edition (Academic Press, Inc., 2008).

[55] M. Ringbauer, T. J. Weinhold, L. A. Howard, A. G. White, and M. R. Vanner, *Generation of mechanical interference fringes by multi-photon counting,* New J. Phys. **20**, 053042 (2018).

[56] Z. Zhu, D. J. Gauthier, and R. W. Boyd, *Stored Light in an Optical Fiber via Stimulated Brillouin Scattering,* Science **318**, 1748 (2007).

[57] V. Fiore, Y. Yang, M. C. Kuzyk, R. l. Barbour, L. Tian, and H. Wang, *Storing Optical Information as a Mechanical Excitation in a Silica Optomechanical Resonator,* Phys. Rev. Lett. **107**, 133601 (2011).

[58] G. S. Wiederhecker, S. Manipatruni, S. Lee, and M. Lipson, *Broadband tuning of optomechanical cavities,* Opt. Express **19**, 2782 (2011).

[59] C. G. Baker, C. Bekker, D. L. McAuslan, E. Sheridan, and W. P. Bowen, *High bandwidth on-chip capacitive tuning of microtoroid resonators,* Opt. Express **24**, 20400 (2016).

[60] T. P. Purdy, R. W. Peterson, and C. A. Regal, *Observation of Radiation Pressure Shot Noise on a Macroscopic Object,* Science **339**, 801 (2013).

[61] S. Forstner, E. Sheridan, J. Knittel, C. L. Humphreys, G. A. Brawley, H. Rubinsztein-Dunlop, and W. P. Bowen, *Ultrasensitive Optomechanical Magnetometry,* Adv. Mater. **26**, 6348 (2014).

[62] Y. Liu, H. Miao, V. Aksyuk, and K. Srinivasan, *Wide cantilever stiffness range cavity optomechanical sensors for atomic force microscopy,* Opt. Express **20**, 18268 (2012).

[63] T. L. S. Collaboration, *A gravitational wave observatory operating beyond the quantum shot-noise limit,* Nat. Phys. **7**, 962 (2011).

[64] J. W. S. B. Rayleigh, *The Theory of Sound*, 2nd edition (Macmillan, 1894).

[65] S. Le Floch and P. Cambon, *Study of Brillouin gain spectrum in standard single-mode optical fiber at low temperatures (1.4–370 K) and high hydrostatic pressures (1–250 bars),* Opt. Commun. **219**, 395 (2003).

[66] T. Carmon, L. Yang, and K. J. Vahala, *Dynamical thermal behavior and thermal self-stability of microcavities,* Opt. Express **12**, 4742 (2004).

[67] A. Barchielli and B. Vacchini, *Quantum Langevin equations for optomechanical systems,* New J. Phys. **17**, 083004 (2015).

[68] A. H. Safavi-Naeini, J. Chan, J. T. Hill, S. Gröblacher, H. Miao, Y. Chen, M. Aspelmeyer, and O. Painter, *Laser noise in cavity-optomechanical cooling and thermometry,* New J. Phys. **15**, 035007 (2013).

[69] V. B. Braginskiǐ and Y. I. Vorontsov, *Quantum-mechanical limitations in macroscopic experiments and modern experimental technique,* Soviet Physics Uspekhi **17**, 644 (1975).

[70] V. B. Braginskiǐ, Y. I. Vorontsov, and K. S. Thorne, *Quantum Nondemolition Measurements,* Science **209**, 547 (1980).

[71] W. Bowen and G. Milburn, *Quantum Optomechanics* (Taylor & Francis, 2016).

[72] P. F. Cohadon, A. Heidmann, and M. Pinard, *Cooling of a Mirror by Radiation Pressure,* Phys. Rev. Lett. **83**, 3174 (1999).

[73] M. Poggio, C. L. Degen, H. J. Mamin, and D. Rugar, *Feedback Cooling of a Cantilever's Fundamental Mode below 5 mK,* Phys. Rev. Lett. **99**, 017201 (2007).

[74] T. Li, S. Kheifets, and M. G. Raizen, *Millikelvin cooling of an optically trapped microsphere in vacuum,* Nature Physics **7**, 527 (2011).

[75] M. Hosseini, G. Guccione, H. J. Slatyer, B. C. Buchler, and P. K. Lam, *Multimode laser cooling and ultra-high sensitivity force sensing with nanowires,* Nature Communications **5** (2014).

[76] G. I. Harris, U. L. Andersen, J. Knittel, and W. P. Bowen, *Feedback-enhanced sensitivity in optomechanics: Surpassing the parametric instability barrier,* Phys. Rev. A **85**, 061802 (2012).

[77] M. Rossi, N. Kralj, S. Zippilli, R. Natali, A. Borrielli, G. Pandraud, E. Serra, G. Di Giuseppe, and D. Vitali, *Normal-Mode Splitting in a Weakly Coupled Optomechanical System,* Phys. Rev. Lett. **120**, 073601 (2018).

[78] M. R. Vanner, I. Pikovski, G. D. Cole, M. S. Kim, Č. Brukner, K. Hammerer, G. J. Milburn, and M. Aspelmeyer, *Pulsed quantum optomechanics,* Proceedings of the National Academy of Sciences **108**, 16182 (2011).

[79] J. Zhang and K. Mølmer, *Prediction and retrodiction with continuously monitored Gaussian states,* Phys. Rev. A **96**, 062131 (2017).

[80] A. Serafini, *Quantum Continuous Variables: A Primer of Theoretical Methods* (Taylor & Francis Group, 2017).

[81] S. L. Braunstein, *Quantum limits on precision measurements of phase,* Phys. Rev. Lett. **69**, 3598 (1992).

[82] S. L. Braunstein and C. M. Caves, *Statistical distance and the geometry of quantum states,* Phys. Rev. Lett. **72**, 3439 (1994).

[83] I. Chuang, *Quantum algorithm for distributed clock synchronization,* Physical review letters **85**, 2006 (2000).

[84] V. Giovannetti, S. Lloyd, and L. Maccone, *Quantum-Enhanced Measurements: Beating the Standard Quantum Limit,* Science **306**, 1330 (2004).

[85] R. X. Adhikari, *Gravitational radiation detection with laser interferometry,* Rev. Mod. Phys. **86**, 121 (2014).

[86] LIGO Scientific Collaboration and Virgo Collaboration, B. P. Abbott and et. al, *Observation of Gravitational Waves from a Binary Black Hole Merger,* Phys. Rev. Lett. **116**, 061102 (2016).

[87] J. Ziv and M. Zakai, *Some lower bounds on signal parameter estimation,* IEEE Transactions on Information Theory **15**, 386 (1969).

[88] E. Weinstein and A. J. Weiss, *A general class of lower bounds in parameter estimation,* IEEE Transactions on Information Theory **34**, 338 (1988).

[89] E. W. Barankin, *Locally Best Unbiased Estimates,* The Annals of Mathematical Statistics **20**, 477 (1949).

[90] A. Holevo, *Probabilistic and Statistical Aspects of Quantum Mechanics* (North-Holland, Amsterdam, 1982).

[91] S. Amari and H. Nagaoka, *Methods of Information Geometry,* Translations of Mathematical monographs Vol. 191 (American Mathematical Society, 2000).

[92] T. M. Cover and J. A. Thomas, *Elements of Information Theory (Wiley Series in Telecommunications and Signal Processing)* (Wiley-Interscience, 2006).

[93] C. Helstrom, *Quantum Detection and Estimation Theory* (Academic Press, 1976).

[94] T. Baumgratz and A. Datta, *Quantum Enhanced Estimation of a Multidimensional Field*, Physical Review Letters **116**, 030801 (2016).

[95] N. Spagnolo, L. Aparo, C. Vitelli, A. Crespi, R. Ramponi, R. Osellame, P. Mataloni, and F. Sciarrino, *Quantum interferometry with three-dimensional geometry*, Sci. Rep. **2**, 862 (2012).

[96] J.-D. Yue, Y.-R. Zhang, and H. Fan, *Quantum-enhanced metrology for multiple phase estimation with noise*, Sci. Rep. **4**, 5933 (2014).

[97] Y.-R. Zhang and H. Fan, *Quantum metrological bounds for vector parameters*, Phys. Rev. A **90**, 043818 (2014).

[98] Y. Gao and H. Lee, *Bounds on quantum multiple-parameter estimation with Gaussian state*, The Euro. Phys. Jour. D **68**, 1 (2014).

[99] D. W. Berry, M. Tsang, M. J. W. Hall, and H. M. Wiseman, *Quantum Bell-Ziv-Zakai Bounds and Heisenberg Limits for Waveform Estimation*, Phys. Rev. X **5**, 031018 (2015).

[100] Y.-L. Zhang, H. Wang, L. Jing, L.-Z. Mu, and H. Fan, *Fitting magnetic field gradient with Heisenberg-scaling accuracy*, Sci. Rep. **4**, 7390 (2014).

[101] M. Zuppardo, J. P. Santos, G. De Chiara, M. Paternostro, F. L. Semião, and G. M. Palma, *Cavity-aided quantum parameter estimation in a bosonic double-well Josephson junction*, Phys. Rev. A **91**, 033631 (2015).

[102] D. Petz and C. Sudár, *Geometries of quantum states*, J. Math. Phys. **37**, 2662 (1996).

[103] E. Ercolessi and M. Schiavina, *Geometry of mixed states for a q-bit and the quantum Fisher information tensor*, Journal of Physics A: Mathematical and Theoretical **45**, 365303 (2012).

[104] E. Ercolessi and M. Schiavina, *Symmetric logarithmic derivative for general n-level systems and the quantum Fisher information tensor for three-level systems*, Physics Letters A **377**, 1996 (2013).

[105] I. Contreras, E. Ercolessi, and M. Schiavina, *On the geometry of mixed states and the Fisher information tensor*, Journal of Mathematical Physics **57** (2016).

[106] S. Z. Ang, R. Nair, and M. Tsang, *Quantum limit for two-dimensional resolution of two incoherent optical point sources*, Phys. Rev. A **95**, 063847 (2017).

[107] J. M. Martinis, *Qubit metrology for building a fault-tolerant quantum computer*, Npj Quantum Information , 15005 (2015).

[108] A. M. Childs, J. Preskill, and J. Renes, *Quantum information and precision measurement*, J. Mod. Opt. **47**, 155 (2000).

[109] B. M. Escher, R. L. de Matos Filho, and L. Davidovich, *General framework for estimating the ultimate precision limit in noisy quantum-enhanced metrology,* Nat. Phys. **7**, 406 (2011).

[110] R. Demkowicz-Dobrzański, J. Kołodyński, and M. Guţă, *The elusive Heisenberg limit in quantum-enhanced metrology,* Nat. Commun. **3**, 1063 (2012).

[111] R. Demkowicz-Dobrzański, U. Dorner, B. J. Smith, J. S. Lundeen, W. Wasilewski, K. Banaszek, and I. A. Walmsley, *Quantum phase estimation with lossy interferometers,* Phys. Rev. A **80**, 013825 (2009).

[112] U. Dorner, R. Demkowicz-Dobrzański, B. J. Smith, J. S. Lundeen, W. Wasilewski, K. Banaszek, and I. A. Walmsley, *Optimal Quantum Phase Estimation,* Phys. Rev. Lett. **102**, 040403 (2009).

[113] M. Kacprowicz, R. Demkowicz-Dobrzański, W. Wasilewski, K. Banaszek, and I. A. Walmsley, *Experimental quantum-enhanced estimation of a lossy phase shift,* Nat. Photon. **4**, 357 (2009).

[114] A. Datta, L. Zhang, N. Thomas-Peter, U. Dorner, B. J. Smith, and I. A. Walmsley, *Quantum metrology with imperfect states and detectors,* Phys. Rev. A - Atomic, Molecular, and Optical Physics **83**, 1 (2011).

[115] D. Brivio, S. Cialdi, S. Vezzoli, B. T. Gebrehiwot, M. G. Genoni, S. Olivares, and M. G. A. Paris, *Experimental estimation of one-parameter qubit gates in the presence of phase diffusion,* Phys. Rev. A **81**, 012305 (2010).

[116] M. G. Genoni, S. Olivares, and M. G. A. Paris, *Optical Phase Estimation in the Presence of Phase Diffusion,* Phys. Rev. Lett. **106**, 153603 (2011).

[117] M. G. Genoni, S. Olivares, D. Brivio, S. Cialdi, D. Cipriani, A. Santamato, S. Vezzoli, and M. G. A. Paris, *Optical interferometry in the presence of large phase diffusion,* Phys. Rev. A **85**, 043817 (2012).

[118] C. L. Degen, F. Reinhard, and P. Cappellaro, *Quantum sensing,* Rev. Mod. Phys. **89**, 035002 (2017).

[119] B. M. Escher, L. Davidovich, N. Zagury, and R. L. de Matos Filho, *Quantum Metrological Limits via a Variational Approach,* Phys. Rev. Lett. **109**, 190404 (2012).

[120] J. H. Cole and L. C. L. Hollenberg, *Scanning quantum decoherence microscopy,* Nanotechnology **20**, 495401 (2009).

[121] R. Schirhagl, K. Chang, M. Loretz, and C. L. Degen, *Nitrogen-vacancy centers in diamond: nanoscale sensors for physics and biology,* Annu. Rev. Phys. Chem. **65**, 83 (2014).

[122] T. M. Stace, *Quantum limits of thermometry,* Phys. Rev. A **82**, 011611 (2010).

[123] G. Kucsko, P. Maurer, N. Y. Yao, M. Kubo, H. Noh, P. Lo, H. Park, and M. D. Lukin, *Nanometre-scale thermometry in a living cell,* Nature **500**, 54 (2013).

[124] D. M. Toyli, C. F. de las Casas, D. J. Christle, V. V. Dobrovitski, and D. D. Awschalom, *Fluorescence thermometry enhanced by the quantum coherence of single spins in diamond*, PNAS **110**, 8417 (2013).

[125] D. Xie, C. Xu, and A. M. Wang, *Optimal quantum thermometry by dephasing,* Quantum Information Processing **16**, 155 (2017).

[126] G. A. Brawley, M. R. Vanner, P. E. Larsen, S. Schmid, A. Boisen, and W. P. Bowen, *Nonlinear optomechanical measurement of mechanical motion,* Nat. Commun. **7**, 10988 (2016).

[127] A. D. Cronin, J. Schmiedmayer, and D. E. Pritchard, *Optics and interferometry with atoms and molecules,* Rev. Mod. Phys. **81**, 1051 (2009).

[128] T. Musha, J. ichi Kamimura, and M. Nakazawa, *Optical phase fluctuations thermally induced in a single-mode optical fiber,* Appl. Opt. **21**, 694 (1982).

[129] J. Du and Z. He, *Sensitivity enhanced strain and temperature measurements based on FBG and frequency chirp magnification,* Opt. Express **21**, 27111 (2013).

[130] T. Berrada, S. van Frank, T. Schumm, J.-F. Schaff, and J. Schmiedmayer, *Integrated Mach-Zehnder interferometer for Bose-Einstein condensates,* Nat. Commun. **4**, 2077 (2013).

[131] J. C. Fang and J. Qin, *Advances in Atomic Gyroscopes: A View from Inertial Navigation Applications,* Sensors **12**, 6331 (2012).

[132] G. Rosi, F. Sorrentino, L. Cacciapuoti, M. Prevedelli, and G. M. Tino, *Precision measurement of the Newtonian gravitational constant using cold atoms,* Nature **510**, 518 (2014).

[133] I. Pikovski, M. Zych, and F. Costa, *Universal decoherence due to gravitational time dilation,* Nature Phys. **11**, 668 (2015).

[134] T. Oniga and C. H.-T. Wang, *Quantum gravitational decoherence of light and matter*, Phys. Rev. D **93**, 044027 (2016).

[135] M. G. Genoni, O. S. Duarte, and A. Serafini, *Unravelling the noise: the discrimination of wave function collapse models under time-continuous measurements,* New J. Phys. **18**, 103040 (2016).

[136] C. J. Riedel, *Direct detection of classically undetectable dark matter through quantum decoherence,* Phys. Rev. D **88**, 116005 (2013).

[137] S. I. Knysh and G. A. Durkin, *Estimation of Phase and Diffusion: Combining Quantum Statistics and Classical Noise,* arXiv:1307.0470 (2013).

[138] M. D. Vidrighin, G. Donati, M. G. Genoni, X.-M. Jin, W. S. Kolthammer, M. S. Kim, A. Datta, M. Barbieri, and I. A. Walmsley, *Joint estimation of phase and phase diffusion for quantum metrology,* Nat. Commun. **5**, 3532 (2014).

[139] M. Altorio, M. G. Genoni, M. D. Vidrighin, F. Somma, and M. Barbieri, *Weak measurements and the joint estimation of phase and phase diffusion*, Phys. Rev. A **92**, 032114 (2015).

[140] S. Ragy, M. Jarzyna, and R. Demkowicz-Dobrzański, *Compatibility in multiparameter quantum metrology*, Phys. Rev. A **94**, 052108 (2016).

[141] R. D. Gill and S. Massar, *State estimation for large ensembles*, Phys. Rev. A **61**, 042312 (2000).

[142] N. Li, C. Ferrie, J. A. Gross, A. Kalev, and C. M. Caves, *Fisher-Symmetric Informationally Complete Measurements for Pure States*, Phys. Rev. Lett. **116**, 180402 (2016).

[143] M. Jarzyna and R. Demkowicz-Dobrzański, *True precision limits in quantum metrology*, New Journal of Physics **17**, 013010 (2015).

[144] M. G. A. Paris, *Quantum estimation for quantum technology*, Int. J. Quantum Inf. **07**, 125 (2009).

[145] E. Roccia, I. Gianani, L. Mancino, M. Sbroscia, F. Somma, M. G. Genoni, and M. Barbieri, *Entangling measurements for multiparameter estimation with two qubits*, Quantum Science and Technology **3**, 01LT01 (2018).

[146] A. P. Dempster, N. M. Laird, and D. B. Rubin, *Maximum Likelihood from Incomplete Data via the EM Algorithm*, J. Roy. Statist. Soc. (B) **39**, 1 (1977).

[147] P. J. D. Crowley, A. Datta, M. Barbieri, and I. A. Walmsley, *Tradeoff in simultaneous quantum-limited phase and loss estimation in interferometry*, Physical Review A - Atomic, Molecular, and Optical Physics **89**, 1 (2014).

[148] M. A. Ballester, *Estimation of unitary quantum operations*, Phys. Rev. A **69**, 022303 (2004).

[149] C. Gagatsos, D. Branford, and A. Datta, *Gaussian systems for quantum enhanced multiple phase estimation*, Phys. Rev. A **94**, 042342 (2016).